이학박사 학위논문

형태가 제어된 반도체 나노구조의 합성, 분석 및 응용에 대한 연구

Synthesis, Characterization, and Application of Morphology-Controlled Semiconductor Nanostructures

2016 년 2 월

서울대학교 대학원

화학부 물리화학 전공

김 형 배

A Ph. D. Dissertation

Synthesis, Characterization, and Application of Morphology-Controlled Semiconductor Nanostructures

By Hyung-Bae Kim

Supervisor: Professor Du-Jeon Jang

Major: Physical Chemistry

Department of Chemistry

Graduate School of Seoul National University

February 2016

형태가 제어된 반도체 나노구조의 합성, 분석 및 응용에 대한 연구

Synthesis, Characterization, and Application of Morphology-Controlled Semiconductor Nanostructures

지도교수 장두전

이 논문을 이학박사 학위논문으로 제출함

2016년 2월

서울대학교 대학원

화학부 물리화학 전공

김 형 배

김형배의 박사학위논문을 인준함

2016년 2월

위 원 장 강 헌 (서명) _____

부 위 원 장 장두전 (서명) _____

위 원 정택동 (서명) _____

위 원 정연준 (서명) _____

위 원 권오훈 (서명) _____

Abstract of Dissertation

In this dissertation, synthesis, characterization, and applications of morphology-controlled semiconductor nanostructures are discussed from the point of views of the physical chemistry and materials chemistry. Hyung-Bae Kim and his supervisor Du-Jeon Jang have developed four unique synthetic approaches for the preparation of morphology-controlled nanostructures: (1) the co-precursor method, (2) the defect-driven method, (3) the co-solvent method, and (4) the additive assisted method. Two heating methods of microwave-assisted methods and hydrothermal methods are selectively employed for the preparation of morphology-controlled nanostructures. The formation mechanisms of all the presented methods are delicately proposed in terms of LaMer theory. In addition, the morphology-dependent photophysical, photocatalytic, and photovoltaic properties of the prepared nanostructures have been investigated for potential applications. Brief overviews of the Chapters 1-5 mentioned in this dissertation are given below.

In Chapter 1, basic concepts of nanoscience especially on semiconductor nanostructures are introduced. The physical and chemical properties of nanosized anisotropic materials show the direction-dependent quantum confinement effects. The morphology-dependent properties of anisotropic nanostructures are summarized in three categories: sizes, shapes, and the surface conditions. The fundamental formation theories of nanostructures and

the several factors that affect the growth kinetics of nanostructures are thoroughly explained.

In Chapter 2, the unique phenomenon of precursor-dependent shape variations of CdSe nanostructures are discussed. Spherical and branched CdSe nanostructures have been fabricated by employing two intrinsically different cadmium precursors of $CdCl_2$ and CdO, respectively. Whereas $CdCl_2$ precursors are polyol-soluble, CdO precursors are polyol-insoluble. We have also selectively employed two different polyol solvents having significantly different boiling temperature and viscosity. Due to the differences in synthetic conditions, each precursor has proceeded through the different growth pathways, generating the morphology-controlled CdSe nanostructures. The mechanism of precursors-dependent morphological variation of CdSe nanostructures are discussed. Combining the advantage of respective precursors, we have successfully synthesized novel structures of sphere-decorated CdSe tetrapods by using co-precursors of $CdCl_2$ and CdO.

In Chapter 3, defect-driven synthesis of porous CdSe nanostructures having a near infrared emission at room temperature. It is worth emphasizing in that the defect-engineered preparation of nanostructures has been rarely reported. Porous CdSe nanorods have been prepared faciley *via* the hydrothermal treatment of $CdSe{\cdot}(en)_{0.5}$ nanorods. During the hydrothermal process, various crystalline imperfections appear due to lattice mismatches between orthorhombic $CdSe{\cdot}(en)_{0.5}$ and hexagonal wurzite porous CdSe nanorods and subsequently dissapear to release mismatch strains. In the self-healing defects

process, point defects of atomic vacancies are heavily generated near the planar defects of twin boundaries in CdSe nanorods to produce volume defects of voids eventually. The emission of CdSe nanorods shifts to the red and decreases in intensity with the increase of surface states and selenium vacancies. The mean lifetime of emission increases with the increase of the hydrothermal-treatment time as the fractional amplitude of a surface-state-related component increases.

Chapter 4 focuses on two subjects; (1) the strategies and formation mechanisms of morphological variation of anatase TiO_2 nanostuctures (Chapter 4A) and (2) their photocatalytic and photovoltaic applications (Chapter 4B). The morphologies of anatase TiO_2 crystals have been varied facilely from rod-like structures to various hedgehog-like hierarchical structures *via* forming titanium glycerolate precursors as sacrificial templates. The morphologies of the precursors have been controlled readily under microwave irradiation by adjusting the relative solvent volumes of isopropanol and glycerol. The variation of the relative volume fractions of isopropanol and glycerol having significantly different boiling points and viscosity values has changed the nucleation and growth kinetics to control the morphologies as well as the sizes of titanium glycerolate precursors. In this studies, it has been founded that hierarchical 3D nanostructures have 5.5 times higher photocatalytic activity than rod-like 1D nanostructures, and the DSSC efficiency of hierarchical 3D nanostructures becomes as high as 5.37%, which is 50% higher than the DSSC efficiency of 1D nanostructures.

In Chapter 5, the ammonia-assisted synthesis of morphology-controlled ZnO microstructures under microwave irradiation is discussed. The morphologies and the surface conditions of ZnO microstructures have been controlled facilely *via* a one-pot synthetic route by varying the ammonia concentration of the reaction mixture. Ammonia affects the nucleation, growth, and hydrolysis kinetics of intermediate zinc glycerolate to induce shape variation from flower-like ZnO microstructures to various ZnO twin microstructures with the preferred exposure of ±(0001) polar planes. As-prepared ZnO microstructures are mesoporous with large specific surface areas and high specific pore volumes, which have resulted from the microwave-assisted fast hydrolysis of intermediate zinc glycerolate microstructures. Owing to the novel features of microwave, ZnO microstructures have numerous microcracks and wrinkles on their surfaces and show characteristic defect-driven orange emission, whose intensity increases with the specific surface area. The photocatalytic degradation rate constant of rhodamine B *via* our prepared ZnO microstructures have been founded to increase linearly with the specific surface area, the specific pore volume, and the polar-surface exposure. Our simple and rapid microwave-assisted synthetic method is considered to be beneficial to the development of morphology-controlled metal oxides that are applicable for eco-friendly waste-water treatment.

Keywords: Semiconductors, Spectroscopy, Nanoscience, Nanotechnology, Photocatalysts, Dye-sensitized solar cells *Student Number:* 2010 – 20273

Table of Contents

List of Figures and Tables

Figure 2-5 (top) Maximum-normalized XPS spectra of as-prepared CdSe crystals produced at X values of 0 (red) and 0.8 (green) in ethylene glycol. (bottom) EDX spectra of CdSe crystals grown in ethylene glycol for 10 min at X values of 0 (a) and 0.8 (b). The Si peak has originated from the silicon wafer substrate

Figure 2-6. Extinction spectra (a) and scattering-removed absorption-edge spectra (b) of CdSe crystals produced at X values of 0 (red) and 0.8 (green) in ethylene glycol. The samples were suspended in ethanol at room temperature. The inset shows the plots of $(\alpha h\nu)^2$ vs hν to estimate E_g.

Figure 2-7. Photoluminescence spectra of CdSe crystals produced in ethylene glycol at various X values indicated inside. The samples were suspended in ethanol at room temperature and excited at 355 nm.

Figure 2-8. TEM images of CdSe crystals grown in glycerol for 10 min at X values of 0 (a) and 1.0 (b). The scale bar of the inset indicates 300 nm. LaMer plots (c) for the formation of CdSe crystals grown at X values of 0 (red) and 1.0 (blue) in glycerol. Sc indicates critical supersaturation.

Figure 3-1 Schematic illustration for the formation of porous CdSe nanorods *via* the hydrothermal treatment of $CdSe \cdot (en)_{0.5}$ nanorods. The formation mechanism is depicted as a function of the hydrothermal-treatment time.

Figure 3-2 TEM (left) and HAADF-STEM images (right) of indicated nanostructures

Figure 3-3 HRTEM image (a), FFT pattern (b), and STEM-EDX elemental profiles (c,d), scanned along the lines in the HAADF images of the insets, of a CE12 porous nanorod.

Figure 3-4 HRXRD patterns of indicated nanostructures. The standard diffraction pattern of CdSe (JCPDS No. 08-0459) is also shown in the bottom.

Figure 3-5 HRTEM images of indicated nanostructures. Yellow lines mark planar defects while pink lines and white arrows indicate lattice alignments and pore regions, respectively.

Table 3-1. Parameters of the XPS Spectra in Figure 3-6.

Figure 3-6 XPS spectra of indicated nanostructures.

Figure 3-7 Photoluminescence spectra of indicated nanostructures suspended in ethanol with excitation at 355 nm.

Figure 3-8. Photoluminescence kinetic profiles of indicated nanostructures suspended in ethanol at room temperature, and solid lines are best-fitted curves to extract kinetic constants.

Table 3-2. Photoluminescence Decay Constants Extracted from Figure 8

Figure 4A-1 Schematic illustration for two-step synthetic processes of anatase TiO_2 crystals under microwave irradiation.

Figure 4A-2 SEM images of as-prepared titanium glycerolate precursors P00 (a), P20 (b), P40 (c), and P67 (d). Each scale bar indicates 1 μm, whereas the scale bar inside the inset indicates 200 nm.

Figure 4A-3 SEM images of anatase TiO_2 A00 (a), A20 (b), A40 (c), and A67 (d) produced by the hydrolysis of titanium glycerolate precursors P00, P20, P40, and P67, respectively. Each scale bar indicates 1 μm, whereas the scale bar inside the inset indicates 200 nm.

Figure 4A-4 TEM images of titanium glycerolate P40 (a,b) and anatase TiO_2 A40 (c,d).

Figure 4A-5 HRXRD patterns of indicated titanium glycerolate precursors and anatase TiO_2 crystals. The standard diffraction pattern of anatase TiO_2 is also shown in the bottom.

F

igure 4A-6 TGA curves of indicated titanium glycerolate precursors and anatase TiO_2 crystals.

Figure 4A-7 FTIR spectra of glycerol, indicated titanium glycerolate precursors, and indicated anatase TiO_2 crystals: (1) O-H stretching at 3500 ~ 3000 cm^{-1}, (2) O-H bending at 1440 cm^{-1}, (3) C-C-O stretching at 1121 cm^{-1}, (4) Ti-O-C stretching at 813 cm^{-1}, and (5) Ti-O-Ti stretching at 612 cm^{-1}.

Figure 4A-8 O 1s XPS spectra of indicated titanium glycerolate precursors (left) and anatase TiO_2 crystals (right). Each XPS spectrum has been deconvoluted into three Gaussian curves arising from indicated oxygen environments.

Figure 4A-9 Plausible growth mechanisms of titanium glycerolate precursors.

Figure 4B-1. Schematic illustration of morphology-depenedent photocatalytic (left) and photovoltaic performances (right) of as-synthesized rod-like (a) and hedgehog-like anatase TiO_2 crystals (b).

Figure 4B-2. SEM images (a,b), HRTEM images (c,d), and FFT patterns (e) of anatase TiO_2 nanostructures A00, A20, and A67.

Figure 4B-3 N_2 adsorption-desorption isotherms (a) and pore-size distributions (b) of indicated anatase TiO_2 crystals.

Figure 4B-4. UV-visible diffuse reflectance spectra (a), Kubelka-Munk plots of the reflectance spectra to find indirect band-gap energies (b), valence-band XPS spectra (c),

Figure 4B-5. Photocatalytic oxidation curves of isopropanol *via* indicated anatase TiO_2 crystals under UV-visible irradiation for remnant isopropanol (a), evolved acetone (b), and evolved CO_2 (c) as a function of irradiation time.

Figure 4B-6. Photocatalytic reduction curves of CO_2 by using anatase TiO_2 crystals A67 and commercial TiO_2 Degussa P25 under UV-visible irradiation.

Figure 4B-7 $J-V$ curves of DSSCs based on as-synthesized anatase TiO_2 crystals A00 (red), A20 (green), A40 (orange), and A67 (blue) with (a) and without (b) a light-shading mask.

Figure 5-1 SEM images of ZnO microstructures having various morphologies prepared at different ammonia concentrations of (a) 0.0 mM, (b) 43 mM, and (c) 170 mM.

Figure 5-2 HRXRD patterns of ZnO microstructures having various morphologies prepared at indicated ammonia concentrations. The relative maximum intensity of each peak is shown on a dashed line, and the standard diffraction pattern of hexagonal wurtzite ZnO is also shown in the bottom.

Figure 5-3 (a) TEM images, (b) HRTEM images observed from the indicated square regions of the TEM images, and (c) atomic density profiles scanned along dashed lines in the HRTEM images of (top) flower-like and (bottom) burger-like ZnO microstructures. The insets show FFT patterns.

Figure 5-4 (a) N_2 adsorption-desorption isotherms and (b) pore-size distributions of ZnO microstructures prepared at indicated ammonia concentrations.

Figure 5-5 (a) UV-visible extinction spectra and (b) photoluminescence spectra with excitation at 266 nm of ZnO microstructures prepared at indicated ammonia concentrations. The inset shows the plots of $(\alpha h\nu)^2$ *vs* $h\nu$, where α is the absorption coefficient and $h\nu$ is the photon energy.

Figure 5-6 Hydrodynamic size evolution of ZnO microstructures prepared at indicated ammonia concentrations, measured by DLS in water. Each datum point represents the standard deviation of three measurements. The obtained data have been fitted to single-exponential growth functions ($y=a\cdot e^{-kt}+b$), resulting in rate constants (k) of 1.26×10^{-2} s^{-1} (0 mM), 1.54×10^{-2} s^{-1} (43 mM), and 1.67×10^{-2} s^{-1} (170 mM).

Figure 5-7 (a) SEM images of burger-like ZnO microstructures synthesized for indicated reaction times. Each scale bar indicates 1 μm. (b) HRXRD patterns of ZnO microstructures prepared at 170 mM of ammonia for indicated reaction times. The standard diffraction pattern of the hexagonal wurtzite ZnO is also shown in the bottom.

Figure 5-8 Plausible mechanisms for the ammonia-assisted growth of ZnO microstructures under microwave irradiation at two different ammonia concentrations (a) and a time-dependent growth mechanism at a particular ammonia concentration of 170 mM.

Figure 5-9 (a) First-order kinetics, $\ln(A/A_0)$ vs. irradiation time, for the photocatalytic degradation of 10 μM rhodamine B (aq) *via* different ZnO microstructures prepared at indicated ammonia concentrations under irradiation of a 300 W Xe lamp. The calculated rate constants were 0.031 s^{-1} (0 mM), 0.038 s^{-1} (43 mM), 0.050 s^{-1} (170 mM), 0.045 s^{-1}(255 mM). (b) The variation of rate constants as functions of surface area, pore volume, and (0001)/ $(10\bar{1}0)$ ratio.

Chapter 1. General Introduction

1. 1. Nanosized and Nanostructured Materials

What Are Nanoparticles?

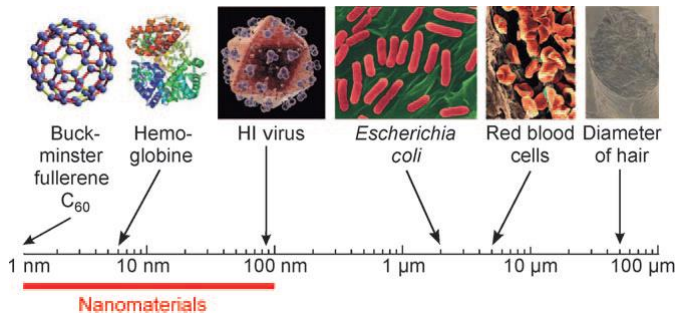

Figure 1-1 Length scale of nanoparticles. Reproduced from ref. 1.

"Nanomaterials" is typically used to refer to objects having certain dimension length scales approaching the unit of 10^{-9} m (Figure 1-1). The synthesis of nanocrystalline particles with sizes ranging from 1 to 100 nm has been intensively explored because nanoparticles exhibit unique properties that cannot be achieved by their bulk counterparts.[1] The characteristic feature of nanoparticles is attributed to the large surface-to-volume ratios. For example, a single cube with edges 1 cm of length can be divided into 10^{21} cubes with edges 1 nm of length, generating that the number of individual cubes and their total surface area increases dramatically. The total surface area of 6000 m^2 for the 10^{21} nanocubes is comparable to the area of a football game field of 7000 m^2.[1] Since nanoparticles are strongly influenced by their surface areas, unsaturated bonding sites and unoccupied coordination sites on their surfaces, surface conditions can play a major role in reactivity of nanocrystals. Thus, the

increasing number of exposed surface atoms determines chemical properties of nanoparticles.[1-4]

In the intermediate size range between molecular and bulk matter, continuous energy bands of bulk solids become discrete and their energy separations display an analytic dependence on the spatial dimension of the material. This is illustrated conceptually in Figure 1-2, which expresses the transformation of the electronic density of states (DOS) of valence and conduction bands in metals and semiconductors from continuous to discrete to individual in bulk, which is called as quantum-confined effects. Quantum confinement effects can be observed when the diameter of a material have similar magnitude as the de Broglie wavelength of the electron wave function (Figure 1-2). As the length of confining quantum well decreases and reaches a certain limit, called the exciton Bohr radius, the energy spectrum becomes discrete, exhibiting that their electronic and optical properties deviate substantially from those of bulk materials.[1]

The most popular demonstration of the size-dependent characteristics of nanocrystals is quantum dots (QDs) whose continuous fluorescent emission covers the entire visible spectrum as a function of their sizes. Especially, quantum-confinement in semiconductors results also from the direction-dependent quantum confinement of electrons and holes as bound pairs known as excitons, the representative scheme is shown in Figure 1-3. The exciton Bohr radius provides an approximate dimension for the onset of quantum-confinement effects. When an electron–hole pair is squeezed into a nanocrystal

within the bulk exciton Bohr radius, the effective bandgap of the semiconductor increases. The larger the effective bandgap shows the effective electron–hole recombination.[1]

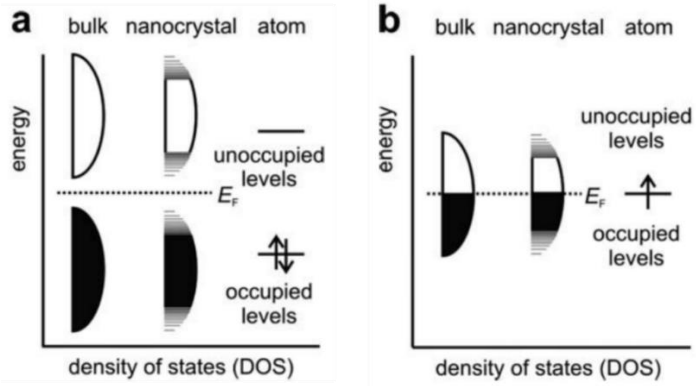

Figure 1-2 Schematic illustration of three density of states of bulk, nanocrystal, and an isolated atom for semiconductor (a) and metal (b). Reproduced from ref. 1.

1. 1. 1. Anisotropic Nanomaterials: Sizes, Shapes, and Surface Effects on the Properties of Nanostructures

The anisotropy of nanomaterials has attracted great attention due to its useful tool for engineering the properties of nanomaterials with attractive features. The development and characterization of anisotropic nanostructures has been strongly encouraged due to their direction-dependent chemical properties. Thus, anisotropic nanomaterials started to get attention for the whole ranges of shapes. Comprehensive knowledge about the anisotropic nanomaterials is important in

designing devices with desired functions. Due to this reason, systematic efforts have been made to synthesize anisotropic materials with diverse shape in the nanoscale regime. Their unique physical and chemical properties make them ideal candidates for designing new applications in nanotechnology. Thus, the zero-dimensional (0D), one-dimensional (1D), two-dimensional (2D), and three-dimensional (3D) arrays of anisotropic nanoparticles brings novel properties into nanoparticles, which would be entirely different from the properties of spherical isotropic nanoparticles (Figure 1-3).

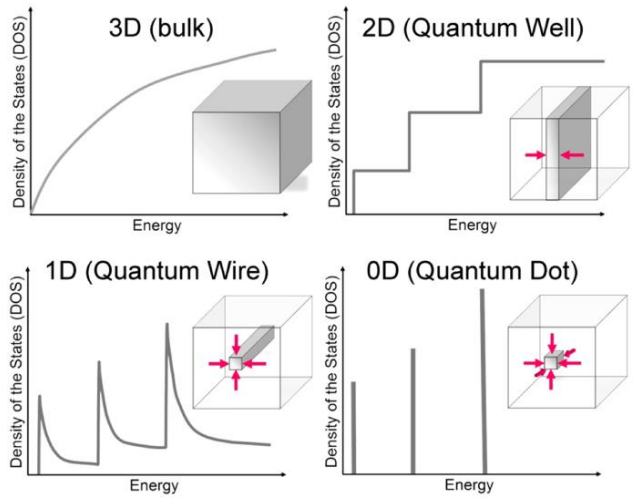

Figure 1-3 Direction-dependent electronic density of states. Reproduced from ref. 2.

1. 1. 2. Preparation of Anisotropic Nanostructures

Nanocrystal synthesis in the “bottom-up” approach, which is different from physical methods in “top-down” approach, is generally employed in solution-phase colloidal chemistry. The advantage of the physical methods is the production of a large quantity of nanocrystals but the control of sizes and size distributions is very difficult to achieve. In contrast, solution-based chemical synthetic methods can be used to synthesize uniform nanocrystals with controlled particle sizes. Furthermore, various-shaped nanocrystals can be synthesized by varying the reaction kinetics. Thus, this chapter focuses primarily on the advances on the synthesis of the morphology-controlled synthesis by solution-based chemical approaches.

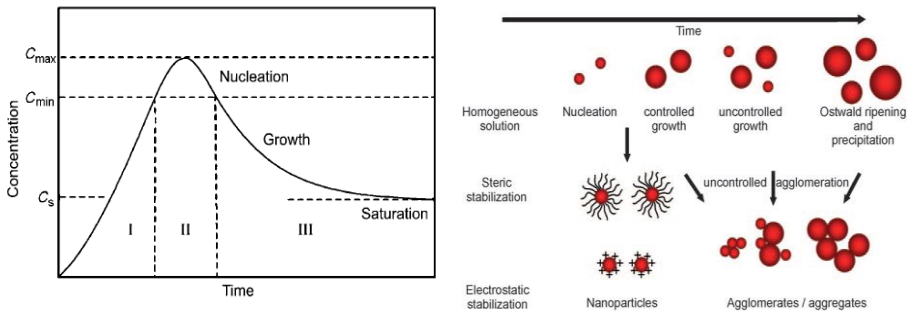

Figure 1-4 LaMer and Dinegar’s model to describe nucleation and nucleus growth (left). Growth and stabilization of nanoparticles (right). Reproduced from ref. 1.

According to the model of LaMer and Dinegar, nucleation is an endothermic process, which includes the various energies that the dissociation energy of chemical bonds in the initial compounds, the removal of solvate shells,

and overcoming the surface tension of the solvent require energy.[1,,7,8] Nucleus growth and Ostwald ripening, however, are exothermic processes that release the enthalpy of formation energy of crystal lattices. Therefore, the growth of nuclei is always energetically favored for nanoparticles. The agglomeration of the nanoparticles is also energetically favored, as it minimizes surface areas and saturates the bonding and coordination sites, which is useful to establish a high degree of supersaturation at high temperature in the homogeneous phase. The particle surfaces should be saturated immediately after nucleation by electrostatic or steric stabilization to protect the nanoparticles from further growth or agglomeration. Electrostatic stabilization can be achieved by targeted adsorption of ions ($RCOO^-$, RSO^{3-}, R_4N^+, etc.) on the particle surface. Steric stabilization is realized by adsorption of long-chain organic molecules (e.g. oleyl amine, oleic acid, trioctyl phosphine, trioctyl phosphine oxide). This protection methods can also affect the growth kinetics of formation of nanocrystals and eventually the morphology of nanocrystal are changed.[3]

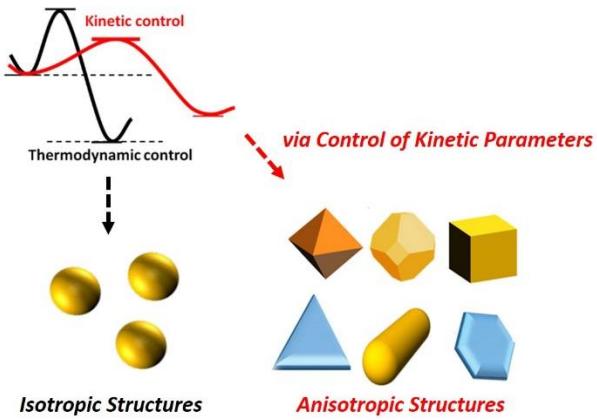

Figure 1-5 Preparation of anisotropic materials.

The following is explanation of major three words used in crystal growth mechanisms. *Nucleation:* nucleation is defined as the series of solid clusters formation by which the atoms or molecules of a reactant phase rearrange into a instantly existent cluster to grow irreversibly to a macroscopically large enough size. The cluster is defined as nucleus. While nucleation can be homogeneous in the absence of foreign particles or crystals in the solution, nucleation can be heterogeneous in the presence of foreign particles in the solution. Both types of nucleation are collectively known as primary nucleation. Secondary nucleation takes place when nucleation is induced by the presence of crystals of the same substance. The rate of nucleation can be generally expressed by an Arrhenius-type equation. It can be seen in this plot that the nucleation rate is virtually zero until a critical value of supersaturation is achieved, after which the rate increases exponentially. This critical supersaturation ($\Delta\mu_c$) defines the so-called metastable zone where crystal growth can proceed without continuous nucleation taking place. *Supersaturation:* the driving force needed for the nucleation and growth of a crystal is referred to as *supersaturation* and is defined as the difference in chemical potential between a molecule in solution and that in the bulk of the crystal phase ($\Delta\mu = \mu_s - \mu_c$, where μ_s is the chemical potential of a molecule in solution and μ_c is the chemical potential of the molecule in the bulk crystal). Following thermodynamics equation can be expressed as $\Delta\mu = kT \ln S$, where k is the Boltzmann constant, T is the absolute temperature, and S is the supersaturation ratio. When $\Delta\mu > 0$ the solution is said

to be supersaturated, meaning that nucleation and growth events are possible, whereas when $\Delta\mu < 0$ the solution will be unsaturated and dissolution will take place. *Crystal Growth:* crystal growth is the series of processes by which an atom or a molecule is incorporated into the surface of a soild crystal, causing an increase in macroscopic sizes. The total processes of nucleation can be summarized into four steps; (1) transport of atoms through solution; (2) attachment of atoms to the surface; (3) movement of atoms on the surface; (4) attachment of atoms to edges and kinks. The first process is the so-called transport process, whereas (2)–(4) are referred to as surface processes. Since these different steps normally occur in series, the slowest process will control the overall crystal growth. Therefore, growth can strongly depend on the transport step when step (1) is the slowest or surface controlled when steps (2)–(4) are the slowest.[4-6]

1. 2. Principles of Microwave-Assisted Synthetic Methods and Solvothermal/Hydrothermal Synthetic Methods

"Time is valuable". This quote is true especially for scientists in the field of synthetic chemistry often a large number of time-consuming experiments. Any new synthetic techniques that help to save time would be extremely beneficial. Microwave definitively fulfils the fast chemical synthesis. Thus, microwave ovens became an indispensable tool in modern organic and inorganic synthesis.

In particular, the synthesis of nanoparticles and nanostructures, whose growth is highly sensitive to the reaction conditions, could benefit from the efficient microwave dielectric heating.[5-7]

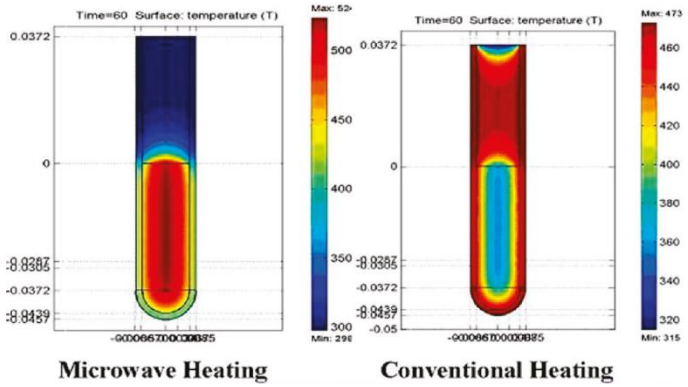

Figure 1-5. Temperature profiles affected by MW irradiation and oil-bath. Reproduced from ref. 6.

Microwave heating does not only reduce the chemical reaction times by several orders of magnitude but also suppresses side reactions and thus improves the yield. The controllable synthesis of nanoparticles *via* microwave irradiation been recognized to be an important technique for better regulating nanocrystal formation and enhancing product quality. Microwave irradiation raises the temperature of the whole reaction volume simultaneously, whereas in the oil heated tube the reaction mixture in contact with the vessel wall is heated first. Therefore, the modern microwave reactors are specifically designed for chemical synthetic applications, which allows an exquisite control and exact *in-situ* characterization of the reaction temperature and pressure inside the reaction vessel. Considering the fact that the energy of a microwave photon at a

frequency of 2.45 GHz is much too low to cleave chemical bonds,[8-12] microwave-assisted nanoparticle synthesis is based on the efficient dielectric heating by absorbing microwave energy and converting it into heat.

The dielectric heating mechanism involves two main processes, namely dipolar polarization and ionic conduction. Microwave irradiation at the sample results in the alignment of the dipoles or ions in the electric field.[4] The electromagnetic radiation generates an oscillating field, the dipoles or ions continuously attempt to realign themselves in the electric field. As a results, different amounts of heat are produced through molecular friction and dielectric loss. The rotations of many polar molecules can produce resistive heating in the reaction medium. The process is generally called as dielectric loss. In the case of ionic conduction, the dissolved charged molecules oscillate back and forth under the influence of the microwave irradiation and then collide with adjacent molecules and thus generate heat.

The ability of a specific material or solvent to convert MW energy into heat at a given frequency and temperature is determined by the factors, so-called loss tangent (tanδ).[4] The loss tangent is expressed as the quotient $\tan\delta = e''/e'$, where e'' is the dielectric loss, indicative of the efficiency with which the electromagnetic radiation is converted into heat, and e' is the dielectric constant describing the polarizability of molecules in the electric field. When a reaction medium has a high tanδ at the standard operating frequency of a MW reactor (2.45 GHz), the reaction medium have good absorption and, consequently, for

efficient heating. Overall, solvents used in MW chemistry can be classified as high- (> 0.5), medium- (0.1–0.5), and low-absorbing (< 0.1).[5,7]

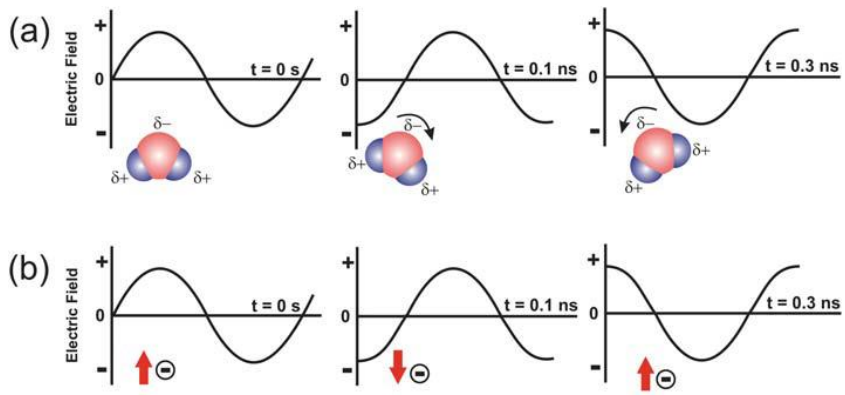

Figure 1-6. Two dielectric heating mechanisms of (a) dipolar polarization and (b) ionic conduction mechanism. Reproduced from ref. 3

Hydrothermal technique can be defined as a synthetic method of single crystals that depends on the solubility of minerals in hot temperatures and under high pressure.[11] In this case, the crystal growth is performed in an apparatus consisting of a steel pressure vessel, which is called as a Teflon-lined stainless-steel autoclave. The wet-chemical based hydrothermal and solvothermal synthetic routes have attracted great attention due to their advantages of environmental friendliness, easy upward scaling, and low production cost. Solvothermal synthesis is very similar to the hydrothermal route where the synthesis is conducted in a stainless steel autoclave, the only difference being that the precursor solution is usually not aqueous. However, this is not always the case in all literature uses of the expression.[11] The solvothermal route can

gain benefits especially for the sol-gel reactions. Thus solvothermal synthesis can be employed for the precise control over the size, shape distribution, and crystallinity of nanostructures, which is easily achieved by changing certain experimental parameters, including reaction temperature, reaction time, solvent type, surfactant type, and precursor type.[11,12]

1. 4. References

(1) H. Goesmann, C. Feldmann, *Angew. Chem. Int. Ed.* 2010, **49**, 1362−1392.

(2) Y.-W. Jun, J.-S. Choi, J. Cheon, *Angew. Chem. Int. Ed.*, 2006, *45*, 3414-3439.

(3) I. Bilecka, M. Niederberger, *Nanoscale*, 2010, 2, 1358-1374.

(4) M. Baghbanzadeh, L. Carbone, P. D. Cozzoli, C.O. Kappe, *Angew. Chem. Int. Ed.*, 2011, **50**, 11312-11359.

(5) J. Park, J. Joo, S. G. Kwon, Y. Jang, T. Hyeon, *Angew*. *Chem*. *Int*. *Ed*. 2007, **46**, 4630-4660.

(6) M. N. Nadagouda, T. F. Speth, R. S. Varma, *Acc. Chem. Res.*, 2011, **44**, 469-478.

(7) H.-B. Kim, D.-J. Jang, *CrystEngComm*, 2012, **14**, 6946-6951.

(8) Y. Kim, H.-B. Kim, D.-J. Jang, *J. Mater. Chem. A*, 2014, **2**, 5791-5799.

(9) H.-B. Kim and D.-J. Jang, *CrystEngComm*, 2015, **17**, 3325-3332.

(10) H.-B. Kim, H. Kim, W. I. Lee and D.-J. Jang, *J. Mater. Chem. A*, 2015, **3**, 9714 - 9721.

(11) H.-B. Kim and D.-J. Jang, *Nanoscale*, 2016, **8**, 403 - 410.

(12) H.-B. Kim, D. W. Jeong and D.-J. Jang, *CrystEngComm*, 2016, (DOI: 10.1039/C5CE02334C).

Chapter 2. Precursor-Dependent Shape Variation of Wurtzite CdSe Crystals in a Microwave-Assisted Polyol Process[†]

[†]This is reproduced from Hyung-Bae Kim and Du-Jeon Jang, *CrystEngComm*, **2012**, *14*, 6946-6951.

2. 1. Abstract

We report a unique synthetic approach to fabricate CdSe crystals with tunable morphology and optical properties via a microwave-assisted polyol process. The morphology of CdSe crystals has been controlled by adjusting the relative amounts of two cadmium precursors $CdCl_2$ and CdO in a polyol solvent of ethylene glycol or glycerol; spheres, pebbles, sheets, and tetrapods of CdSe wurtzite structures with their sizes ranged from nanometers to sub-micrometers have been prepared facilely under microwave irradiation. The growth mechanism is discussed in terms of the LaMer theory; the nucleation and growth kinetics of CdSe, which depends decisively on cadmium precursors and polyol solvents, determines the shapes and sizes of diverse CdSe crystals.

2. 2. Introduction

The controlled fabrication of nanostructured materials having functional properties is of fundamental importance in the nanotechnology.[1-3] In particular, semiconductor nanocrystals whose electronic structures can be easily tuned by controlling their sizes, shapes, and compositions have been extensively explored.[4-8] Much effort has been devoted to obtain the precise shape control of semiconductor nanocrystals, which is determined by both kinetic and thermodynamic factors.[9-11] CdSe having a bulk band gap of 1.74 eV has been considered to be a most promising II-VI semiconductor material. Diverse synthetic methods of wurtzite CdSe crystals having unique structures such as wires, rods, spheres, and branched types have been attempted extensively because those shapes provide new properties, which can be exploited into useful applications for optoelectronic devices, optical sensing, and solar cells.[2,12,13]

Novel microwave-assisted liquid-phase routes have attracted great attention to control the reaction parameters in alternative access. It is significantly different from conventional heating systems that microwaves can penetrate the container wall, selectively excite molecules or ions, and trigger heating by two main mechanisms: dipolar polarization and ionic conduction.[14] So these features not only reduce the reaction times by several orders of magnitude but also suppress side reactions.[14-15] Polyol solvents have been frequently employed in microwave irradiation systems because

high loss-tangent values of polyols lead them to convert microwave energy efficiently into heat. Additionally, polyols can be used as reducing agents as well as solvents for redox reactions. Thus, these facts could make microwave-assisted polyol methods be environment-friendly.[16]

Until now, the tuning of inorganic structures *via* microwave-assisted synthetic methods has been demonstrated by controlling various reaction conditions such as reducing agents, surfactants, solvents, and capping reagents.[14-19] However, controlling those factors still involves challenging problems. In this paper, we will report that the diverse shapes and sizes of CdSe crystals have been tuned facilely by adjusting cadmium precursors and polyol solvents in a microwave-assisted process. So far, precursor-dependent shape control has been rarely reported either under microwave irradiation or in a conventional heating system.[20-21] The crucial factor that determines the shapes of CdSe crystals is the relative amounts of two cadmium precursors: $CdCl_2$ and CdO. To understand the formation mechanisms of CdSe crystals with various shapes and sizes, we have intensively investigated the structures and properties of CdSe crystals fabricated at specific relative amounts of $CdCl_2$ and CdO in two different polyol solvents.

2. 3. Experimental Details

Preparation of CdSe Crystals. The controlled fabrication CdO(s, ≥ 99.99%), $CdCl_2$(s, ≥ 99.99%), Se(s, ≥ 99.999%), ethylene glycol(l, ≥ 99%), and glycerol(l, ≥ 99%) were used as purchased from Sigma-Aldrich. Ethylene glycol and glycerol were used as solvents and reducing agents in polyol processes. For the synthesis of CdSe crystals, $CdCl_2$(s) and CdO(s), whose total chemical amount was 1.0 mmol, were added with variation of $[CdCl_2]/([CdO] + [CdCl_2])$ (X) to 20 mL of ethylene glycol or glycerol containing 1.0 mmol of Se(s). To make those precursors dispersed homogeneously into the solvent, the mixture was maintained at 50 ℃ for 30 min under vigorous stirring and sonicated in an ultrasonic bath for 5 min. The mixture was then subject to irradiation of 2.45 GHz from a 450 W Samsung HV-367AWJ microwave system for 10 min. The precipitate was repeatedly centrifuged and washed with deionized water and ethanol, and the final product was dried in a vacuum at 50 ℃ for 12 h.

Characterization. While transmission electron microscopy (TEM) images were measured using a JEOL JEM-2000 microscope, fast Fourier transform (FFT) patterns and high resolution TEM (HRTEM) images were measured with a JEOL JEM-3000F microscope. The morphology of CdSe crystals was measured with a JEOL JSM-6700F field-emission scanning electron microscope (FESEM) equipped with an energy-dispersive X-ray (EDX) spectroscope. High resolution X-ray diffraction (HRXRD) patterns were

recorded with a MAC Science M18XHF-SRA diffractometer using Cu Kα radiation (λ = 0.154056 nm). The scanning 2θ angle was varied from 20° to 70° at a scanning rate of 5° min^{-1}. High-resolution X-ray photoelectron spectroscopy (HRXPS) data were obtained using a Sigma Probe ThermoVG photoelectron spectrometer with an excitation source of Al Kα radiation (1486.7 eV). Photoluminescence spectra were detected using a Princeton Instruments ICCD576G CCD attached to a 0.5 m Acton Research SpectraPro-500 spectrometer with excitation using 355 nm pulses from a Q-switched Quantel Brilliant Nd: YAG laser of 6 ns.

2. 4. Results and Discussion

CdSe crystals synthesized at an X value of 0 in ethylene glycol via a microwave-assisted polyol process are considered to be nanospheres having an average diameter of 60 nm (Figure 2-1, top) although their surfaces are not perfectly round and smooth. Thus, our CdSe nanospheres have high surface-to-volume ratios as so called nanoflowers.[22] Although the preparation of CdSe nanospheres, named as nanoballs, via a microwave-assisted polyol method has been reported,[23] our prepared CdSe nanospheres are much smaller, more monodispersive, better crystallized, and more enhanced in optical properties (see below). However, CdSe crystals grown

at an X value of 0.8 Figure 2-1, bottom) are quite different from CdSe nanospheres grown at an X value of 0 in morphology. They are mostly tetrapods and the average diameter and length of their arms are found to be 180 and 680 nm, respectively. Looking carefully at the surfaces of the arms, we can find that the arms of the tetrapods are decorated with nanoparticles of 50 nm in diameter. To our knowledge, decorated CdSe tetrapods have not been reported yet.

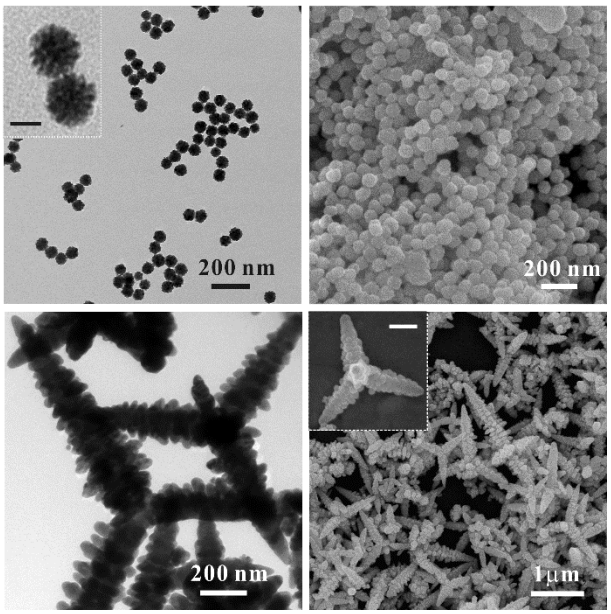

Figure 2-1. TEM (left) and FESEM images (right) of CdSe crystals grown at X values of 0 (top) and 0.8 (down) in ethylene glycol for 10 min. Scale bars inside insets indicate 50 nm (top) and 200 nm (down).

The HRTEM images of Figure 2-2 show clear lattice-fringe images of CdSe crystals prepared at X values of 0 and 0.8 in ethylene glycol. The interplanar distances of 0.212 and 0.326 nm observed with the lattice fringes in Fig. 2a accord reasonably with the spacings of 0.216 nm between the (110)

planes and 0.331 nm between the (101) planes, respectively, of the reference wurtzite CdSe (JCPDS No. 08-0459). The average d-spacing values of 0.212 nm and 0.329 nm calculated from the diffraction spots in the FFT pattern of Figure 2-2a also agree fairly with the spacings of the (110) and (101) planes, respectively, of the reference wurtzite CdSe. The ring-like shape of the FFT pattern and the incomplete accordance of the interplanar distances with the respective ones of the reference wurtzite CdSe indicate that CdSe nanospheres grown at an X value of 0 are polycrystalline. The lattice fringe distance of 0.351 nm in Figure 2-2b agrees well with the d-spacing length of the (002) planes of the reference wurtzite CdSe, indicating that the arm structure has grown anisotropically along the c-axis; the tetrapod structure has been known to have four hexagonal arms equivalently grown along the [0001] or $[000\bar{1}]$ direction on the zinc blended core with four {111} facets.[24-27] However, unfortunately, we cannot observe the central core region of the tetrapod structure due to the high density of atoms. The average d-spacing value calculated from diffraction spots in the FFT pattern of Figure 2-2b also agrees well with the spacing of the (002) planes of the reference hexagonal wurtzite CdSe. The discrete dot shapes of the FFT pattern and the single lattice-fringe pattern of the HRTEM image in Figure 2-2b suggest that compared with CdSe nanospheres grown at an X value of 0, decorated CdSe tetrapods grown at an X value of 0.8 are highly crystalline.

The HRXRD patterns in Figure 2-3 of CdSe crystals grown at both X values of 0 and 0.8 match well with the pattern of the reference hexagonal

wurtzite CdSe (JCPDS No. 08-0459) although decorated CdSe tetrapods grown at an X value of 0.8 seem to be more crystalline than CdSe nanospheres grown at an X value of 0 as already suggested with the HRTEM images of Figure 2-2. The bandwidths of the HRXRD peaks of decorated CdSe tetrapods are much narrower than the respective ones of CdSe nanospheres. This implies that the mean crystallite size of the tetrapods grown at an X value of 0.8 is much larger than that of nanospheres grown at an X value of 0. In order to calculate the mean crystallite size (D), we have applied the (002) peak to the Scherrer equation $<D> = 0.94\,\lambda/(\beta\cos\theta)$ where λ is the X-ray wavelength, θ is the Bragg diffraction angle, and β is the peak width at the half-maximum intensity in radian. Mean crystallite sizes have been estimated to be 10 and 33 nm for CdSe crystals synthesized at X values of 0 and 0.8, respectively. These results suggest that the nucleation and growth rates of CdSe tetrapods at an X value of 0.8 are quite different from the respective ones of CdSe nanosphere at an X value of 0 (see below). The mean crystallite size (D) is known to be related to two parameters by $<D> = 1.023\sqrt[3]{G/N}$, where G and N represent growth and nucleation rates, respectively.[28]

To understand the formation mechanism of tetrapods further, we have synthesized CdSe crystals with variation of the X value from 0 to 1. Figure 2-4 and Table 1 show that the morphology of wurtzite CdSe crystals has been evolved steadily from spheres at X = 0 to decorated tetrapods at X = 0.8 although CdSe crystals were not produced at X = 1 in ethylene glycol. It

has been found that the wurtzite CdSe tetrapods can be produced when the X value reaches a critical value between 0.67 and 0.8. Figure 2-4 and Table 1 also show that the average size of CdSe crystals increases continuously with the increment of the X value. Furthermore, HRXRD patterns have revealed that the average crystallite size of CdSe crystals increases gradually as well with the increase of the X value. Thus, Figure 2-4 as well as Table 2-1 have indicated that we can control both the morphology and the average size of CdSe crystals indeed by adjusting the X value, the mole fraction of $CdCl_2$ out of two cadmium precursors $CdCl_2$ and CdO.

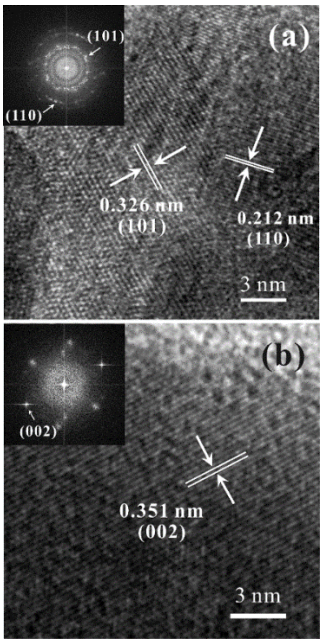

Figure 2-2. HRTEM images of hexagonal wurtzite CdSe crystals grown at X values of 0 (a) and 0.8 (b) in ethylene glycol for 10 min. Insets show the FFT patterns of the selected areas.

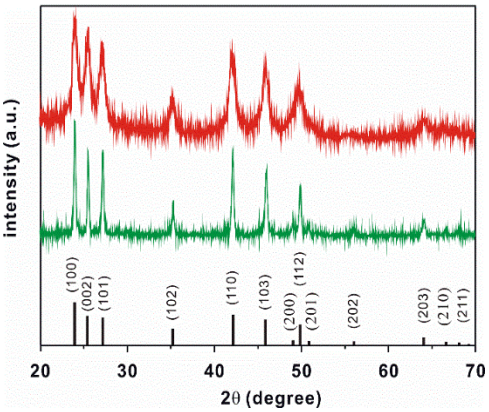

Figure 2-3. HRXRD patterns of CdSe crystals produced at X values of 0 (red) and 0.8 (green) in ethylene glycol and the reference wurtzite CdSe (black).

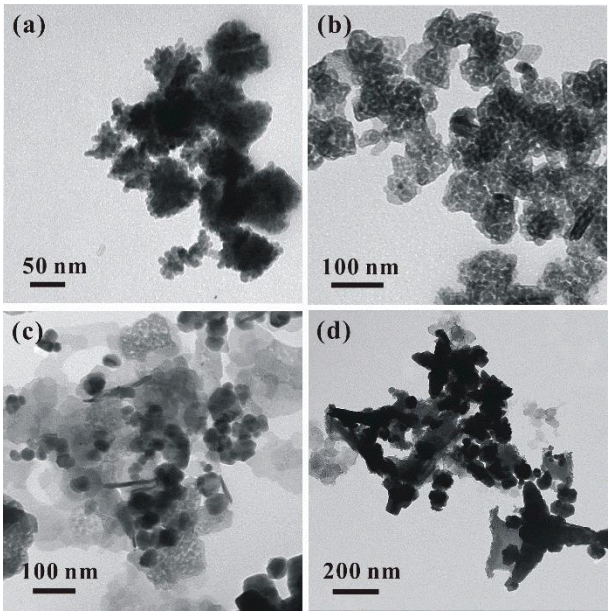

Figure 2-4. TEM images of CdSe crystals grown for 10 min at X values of 0.2 (a), 0.33 (b), 0.50 (c), and 0.67 (d) in ethylene glycol.

The XPS spectra of as-prepared CdSe crystals in Figure 2-5 can provide further significant information on the surface conditions of the products. Binding energies obtained in the XPS analysis have been calibrated by referencing the C 1s signal at 284.6 eV. The doublet Cd peaks of $3d_{5/2}$ and $3d_{3/2}$ have been observed at 404.8 and 411.5 eV, respectively, for CdSe nanospheres grown at X=0, and at 405.1 and 411.8 eV, respectively, for CdSe tetrapods grown at X = 0.8 while the unresolved doublet Se peaks of $3d_{5/2,3/2}$ have been observed at 53.8 eV with X = 0 and 54.1 eV with X = 0.8. Although, all the observed binding energies of Cd and Se are ranged within the literature values,[29-31] the XPS peak positions of CdSe tetrapods grown with X = 0.8 are shifted to the higher energy by 0.3 eV compared the respective ones of CdSe nanospheres grown with X = 0. We attribute this to the possible presence of chlorine, which has higher electronegativity than selenium, in replacement of selenium when the mole fraction of $CdCl_2$ for Cd precursors was 0.8. The quantitative analysis of EDX spectra (Figure 2-5) has shown that the molar ratios of selenium to cadmium are 0.97 for CdSe nanospheres and 0.91 for decorated CdSe tetrapods. The significantly smaller amount of selenium compared with cadmium (0.91) suggests that some selenide ions have been replaced by chloride ions for CdSe tetrapods grown at an X value of 0.8. Thus, these results indicate apparently that the surface conditions of as-prepared CdSe crystals have been also affected significantly by the employed precursors.

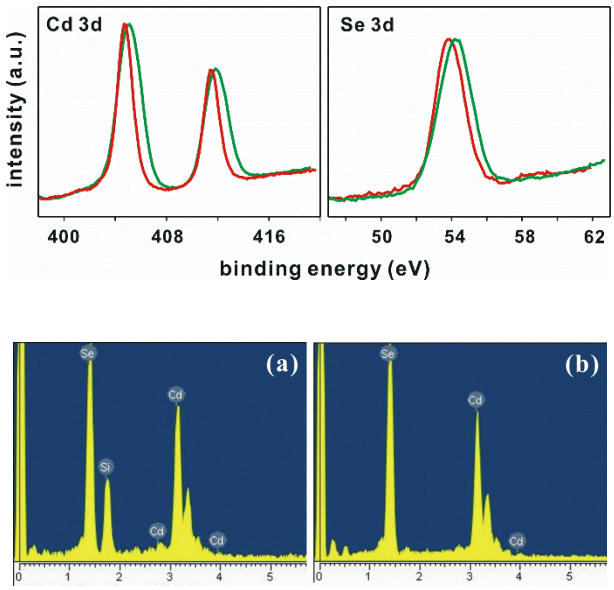

Figure 2-5 (top) Maximum-normalized XPS spectra of as-prepared CdSe crystals produced at X values of 0 (red) and 0.8 (green) in ethylene glycol. (bottom) EDX spectra of CdSe crystals grown in ethylene glycol for 10 min at X values of 0 (a) and 0.8 (b). The Si peak has originated from the silicon wafer substrate.

Because it is very difficult to estimate the band-gap energies (E_g) using the extinction spectra of Figure 2-6a, we have obtained the scattering-removed absorption spectra of Figure 2-6b by subtracting ($c_1/\lambda^4 + c_2$), where c_1, c_2 are arbitrary constants, from the extinction spectra of Fig. 6a. The relationship between absorption coefficients (α) near the absorption edge and E_g for direct interband transitions is known to obey $(\alpha h\nu)^2 = A(h\nu - E_g)$,[32-33] where A is a parameter and $h\nu$ is the photon energy. By extrapolating the linear portions of the $(\alpha h\nu)^2$ plots versus $h\nu$ to $\alpha = 0$ in the inset of Figure 2-6b, we have estimated the E_g of CdSe nanospheres and tetrapods to be 2.25

eV (551 nm) and 1.85 eV (670 nm), respectively. Both the average diameter of CdSe nanospheres (60 nm) and the average arm diameter of CdSe tetrapods (180 nm) are much larger than the Bohr exciton radius of CdSe (5.6 nm).[34] Thus, we attribute the red shift of tetrapods mainly to their intriguing nanocrystal shapes, in which four arms with a wurtzite structure branch from a central zinc blende core to exhibit behaviors of type-II composites, which have staggered band alignment.[25,35]

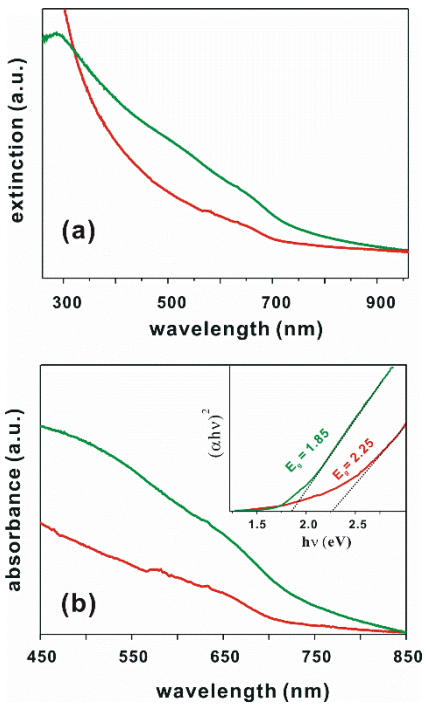

Figure 2-6. Extinction spectra (a) and scattering-removed absorption-edge spectra (b) of CdSe crystals produced at X values of 0 (red) and 0.8 (green) in ethylene glycol. The samples were suspended in ethanol at room temperature. The inset shows the plots of $(\alpha h\nu)^2$ vs hν to estimate E_g.

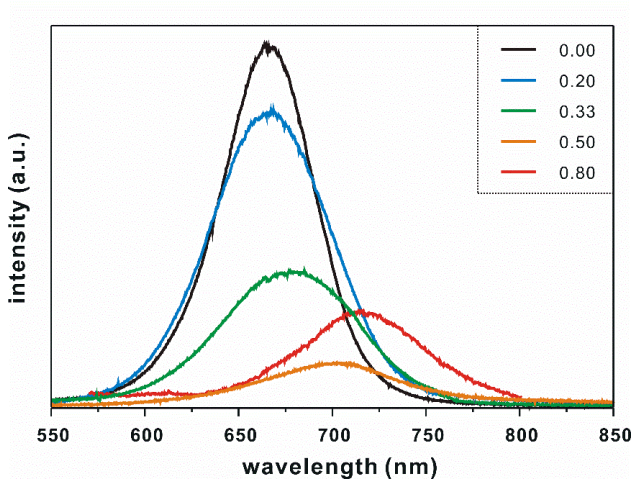

Figure 2-7. Photoluminescence spectra of CdSe crystals produced in ethylene glycol at various X values indicated inside. The samples were suspended in ethanol at room temperature and excited at 355 nm.

Figure 2-7 shows that the photoluminescence spectra of CdSe crystals shift to the red gradually as the X value increases from 0 to 0.8. The photoluminescence spectra of CdSe nanospheres at X = 0 and decorated CdSe tetrapods at X = 0.8 have the maxima at 663 and 715 nm, respectively. Table 1 has indicated that both the average size and the mean crystallite size of CdSe crystals grown in ethylene glycol increase gradually as the X value increases from 0 to 0.8. Thus, one might attribute the red shift of photoluminescence with the increment of the X values to the reduced quantum confinement resulting from the increase of the average crystallite size.[10] However, Figure 2-7 designates that the photoluminescence efficiency of CdSe crystals decreases roughly with the increase of the X value. Thus, we attribute the red shift of photoluminescence with the increase of the X value mainly to the increased character of CdSe tetrapods,

where four arms with a wurtzite structure and a core with a zinc blende structure have the staggered alignment of their bands to reveal type-II behaviors.[25,35]

To understand the solvent effect on the formation of CdSe crystals, we have employed both ethylene glycol (bp = 197 ºC; η = 16.1 cP at 25 ºC) and glycerol (bp = 290 ºC; η = 945 cP at 25 ºC) as the polyol solvent. As shown in Fig. 8a and Table 1, at X = 0, the morphology of CdSe crystals produced in glycerol was almost similar to that in ethylene glycol although the average size of CdSe nanospheres in glycerol was substantially smaller than that in ethylene glycol. The size decrease might be attributed to the higher viscosity of glycerol.[36] At X=0.8, however, the morphology of CdSe crystals in glycerol was largely different from that in ethylene glycol (Table 2-1). Furthermore, Table 1 and Fig. 8b indicate that at X = 1, although any structures of CdSe crystals have not been produced at all in ethylene glycol, CdSe tetrapods have been fabricated well in glycerol.

Considering the dependence of CdSe structures on precursors and solvents, we propose possible growth mechanisms of our prepared CdSe crystals in terms of the LaMer theory.[1,9,14-15,37-38] According to the theory, the precursors decompose and chemically transform into active monomers which play crucial roles in nucleation and growth processes. And only if the concentration of monomers is above critical supersaturation, which is high enough to overcome the energy barrier for nucleation, the formation of stable nuclei can take place. After the nucleation process, the nuclei can

grow by incorporating additional monomers still present in the reaction medium. Figure 2-8c suggests that there are intrinsically different formation mechanisms of CdSe crystals depending on CdO and $CdCl_2$ as cadmium precursors. CdO, which has a poor solubility in polyol solvents, remains as itself in ethylene glycol, so that it is directly activated under microwave irradiation and transformed into monomers without any hindrance. Consequently, the concentration of the monomers rapidly reaches to critical supersaturation at a very short time, resulting in burst nucleation; highly monodispersed nanospheres could be obtained (Figure 2-1 and 2-8).[37,39] However, $CdCl_2$, which is soluble very well in polyol solvent molecules to form tetrahedral or octahedral complexes of cadmium ions.[40] The formation of cadmium-polyol complexes could modify the reactivity of the $CdCl_2$ precursor significantly to retard the formation of monomers. As a result, the monomers are unevenly produced and depleted during the reaction, and then the nucleation of CdSe proceeds over an extended period of time, leading to variation in growth rates.[9,38] Thus, kinetically controlled nucleation and growth processes could determine the shapes and sizes of CdSe crystals in a microwave-assisted polyol process.

In ethylene glycol which has a lower boiling point, cadmium-polyol complexes cannot transform efficiently into active monomers under microwave irradiation due to the insufficient thermal energy. So the concentration increment of monomers from the $CdCl_2$ precursor is limited. For this reason, when at X = 1 ($CdCl_2$ only for cadmium precursors) in

ethylene glycol, the nucleation of CdSe did not occur to produce any CdSe crystals in a short reaction time of 10 min. This result also indicates that the CdO precursor is indispensible for the formation of CdSe nuclei in ethylene glycol. When the X value was small (the mole fraction of CdO was high), most of precursors were consumed at the nucleation process and a low flux of monomers was supplied during the growth process, resulting in the isotropic growth of CdSe nuclei to produce CdSe nanospheres. When the X value was high (the mole fraction of $CdCl_2$ was high), however, only a small portion of the precursors was consumed at the nucleation process and a high flux of monomer was extensively supplied during the growth process, facilitating the anisotropic growth of CdSe nuclei and also leading to the size increase of CdSe crystals.[9,38] This also explains reasonably why decorated tetrapods and decorated spheres of CdSe crystals were grown at X = 0.8 in ethylene glycol and glycerol, respectively; $CdCl_2$ can also participate in the nucleation of CdSe only in the solvent of glycerol. Consequently, we can suggest that the shapes and sizes of CdSe crystals can be controlled in a microwave-assisted polyol process by adjusting precursors and solvents, which determine the nucleation and growth kinetics of CdSe.

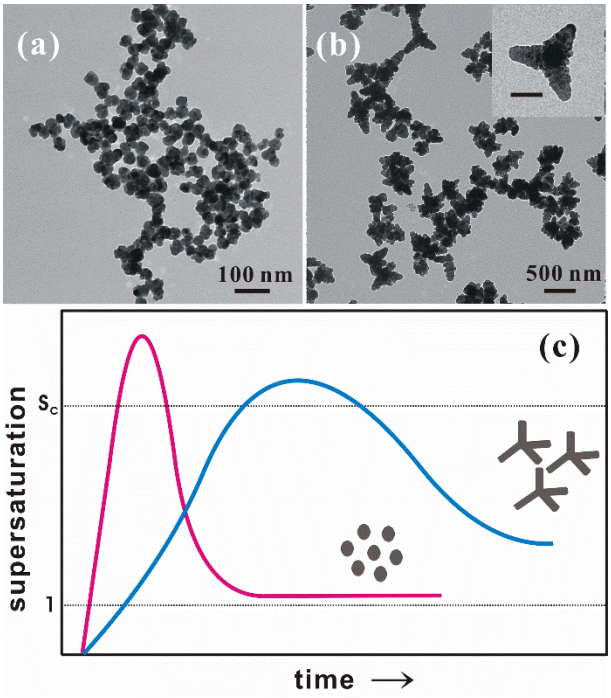

Figure 2-8. TEM images of CdSe crystals grown in glycerol for 10 min at X values of 0 (a) and 1.0 (b). The scale bar of the inset indicates 300 nm. LaMer plots (c) for the formation of CdSe crystals grown at X values of 0 (red) and 1.0 (blue) in glycerol. Sc indicates critical supersaturation.

2. 5. Conclusion

We have illustrated a facile and novel method for controlling the shapes and sizes of wurtzite CdSe crystals. As a demonstration, the morphology of CdSe crystals has been controlled by adjusting the relative amounts of two cadmium precursors $CdCl_2$ and CdO in a polyol solvent of ethylene glycol or glycerol; spheres, pebbles, sheets, and tetrapods of CdSe wurtzite structures with their sizes ranged from nanometers to sub-micrometers have

been prepared facilely under microwave irradiation. The optical properties of CdSe crystals have been found to depend on shapes and sizes. Based on our results, we have proposed the formation mechanisms of CdSe crystals in terms of the LaMer theory. The key factors of the shape and size variation of CdSe crystals are nucleation and growth processes, whose rates are determined by precursors as well as solvents. We consider that our results would contribute to the development of a new synthetic strategy in microwave chemistry for fabricating semiconductor nano-structures, which still remains to be veiled due to the lack of well-established theories and mechanistic studies.

2. 7. References

(1) H. Goesmann, C. Feldmann, *Angew*. *Chem*. *Int*. *Ed*., 2010, **49**, 1362-1395.

(2) D. V. Talapin, J.-S. Lee, M. V. Kovalenko, E. V. Shevchenko, *Chem.Rev*., 2010, **110**, 389-458.

(3) M. R. Kim, D.-J. Jang, *Chem. Commun*., 2008, 5218–5220

(4) M. S. Kang, A. Sahu, D. J Norris, C. D. Frisbie, *Nano lett*., 2010, **10**, 3727-3732.

(5) Q. Zhao, P. A. Graf, W. B. Jones, A. Franceschetti, J. Li, L.-W. Wang, K. Kim, *Nano lett*., 2007, **7**, 3274-3280.

(6) T. Zhai, X. Fang, Y. Bando, Q. Liao, X. Xu, H. Zeng, Y. Ma, J. Yao, D. Golberg, *ACS Nano*, 2009, **3**, 949-959.

(7) M. R. Kim, S.-Y. Park, D.-J. Jang, *Adv*. *Funct*. *Mater*., 2009, **19**, 3910-3916.

(8) M. R. Kim, S.-Y. Park, D.-J. Jang, *J. Phys. Chem*. *C*, 2010, **114**, 6452–6457.

(9) Y.-W. Jun, J.-S. Choi, J. Cheon, *Angew. Chem. Int. Ed*., 2006, **45**, 3414-3439.

(10) Z. Wang, Q. Lu, X. Fang, X. Tian, L. Zhang, *Adv*. *Funct*. *Mater*., 2006, **16**, 661-666.

(11) L. Liu, Z. Zhuang, T. Xie, Y.-G. Wang, J. Li, Q. Peng, Y. Li, *J*. *Am*. *Chem*. *Soc*., 2009, **131**, 16423–16429.

(12) J. S. Jie, W. J. Zhang, Y. Jiang, S. T. Lee, *Appl*. *Phys*. *Lett*., 2006, **89**, 133118.

(13) S. Dayal, M. O. Reese, A. J. Ferguson, D. S. Ginley, G. Rumbles, N. Kopidakis, *Adv*. *Funct*. *Mater*., 2010, **20**, 2629-2635.

(14) I. Bilecka, M. Niederberger, *Nanoscale*, 2010, **2**, 1358-1374.

(15) M. Baghbanzadeh, L. Carbone, P. D. Cozzoli, C.O. Kappe, *Angew*. *Chem*. *Int*. *Ed*., 2011, **50**, 11312-11359.

(16) M. N. Nadagouda, T. F. Speth, R. S. Varma, *Acc. Chem. Res.*, 2011, **44**, 469-478.

(17) N. N. Mallikarjuna, R. S. Varma, *Cryst. Growth Des.*, 2007, **7**, 686-690.

(18) Z.-P. Qiao, Y. Zhang, L.-T. Zhou, Q. Xire, *Cryst. Growth Des.*, 2007, **7**, 2394-2396.

(19) N. N. Mallikarjuna, R. S. Varma, *Cryst. Growth Des.*, 2008, **8**, 291-295.

(20) E. Rauwel, A. Galeckas, P. Rauwel, M. F. Sunding, H. Fjellvag, *J. Phys. Chem. C*, 2011, **115**, 25227-25233.

(21) V. Singh, A. Karakoti, A. Kumar, A. Saha, S. Basu, S. Seal, *J. Am. Ceram. Soc.*, 2010, **93**, 3700-3708.

(22) A. Mohanty, N. Garg, R. Jin, *Angew. Chem. Int. Ed.*, 2010, **49**, 1-6.

(23) O. Palchik, R. Kerner, A. Gedanken, A. M. Weiss, M. A. Slifkin, V. Palchik, *J. Mater. Chem.*, 2001, **11**, 874-878.

(24) L. Manna, D. J. Milliron, A. Meisel, E. C. Scher, A. P. Alivisatos, *Nat. Mater.*, 2003, **2**, 382−385.

(25) D. Tari, M. D. Giorgi, F. D. Sala, L. Carbone, R. Krahne, L. Manna, R. Cingolani, *Appl. Phys. Lett.*, 2005, **87**, 224101.

(26) Z. Y. Wang, X. S. Fang, Q. F. Lu, C. H. Ye, L. D. Zhang, *Appl. Phys. Lett.*, 2006, **88**, 083102.

(27) M. Zhang, T. Zhai, X. Wang, Y. Ma, Y. Yao, *Cryst. Growth Des.*, 2010, **10**, 1201-1206.

(28) J. M. Byrne, N. D. Telling V. S. Coker, R. A. D. Pattrick, G. van der Laan, E. Arenholz, F. Tuna, J. R. Lloyd, *Nanotechnology*, 2011, **22**, 455709.

(29) N. S. Lam, K. W. Wong, Q. Li, Z. Zheng, W. M. Lau, *Nanotechnology*, 2007, **18**, 415607.

(30) R. E. Galian, M. Guardia, J. Perez-Prieto, *Langmuir*, 2011, **27**, 1942-1945.

(31) J. S. Owen, J. Park, P.-E. Trudeau, A. P. Alivisatos, *J. Am. Chem. Soc.*, 2008, **130**, 12279-12281.

(32) X. Fang, Y. Bando, G. Shen, C. Ye, U. K. Gautam, P. M. F. Costa, C. Zhi, C. Tang, D. Golberg, *Adv. Mater.*, 2007, **19**, 2593-2596.

(33) S. Monticone, R. Tufeu, A.V. Kanaev, *J. Phys. Chem. B*, 1998, **101**, 2854-2862.

(34) R. W. Meulenberg, J. R. Lee, A. Wolcott, J. Z. Zhang, L. J. Terminello, T. van Buuren, *ACS Nano*, 2009, **3**, 325-330.

(35) P. Reiss, M. Protiere, L. Li, *Small*, 2009, **5**, 154-168.

(36) K. H. Park, S. H. Im, O. O. Park, *Nanotechnology*, 2011, **22**, 045602.

(37) J. Park, J. Joo, S. G. Kwon, Y. Jang, T. Hyeon, *Angew. Chem. Int. Ed.* 2007, **46**, 4630-4660.

(38) A. R. Tao, S. Habas, P. Yang, *Small*, 2008, **4**, 310-325.

(39) K. Yu, *Adv. Mater.*, 2012, **24**, 1123-1132.

(40) D. Knetsch, W. L. Groeneveld, *Inorg. Chim. Acta.*, 1973, 7, 81-87.

Chapter 3. Dislocation-Driven Growth of Porous CdSe Nanorods from CdSe·(ethylenediamine)$_{0.5}$ Nanorods[†]

[†]This is reproduced from Hyung-Bae Kim and Du-Jeon Jang, *Nanoscale*, 2016, **8**, 403 - 410. © 2016 Royal Society of Chemistry.

3. 1. Abstract

Porous CdSe nanorods having a novel flute-like morphology have been prepared facilely via the hydrothermal treatment of $CdSe \cdot (en)_{0.5}$ (en = ethylenediamine) nanorods as sacrificial templates. During the hydrothermal process, various crystalline imperfections such as stacking faults and twinning planes appear due to lattice mismatches between orthorhombic $CdSe \cdot (en)_{0.5}$ and hexagonal wurtzite porous CdSe nanorods and subsequently disappear to release mismatched strains. In the self-healing process of defects, due to the imbalance of in-and-out atomic diffusion, point defects of atomic vacancies are heavily generated in CdSe nanorods to produce volume defects of voids eventually. The photoluminescence of CdSe nanorods shifts to the red region and decreases in intensity with the increase of the hydrolysis time as surface states and selenium vacancies increase. The mean lifetime of photoluminescence increases with the increase of the hydrothermal-treatment time as the fractional amplitude of the surface-state-related component increases.

3. 2. Introduction

The morphology control of nanomaterials has been considered to be a crucial issue in nanotechnology research due to their structure-dependent fundamental properties.[1–7] In particular, the fabrication of one dimensional (1D) nanostructures such as nanorods, nanowires, nanobelts and nanotubes has attracted considerable scientific attention owing to their novel properties in optoelectronic and electrochemical applications.[8–11] Solution-phase synthetic strategies have been widely used to prepare controlled 1D semiconductor nanostructures.[12] Among them, solvothermal solvent-coordination molecular template (SCMT) methods have been widely used to produce novel inorganic–organic nanostructures.[12–15] Novel inorganic–organic hybrid nanomaterials of MX·(Y)n composites (M = Cd, Zn, Mn; X = S, Se, Te; Y = amine derivatives; n = 0.5 or 1) have been fabricated easily via SCMT routes.[13,14,16–18] The $MX{\cdot}(Y)_n$ nanomaterials have strong quantum-confinement effects and high carrier mobility owing to their layered structures. Furthermore, they have been considered as useful precursors for the production of MX semiconductor nanostructures via hydrothermal treatment.[17–19] Typically, the intrinsic morphologies of MX·(Y)n nanostructures are preserved even after conversion into MX, but their structures are sometimes turned into porous structures due to the removal of organic moieties. Consequently, with the assistance of $MX{\cdot}(Y)_n$ precursors, MX semiconductor nanostructures can have novel porous morphologies.[13,19]

When crystal lattices are subjected to stress, crystal defects are often produced as a means of the energy minimization of high surface tensions. Generally, the crystal defects are classified by their dimension as point defects, line defects, planar defects, and volume defects, and these crystal imperfections can significantly affect the properties of semiconductor nanostructures.[20–23] Crystal defects do not always have negative effects on the quality of nanocrystals but rather are exploitable in realizing interesting concepts such as the construction of multiquantum wells,[24] the synthesis of branched nanostructures,[25] and the creation of internal voids.[23,26–28] 1D nanostructures are prone to having planar defects such as stacking faults and twinning planes during the crystal growth.[21–23] Particularly, stacking faults, which are generated between line defects, are an important class of planar defects commonly observed in closely packed crystal structures. They have been often produced at every boundary of two different crystal structures such as hexagonal wurtzite and cubic zincblende. Thus, stacking faults are used as internal standards for detecting orientations and phase transitions in nanostructures.[21,22] Consequently, understanding the formation mechanisms of stacking faults is crucial in controlling nanostructures better via defect engineering.

CdSe, which has a narrow band gap of 1.74 eV, is one of the most attractive II–VI semiconductor materials with wide potential applications in fabricating nanoscale electronic, photonic, electromechanical, and biomedical devices.[3-6,29,30] CdSe is used as an ideal system to verify the kinetic model of particle growth in solution phases, which further directs the synthesis of additional

analogue II–VI semiconductor materials such as ZnS, ZnSe, CdS, and CdTe. Therefore, it is meaningful to develop new synthetic approaches to control CdSe nanostructures. Although there are numerous reports about the synthesis of 1D CdSe nanostructures, the preparation of porous 1D CdSe nanostructures has been rarely reported in spite of the importance of porous materials.[31-33]

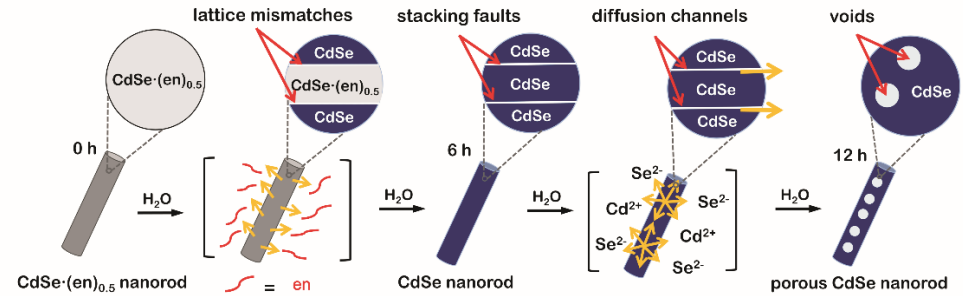

Figure 3-1 Schematic illustration for the formation of porous CdSe nanorods *via* the hydrothermal treatment of CdSe·$(en)_{0.5}$ nanorods. The formation mechanism is depicted as a function of the hydrothermal-treatment time.

Herein, we demonstrate a unique strategy to produce porous CdSe nanorods with the assistance of crystal defects. CdSe·$(ethylenediamine)_{0.5}$ nanorods have been used as sacrificial templates to produce porous CdSe nanorods. During the hydrothermal transformation of CdSe·$(ethylenediamine)_{0.5}$ nanorods into porous CdSe nanorods, various crystalline imperfections such as stacking faults and twinning planes have been found to appear and subsequently disappear to release mismatched strains. On the basis of our observation of the generation and disappearance of various defects, we suggest a dislocation-driven formation mechanism of porous CdSe nanorods (Figure 3-1). Furthermore, we

have also observed the defect-related photophysical properties of as-prepared porous CdSe nanorods. Thus, we believe that this work provides a novel strategy for the rational design of defectengineered nanostructures.

3. 3. Experimental Details

Materials. The analytical grade chemicals of $CdCl_2$(s), Se(s), ethylenediamine(l, en), and hydrazine monohydrate(l) were purchased from Sigma-Aldrich. Ultrapure deionized water (>17 MΩ cm) from a Millipore Milli-Q system was used throughout the experiments.

Synthesis of $CdSe \cdot (en)_{0.5}$ nanorods. 1.0 mmol of $CdCl_2$ was put into 30 mL of en and the mixture was sonicated in an ultrasonic bath for 30 min. Then, 0.50 mmol of Se and 0.25 mmol of hydrazine monohydrate were added into the above mixture and stirred vigorously for 1 h. The mixture solution was loaded into a Teflon-lined stainless-steel autoclave of 50 mL capacity, placed in a preheated oven at 200 ℃ for 12 h, and cooled to room temperature naturally. A dark brown precipitate produced in the reaction mixture was washed twice with deionized water and ethanol to remove residual impurities, and the product was dried in a vacuum at 50 ℃ for 6 h. Note that $CdSe \cdot (en)_{0.5}$ nanorods were prepared with a [$CdCl_2$]-to-[Se] ratio of 2.0 and that $CdSe \cdot (en)_{0.5}$ nanostructures prepared with a [$CdCl_2$]-to-[Se] ratio of 1.0 do not have rod-like shapes.

Synthesis of porous CdSe nanorods. Porous CdSe nanorods were fabricated by treating the precursors of $CdSe{\cdot}(en)_{0.5}$ nanorods hydrothermally at 150 ℃ in a Teflon-lined stainless-steel autoclave for 12 h. The product in the reaction mixture was washed twice with deionized water and ethanol to remove residual impurities and dried in a vacuum at 50 ℃ for 12 h. Nanostructures obtained by the hydrothermal treatment of $CdSe{\cdot}(en)_{0.5}$ nanorods for 0, 3, 6, 9 , and 12 h will be designated as CE00, CE03, CE06, CE09, and CE12, respectively.

Characterization. While transmission electron microscope (TEM) images were measured with a Zeiss LIBRA 120 microscope, fast Fourier transform (FFT) patterns and high-resolution transmission electron microscope (HRTEM) images were measured with a JEOL JEM-3010 microscope. High-resolution X-ray diffraction (HRXRD) patterns were recorded with a Bruker D8 DISCOVER diffractometer using Cu K_α radiation (λ = 0.154178 nm). X-ray photoelectron spectroscopy (XPS) spectra were collected using a Thermo Scientific Sigma Probe ESCA spectrometer with an Al K_α X-ray source, and their measured binding energies were calibrated with the C 1s peak at 284.6 eV of contaminated carbon. Energy-dispersive X-ray (EDX) spectra were collected by using a JEOL JSM-6700F microscope. High-angle annular dark-field (HAADF) images and line-scanned EDX elemental profiles were obtained by using an Oxford INCA scanning transmission electron microscope (STEM) installed in a JEOL JEM-3000F microscope. Photoluminescence spectra were detected using a Princeton Instruments ICCD576G CCD attached to a 0.5 m Acton Research SpectraPro-500 spectrometer with excitation of 355 nm pulses

from a Q-switched Quantel Brilliant Nd:YAG laser of 6 ns. To obtain time-resolved fluorescence kinetic profiles, a mode-locked Quantel Pizzicato Nd:YAG laser with the pulse duration of 25 ps was employed for excitation, and a Hamamatsu C2830 streak camera of 10 ps attached to a Princeton Instruments RTE128H CCD detector was used for detection. Samples were excited with the third-harmonic pulses (355 nm) of the laser. Emission wavelengths were selected by combining band-pass and cut-off filters. Fluorescence kinetic constants were extracted by fitting kinetic profiles to computer-simulated exponential curves convoluted with instrument response functions. All the measurements were carried out at room temperature.

3. 4. Results and Discussion

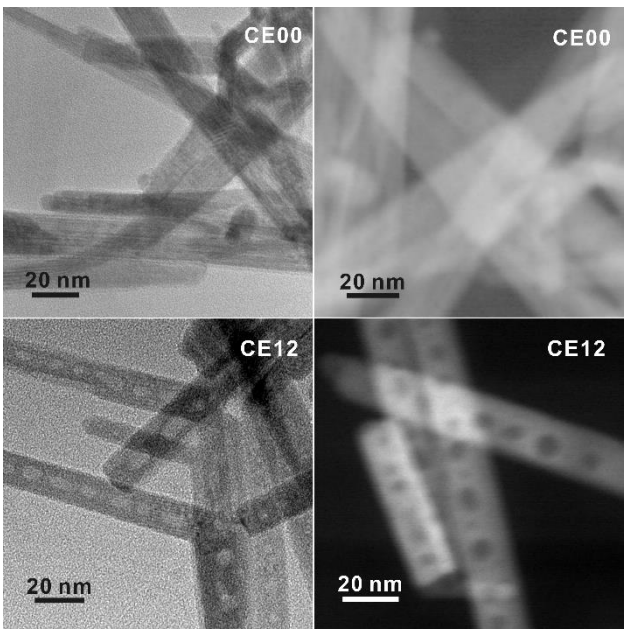

Figure 3-2 TEM (left) and HAADF-STEM images (right) of indicated nanostructures

Orthorhombic $CdSe \cdot (en)_{0.5}$ crystals with an inorganic–organic layered structure have been known to transform into hexagonal wurtzite CdSe crystals via releasing the en moiety intercalated at CdSe interlayer spaces during the hydrothermal treatment at >120 ℃.[13,14] Owing to the layered structure, the transformation process can proceed through a layer-by-layer fashion (see below). Considering that the intrinsic exterior morphologies of $CdSe \cdot (en)_{0.5}$ nanostructures are preserved usually after transformation into CdSe, and that rod-like 1D nanostructures are prone to having planar defects,21 we should optimize the morphology of $CdSe \cdot (en)_{0.5}$ precursors to drive the defect-driven growth of CdSe nanorods. Note that $CdSe \cdot (en)_{0.5}$ nanorods have been prepared with a [CdCl2]-to-[Se] ratio of 2.0 and that $CdSe \cdot (en)_{0.5}$ nanostructures prepared with a [CdCl2]-to-[Se] ratio of 1.0 do not have rod-like shapes.

The HAADF-STEM and TEM images of Figure 3-2 show the morphologies of $CdSe \cdot (en)_{0.5}$ nanorods and porous CdSe nanorods prepared by the hydrothermal treatment of $CdSe \cdot (en)_{0.5}$ nanorods for 12 h. $CdSe \cdot (en)_{0.5}$ nanorods have an average length of 210 nm and an average diameter of 20 nm while hydrothermally produced porous CdSe nanorods almost retain the intrinsic rod-like shapes as well as the average length and diameter of the precursors. However, CE12 CdSe nanorods have multiple voids ranging from 8 to 12 nm, which can be confirmed by the presences of contrast-inverted regions at the centers of the nanorods in both HAADF-STEM and TEM images. Figure S2 in the SI indicates that nanostructures produced by the hydrothermal

treatment of $CdSe \cdot (en)_{0.5}$ for 6 or 9 h do not have nanopores. Thus, it can be concluded that nanocavities in CdSe nanorods were generated during the hydrothermal treatment time of >9 h.

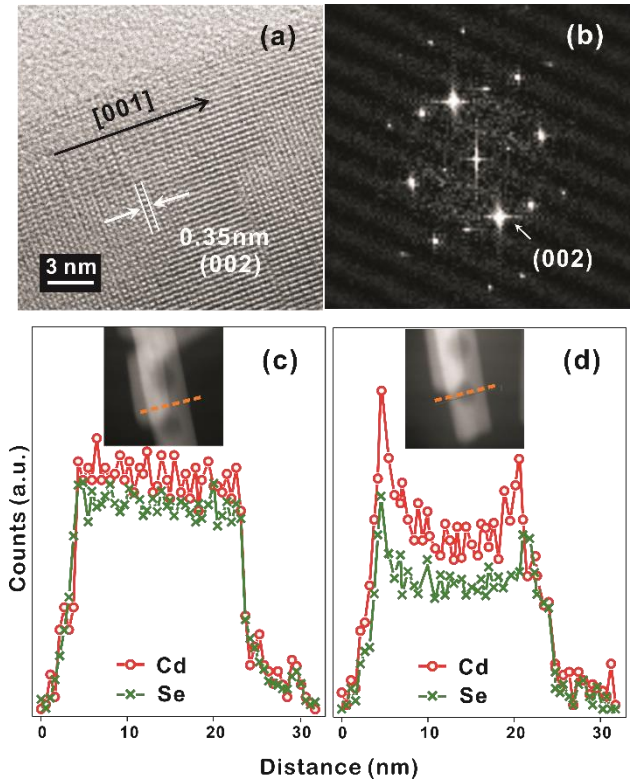

Figure 3-3 HRTEM image (a), FFT pattern (b), and STEM-EDX elemental profiles (c,d), scanned along the lines in the HAADF images of the insets, of a CE12 porous nanorod.

The discernible lattice-fringe image of Figure 3-3a and the clear diffraction spots of Figure 3b indicate that a porous CdSe nanorod possesses a well-defined single crystalline structure. The interplanar distance of 0.35 nm observed from the lattice fringes of Figure 3-3a accords with the

theoretical spacing of 0.352 nm between the (002) planes of wurtzite CdSe (JCPDS No. 08-0459). The d-spacing of 0.34 nm calculated from the most brightest diffraction spot in the FFT pattern of Figure 3-3b also agrees reasonably with the spacing of the (002) planes, implying that the as-synthesized porous CdSe nanorod has a preferred [001] orientation.[31,32] To verify whether the as-synthesized porous CdSe nanorod indeed has nanocavities, its line-scanned EDX elemental profiles have also been examined; although a bright region in the HAADF-STEM image of Figure 3-3c has a flat elemental profile for both Cd and Se, a dark circles region in the HADDF-STEM image of Figure 3-4d has a parabolic-shaped elemental profile, which is a common feature of hollow structures, for both Cd and Se.[4,23] Interestingly, the atomic ratio of [Se]-to-[Cd] calculated from the integrated elemental profiles of Figure 3-3c is 0.92 whereas the ratio calculated from Figure 3-3d is 0.76. This indicates that while selenium vacancies are rich in a porous CdSe nanorod, they are three times richer in void regions than in filled regions. Considering this observation, we suggest that Se anions have diffused out faster than Cd cations during the hydrothermal process of $CdSe \cdot (en)_{0.5}$ nanorods and that the diffusion of Se anions is particularly rapid near crystal defects (see below).

The HRXRD patterns of Figure 3-4 show the structural evolution of $CdSe \cdot (en)_{0.5}$ nanorods with the increase of the hydrothermal-treatment time. The diffraction patterns of nanostructures prepared by the hydrothermal treatment of $CdSe \cdot (en)_{0.5}$ nanorods for 0 and 3 h can be correlated well with the

reported pattern of the orthorhombic $CdSe \cdot (en)_{0.5}$.[10,11] However, the diffraction patterns of CE06 and CE12 nanorods produced by the hydrothermal treatment of $CdSe \cdot (en)_{0.5}$ nanorods for 6 and 12 h, respectively, agree well with the standard pattern of the hexagonal wurtzite CdSe (JCPDS No. 08-0459). It means that the complete transformation of orthorhombic $CdSe \cdot (en)_{0.5}$ nanostructures into wurtzite CdSe nanostructures *via* hydrothermal treatment at 150 ℃ takes longer than 3 h. The characteristic diffraction peaks of CE06 and CE12 CdSe nanorods at the 2θ value of 25.2°, which arise from the (002) planes of the wurtzite CdSe, are particularly strong in comparison of diffraction peaks arising from any other planes. This indicates that our CE06 and CE12 CdSe nanorods have a preferred [001] orientation, as already described with the HRTEM image of Figure 3a and the FFT pattern of Figure 3b. Using the Scherrer equation[14] and assuming that peak broadening arises entirely from size effects, we have calculated average crystallite sizes by using the peaks at 2θ of ~42º. The average crystallite sizes of CE00, CE03, CE06, and CE12 nanostructures have been calculated as 27.5, 24.5, 10.2, and 9.8 nm, respectively, indicating that the average crystallite size of $CdSe \cdot (en)_{0.5}$ nanorods has decreased with hydrothermal treatment. In particular, during the hydrolysis time between 3 and 6 h, crystallite sizes have reduced extensively. This also supports that the transformation of orthorhombic $CdSe \cdot (en)_{0.5}$ nanorods into wurtzite CdSe nanorods has taken place essentially during the hydrothermal treatment time between 3 and 6 h.

HRXRD profiles can provide significant information about the structural defects because internal stress, caused by misfit at grain boundaries, can change lattice parameters such as lattice constants and interplanar spacings.[36,37] Thus, diffraction patterns from distorted crystallites are different in the location and broadening of a peak. In the case of internal tensile stress resulting from planar defects, HRXRD peaks are known to shift to a higher angle than the standard diffraction pattern.36 Fig. 4 shows that the XRD peaks of CE06 and CE12 have small shifts to higher angles, indicating that there are structural defects in both CdSe nanostructures. It is noteworthy that the peak shifts of CE12 are smaller than those of CE06, suggesting that the internal stress of planar defects relaxes gradually during the late stage of hydrothermal treatment (see below).

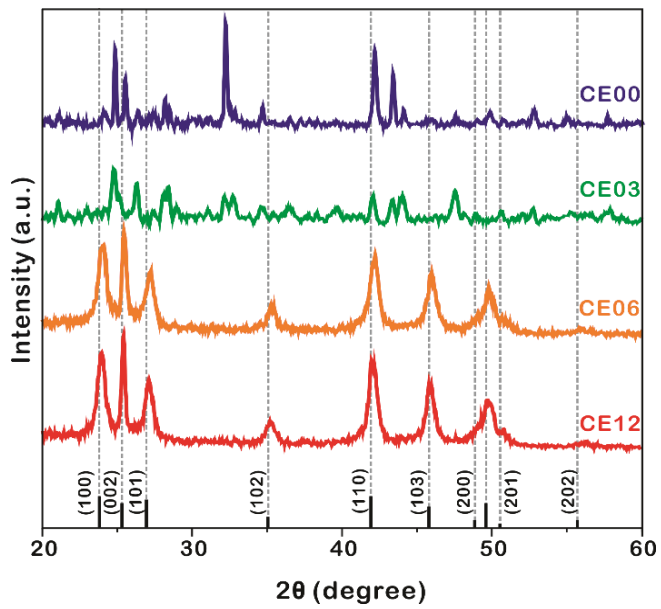

Figure 3-4 HRXRD patterns of indicated nanostructures. The standard diffraction pattern of CdSe (JCPDS No. 08-0459) is also shown in the bottom.

The HRTEM images of Figure 3-5 display the lattice evolution of $CdSe \cdot (en)_{0.5}$ nanorods with the increase of the hydrothermal-treatment time. In the early stage of the hydrothermal-treatment time of 3 h, highly defective regions, which are generally called as stacking faults, have been observed throughout the crystal lattice of a CE03 nanorod. These stacking faults are considered to arise from lattice mismatches between orthorhombic $CdSe \cdot (en)_{0.5}$ structures and hexagonal wurtzite CdSe structures. The observed stacking faults are parallel to each other and perpendicular to the growth direction of nanostructures. Thus, we suggest that the chemical transformation of orthorhombic $CdSe \cdot (en)_{0.5}$ nanorods into hexagonal wurtzite CdSe nanorods has progressed in a layer-by-layer fashion. Stacking faults still remain in the crystal lattices of CE06 and CE09 nanostructures even after orthorhombic $CdSe \cdot (en)_{0.5}$ nanorods have been converted completely into hexagonal wurtzite CdSe nanorods. The remaining stacking faults have functioned as twinning planes around which CdSe lattice segments have aligned along the [001] direction in a zigzag manner. As the hydrothermal-treatment time increases, the observed number of plane defects decreases gradually, indicating that the internal stress of planar defects relaxes gradually during the late stage of hydrothermal treatment. Owing to the self-healing process of planar defects, most of the stacking faults have disappeared eventually to produce highly crystalline CE12 CdSe nanorods. When the crystal lattice is distorted, atomic diffusion can occur to release the excess elastic energy of the lattice.[25,33]

Twinning boundaries have been considered to become another fast diffusion path as a 'pipe diffusion' concept,[34] and outward atomic diffusion can be particularly triggered near the twining plane sites during the self-healing process of planar defects. Due to the imbalance of atomic in-and-out diffusion, point defects can be severely generated near twinning boundaries, finally forming volume defects of voids in a CE12 CdSe nanorod. Therefore, we assert that the emergence of internal voids in a porous CdSe nanorod has been closely correlated with the disappearance of planar defects. However, the evidence of axial dislocation has not been observed in our nanorods, suggesting that our CdSe nanorods have grown up unlikely *via* a screw-dislocation mechanism.[19,20]

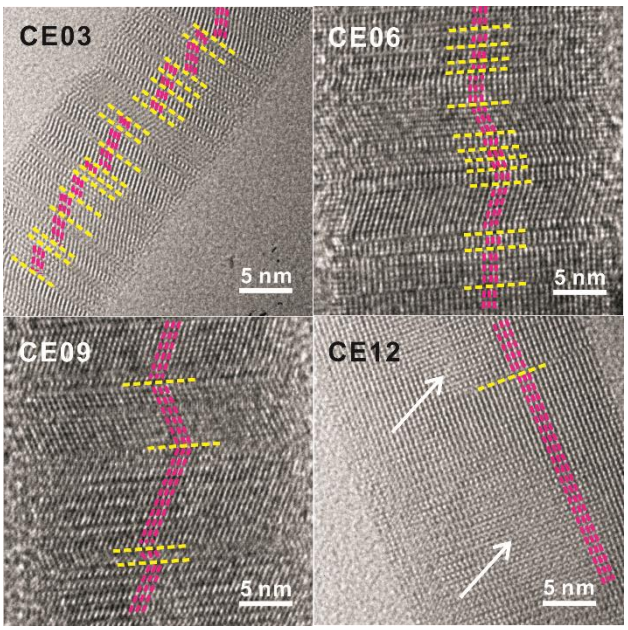

Figure 3-5 HRTEM images of indicated nanostructures. Yellow lines mark planar defects while pink lines and white arrows indicate lattice alignments and pore regions, respectively.

To understand the formation mechanisms of porous CdSe nanorods in detail, we have measured the XPS spectra of Cd 3d and Se 3d with the increase of the hydrothermal-treatment time (Figure 3-6). The XPS peak positions of Cd 3d have shifted significantly to the low binding energy with the hydrolysis time whereas the XPS peak positions of Se 3d have shifted hardly (Table 3-1). As CE00 $CdSe \cdot (en)_{0.5}$ nanorods have been transformed into CE06 CdSe nanorods, the binding energies of Cd 3d have been decreased significantly because the electronegativity of Se is smaller than that of N. The further down shift of Cd 3d binding energies during the hydrolysis time between 6 and 12 h has been attributed to the increased presence of Se vacancies because it is generally known that adjacent anion vacancies reduce the binding energy of metal ions.[35] Interestingly, Figure 6 and Table 1 show that the atomic ratio of [Se]-to-[Cd] for porous CdSe nanorods is substantially smaller than one. As already described with the EDX elemental profiles of Figure 3-3, selenium vacancies are rich particularly in CE12 porous CdSe nanorods, suggesting that Se anions have diffused out faster than Cd cations during the hydrothermal process of $CdSe \cdot (en)_{0.5}$ nanorods and that the diffusion of Se anions is rapid near crystal defects. We suggest that generated selenium vacancy sites have been filled with trapped electrons, oxide ions, or hydroxide ions to balance the overall charge of nanostructures.[36] Summarizing the above presented results, we propose a dislocation-driven growth mechanism of porous CdSe nanorods from $CdSe \cdot (en)_{0.5}$ nanorods in Figure 3-1.

Table 3-1. Parameters of the XPS Spectra in Figure 3-6

sample	binding energy (eV)			atomic ratio[a]	
	Cd $3d_{5/2}$	Cd $3d_{3/2}$	Se 3d	Cd	Se
CE00	405.7	412.4	54.3	1.00	0.99
CE06	405.0	411.7	54.1	1.00	0.97
CE12	404.8	411.5	54.0	1.00	0.78

[a]Surface atomic ratios of Cd and Se are calculated from the XPS by using peak areas normalized on the basis of sensitivity factors.

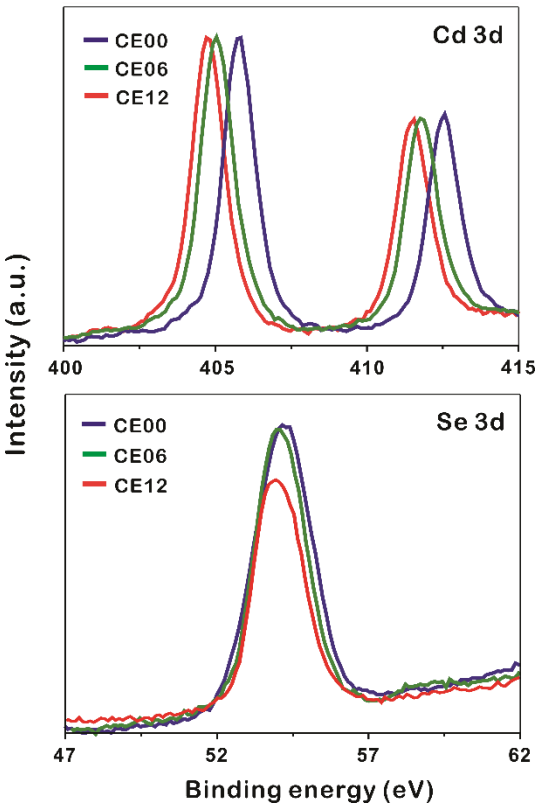

Figure 3-6 XPS spectra of indicated nanostructures.

Figure 7 shows that the photoluminescence of as-prepared nanostructures shifts to the red and decreases in intensity as the hydrothermal-treatment time increases. The photoluminescence of CE06 CdSe nanorods has shifted to the

red by 36 nm from that of CE00 $CdSe \cdot (en)_{0.5}$ nanorods at 635 nm as en molecules intercalated in CdSe layers have been removed.[14,15] Even after orthorhombic $CdSe \cdot (en)_{0.5}$ nanorods have been converted completely into hexagonal wurtzite CdSe nanorods, the photoluminescence of CE06 CdSe nanorods has shifted further to the red by 9 nm during the hydrothermal-treatment time between 6 and 12 h. Figure 4S and Table S1 in the SI indicate that the near-infrared shoulder band of photoluminescence at 784 nm, which has been attributed to arise from selenium vacancies and oxygen impurities,[35] increases by 4.8 times during the hydrothermal-treatment time between 6 and 12 h. This also supports the observation of Figure 6 and Table 1 that selenium vacancies are rich particularly in CE12 porous CdSe nanorods. The continuous decrease of photoluminescence intensity with the increase of the hydrolysis time is attributed to increased surface states, which block the recombination of electrons in the conduction band with holes in the valence band, as Figure 4 has shown that the average crystallite sizes of nanorods decrease gradually with the increase of the hydrothermal treatment time.

Figure 3-8 and Table 3-2 indicate the photoluminescence kinetic profiles of CE00 $CdSe \cdot (en)_{0.5}$ nanorods, CE06 CdSe nanorods, and CE12 porous CdSe nanorods look similar to one another with having two decay components although their mean emission lifetime increases with the increase of the hydrothermal-treatment time. The fast decay component of 60 ps has been attributed to the intrinsic recombination of electrons in the conduction band whereas the slow decay component of 270 ps is considered to arise from the

radiative recombination of charge carriers in surface states.[37-39] Thus, the increase of the mean lifetime with the increase of the hydrothermal-treatment time is due to the fractional-amplitude increment of the slow-decay component. This also supports our suggestion made with Figure 3-7 that surface states increase with the hydrothermal-treatment time of $CdSe \cdot (en)_{0.5}$ nanorods. The decay kinetic profile of the near-infrared shoulder band of photoluminescence at ~790 nm, which arises mainly from selenium vacancies, has been found to be too slow to be observed with our picosecond kinetic spectrometer because radiative transition from the relaxed excited state (2s) to the ground state (1s) of F-centers (selenium vacancies with two trapped electrons) is not allowed by the spectroscopic selection rule of Laporte.

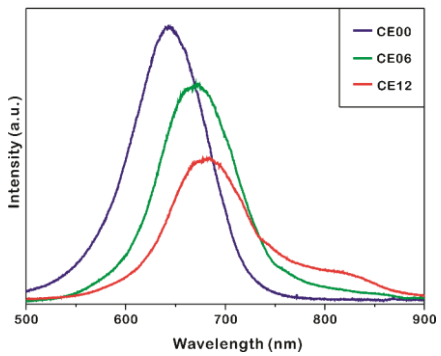

Figure 3-7 Photoluminescence spectra of indicated nanostructures suspended in ethanol with excitation at 355 nm.

In the review process of this manuscript, it has been found that our nanostructures have low PLQYs of 4.4 (CE00), 3.8 (CE06), and 3.2% (CE12), in consideration of the fact that PLQYs of reported CdSe nanocrystals are

usually 10–86%. In general, the relaxation dynamics of photoexcited charge carriers proceed through radiative decay and non-radiative decay; while radiative decay is determined by the intrinsic properties of the exciton that depends on the size, shape, and composition of a nanocrystal, non-radiative decay is primarily determined by the conditions of surface states on the nanostructures.[34] Thus, the surface defects of the planar defects (stacking faults and twinning boundaries) or volume defects (voids) in our as-prepared CdSe nanostructures can facilitate charge carrier-quenching, and therefore the photoluminescence decay dynamics is dominated by non-radiative processes, resulting in low PLQYs. Thus, the fast photoluminescence decay times of our as-prepared CdSe nanostructures are strongly correlated with their low PLQYs.

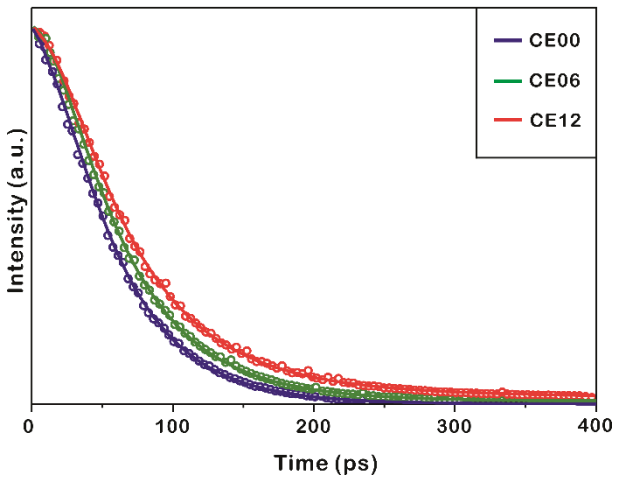

Figure 3-8. Photoluminescence kinetic profiles of indicated nanostructures suspended in ethanol at room temperature, and solid lines are best-fitted curves to extract kinetic constants.

Table 3-2. Photoluminescence Decay Constants Extracted from Figure 8

sample	decay time / ps	mean lifetime / ps
CE00	60 (96%) + 270 (4%)[a]	68
CE06	60 (87%) + 270 (13%)	85
CE12	60 (62%) + 270 (38%)	140

[a]Initial intensity percentage of each component.

3. 5. Conclusion

Porous hexagonal wurtzite CdSe nanorods having an average length of 210 nm and a typical diameter of 20 nm with multiple voids ranging from 8 to 12 nm have been prepared facilely by treating orthorhombic $CdSe \cdot (en)_{0.5}$ nanorods hydrothermally. It has been found that various crystalline imperfections such as stacking faults and twinning planes appear during the hydrolysis time between 3 and 9 h and disappear subsequently during the hydrolysis time between 9 and 12 h to release lattice mismatch strains. Selenium vacancies are rich particularly in porous CdSe nanorods, suggesting that Se anions have diffused out faster than Cd cations during the hydrothermal process of $CdSe \cdot (en)_{0.5}$ nanorods and that the diffusion of Se anions is rapid near crystal defects. Due to the imbalance of in-and-out atomic diffusion, point defects of atomic vacancies are heavily generated in CdSe nanorods to produce volume defects of voids eventually. The photoluminescence of CdSe nanorods shifts to the red and decreases in intensity with the increase of the hydrolysis time as surface states and selenium vacancies increase. The mean lifetime of photoluminescence increases with the increase of the hydrothermal-treatment time as the fractional amplitude of the slower-

decay component, arising from the radiative recombination of charge carriers in surface states, increases.

3A. 7. References

(1) Liu, Y.; Goebl, J.; Yin, Y. *Chem. Soc. Rev.* **2013**, *42*, 2610−2653.

(2) Jun, Y.-W.; Choi, J.-S.; Cheon, J. *Angew. Chem. Int. Ed.* **2006**, *45*, 3414−3439.

(3) Kim, J.-Y.; Lee, D.; Kim, H. J.; Lim, I.; Lee, W. I.; Jang, D.-J. *J. Mater. Chem. A* **2013**, *1*, 5982−5988.

(4) Kim, Y.; Kim, H.-B.; Jang, D.-J. Facile *J. Mater. Chem. A* **2014**, *2*, 5791−5799.

(5) Kim, H.-B.; Kim, H.; Lee, W. I.; Jang, D.-J.. *J. Mater. Chem. A* **2015**, *3*, 9714−9721.

(6) Liang, H.-W.; Liu, J.-W.; Qian, H.-S.; Yu, S.-H. *Acc. Chem. Res.* **2013**, *46*, 1450−1461.

(7) Wang, X. D.; Li, Z. D.; Shi, J.; Yu, Y. H. *Chem. Rev.* **2014**, *114*, 9346−9384 .

(8) Zhang, S; Tang, N; Jin, W.; Duan, J.; He, X.; Rong, X.; He, C.; Zhang, L.; Qin, X.; Dai, L.; Chen, Y.; Ge, W.; Shen, B.. *Nano Lett.* **2015**, *15*, 1152−1157.

(9) Zhuang, Z.; Peng, Q.; Li, Y. *Chem. Soc. Rev.*, **2011**, *40*, 5492–5513.

(10) Deng, Z.-X.; Li, L.; Li, Y. *Inorg. Chem.* **2003**, *42*, 2331–2341.

(11) Huang, X.; Li, J.; Zhang, Y.. *J. Am. Chem. Soc.* **2003**, *125*, 7049–7055.

(12) Yang. J.; Xue, C.; Yu, S.-H.; Zeng, J.-H.; Qian, Y.-T. *Angew. Chem. Int. Ed.* **2002**, *41*, 4697−4700.

(13) Kim, J.-Y.; Kim, M. R.; Park, S.-Y.; Jang, D.-J. *CrystEngComm* **2010**, *12*, 1803−1808.

(14) Kim, Y.; Kim, J.-Y.; Jang, D.-J. *J. Phys. Chem. C* **2012**, *116*, 10296−10302.

(15) Kim, Y.; Jang, D.-J. *CrystEngComm* **2014**, *16*, 6989−6995.

(16) Zhang, J.; Yu, J.; Zhang, Y.; Li, Q.; Gong, J. R. *Nano Lett.* **2011**, *11*, 4774–4779.

(17) Hull, D.; Bacon, D. J. *Introduction to Dislocations*; 5th ed.; Elsevier: Oxford, 2011.

(18) Hughes, S. M.; Alivisatos, A. P. *Nano Lett.* **2013**, *13*, 106–110.

(19) Utama, M. I. B.; de la Mata, M.; Magen, C.; Arbiol, J.; Xiong, Q. *Adv. Funct. Mater.* **2013**, *23*, 1636−1646.

(20) Meng, F.; Estruga, M.; Forticaux, A.; Morin, S. A.; Wu, Q.; Hu,Z.; Jin, S. A *ACS Nano* **2013**, *7*, 11369−11378.

(21) Liu, M.; Jing, D.; Zhou, Z.; Guo, L.. *Nat. Commun.* **2013**, *4*, 2278.

(22) Utama, M. I. B.; Zhang, Q.; Jia, S.; Li, D.; Wang, J.; Xiong, Q.. *ACS Nano* **2012**, *6*, 2281–2288.

(23) Kumar, M.; Singh, V. N.; Mehta, B. R.; Singh, J. P. *J. Phys. Chem. C* **2012,** *116*, 5450−5455.

(24) Maestre, D.; Häussler, D.; Cremades, A.; Jäger, W.; Piqueras, J.,. *J. Phys. Chem. C* **2011**, *115*, 18083−18087.

(25) de la Mata, M.; Magén, C.; Caroff, P.; Arbiol, J, *Nano Lett.* **2014**, *14*, 6614–6620.

(26) Zhao, L.; Hu, L.; Fang, X. *Adv. Funct. Mater.* **2012**, *22*, 1551–1566.

(27) Li, L.; Lu, H.; Deng, K., *J. Mater. Chem. A* **2013**, *1*, 2089–2093.

(28) Zhu, C.; Du, D; Eychmüller, A.; Lin, Y., *Chem. Rev.* **2015**, DOI: 10.1021/acs.chemrev.5b00255.

(29) Valtchev, V.; Tosheva, L. *Chem. Rev.* **2013**, *113*, 6734−6760.

(30) Wang, W.; Dahl, M.; Yin, Y., *Chem. Mater.* **2013**, *25*, 1179−1189.

(31) Peng, X. G.; Manna, L.; Yang, W. D.; Wickham, J.; Scher, E.; Kadavanich, A.; Alivisatos, A. P. *Nature* **2000**, *404*, 59–61.

(32) Peng, Z. A.; Peng, X. G. *J. Am. Chem. Soc.* **2001**, *123*, 1389–1395.

(33) Xu, W.; Zhang, Y.; Cheng, G.; Jian, W.; Millett, P. C.; Koch, C. C.; Mathaudhu, S. N.; Zhu, Y., *Nat. Commun.* **2013**, *4*, 2288.

(34) Tang, Y.; Ouyang, M., *Nat. Mater.* **2007**, *6*, 754−759.

(35) Wang, G.; Huang, B.; Li, Z.; Lou, Z.; Wang, Z.; Dai, Y.; Whangbo, M.-H. *Sci. Rep.* **2015**, *5*, 8544.

(36) Brasil, M. J. S. P.; Motisuke, P.; Decker, F.; Moro, J. R. *J. Phys. C: Solid State Phys.* **1988**, *21*, 3141−3150.

(37) Jiang, Z.-J.; Kelley, D. F. *J. Phys. Chem. C* **2010**, *114*, 17519−17528

Kim, M. R.; Chung, J. H.; Lee, M.; Lee, S.; Jang, D.-J. *J. Colloid. Interface Sci.* **2010**, *350*, 5−9.

Chapter 4. Fabrication and Application of Morphology-Controlled Anatase TiO_2 Nanostructures

Part 4A. Morphological variation of anatase TiO_2 crystals *via* formation of titanium glycerolate precursors under microwave Irradiation[†]

4A. 1. Abstract

The morphologies of anatase TiO_2 crystals have been varied facilely from rod-like structures to various hedgehog-like hierarchical structures *via* forming titanium glycerolate precursors as sacrificial templates. The morphologies of the precursors have been controlled readily under microwave irradiation by adjusting the relative solvent volumes of isopropanol and glycerol. The simple hydrolysis of as-prepared titanium glycerolate precursors for 10 min under microwave irradiation has yielded intrinsic morphology-retained anatase TiO_2 nanostructures. The smooth surfaces of the precursors have been turned into rough surfaces of anatase TiO_2 crystals during the hydrolysis, suggesting that our as-prepared anatase TiO_2 nanostructures have highly potential applications in diverse fields such as photocatalysts and solar cells. It has been suggested that the variation of the relative volume fractions of isopropanol and glycerol having significantly different boiling points and viscosity values has changed the nucleation and growth kinetics to control the morphologies as well as the sizes of titanium glycerolate precursors..

[†]This is reproduced from Hyung-Bae Kim and Du-Jeon Jang, *CrystEngComm*, **2015,** *17***,** 3325-3332.

4A. 2. Introduction

With the growth of interest in the field of nanotechnology, the development of the facile and rapid synthetic methods of nanostructures with functional properties has become increasingly important.[1-5] Particularly, the syntheses of metal oxide nanomaterials having controllable shapes and sizes have been extensively explored because of their wide applications in Li-ion batteries, gas sensors, sensitized solar cells, and photocatalysts.[6-10] Anatase, which is one of the four polymorphs of TiO_2, has been widely utilized due to its photoreactivity, chemical stability, favorable band-edge positions, strong optical absorption, and inexpensive cost.[11] Since the properties of anatase TiO_2 nanostructures are strongly dependent on their morphologies and surface structures, extensive efforts have been devoted to control their sizes and shapes delicately.[12,13] In solution-based synthetic methods of anatase TiO_2 crystals, the most useful strategy to control shapes and surface structures is the introduction of additives such as surfactants or ions,[11-13,21] which affect kinetic and thermodynamic parameters significantly during nucleation and growth processes.[11] These additives are preferentially adsorbent on certain facets of growing crystals, changing their surface energies. Thus, they can tune the growth rate of crystals and tailor the sizes and surface structures of the growing crystals. However, it is challenging to synthesize the shape-controlled anatase TiO_2 crystals because the conventional sol-gel reaction is generally too highly moisture-sensitive, thus making it difficult for additives to control the growth kinetics of anatase

crystals.[11] Unlike conventional one-pot methods, diverse two-step fabrication approaches of anatase TiO_2 crystals through a Ti-containing crystalline precursor (TCP) have been also reported.[14-21] TCPs, which are potential materials to be transformed into anatase TiO_2 nanostructures, are stable against moisture, so that we can control their shapes rather easily. Thus, TCPs can be employed as shape-determining sacrificial templates. The subsequent calcination or hydrolysis process can transform TCP nanostructures into anatase TiO_2 nanocrystals. In most cases, the intrinsic morphologies of TCPs have been preserved after conversion into anatase TiO_2 crystals. Consequently, with the assistance of TCP, nanostructured anatase TiO_2 crystals can have the novel morphologies that cannot be realized by conventional one-pot synthetic methods. There are three major challenging problems in both conventional and precursor-based synthetic methods. Most of the synthetic conditions involve seriously harmful organic surfactants or ionic additives to control the sizes and shapes of nanostructures; those additives can be heavily coated on reactive surfaces to deteriorate the performances of TiO_2 nanomaterials. Also, the reported methods often require too long reaction times of 6-24 h. Finally, an additional post-annealing (calcination) process at a high temperature of 400-700 ℃ is necessarily required to generate the desired crystalline phase. Thus, those challenging features have limited the economical use of anatase TiO_2 nanomaterials.

The use of microwave irradiation as a nonclassical heating source has become increasingly popular in time-consuming synthetic processes.[2,22,23]

Microwave superheating, which is significantly different from conventional heating methods, can be triggered by dipolar-polarization and ionic-conduction mechanisms.[22] Microwave can penetrate the reactor wall and thereby excite molecules or ions selectively, raising the reaction temperature uniformly and quickly throughout the whole liquid volume.[23] The thermal and kinetic features of microwave irradiation not only reduce the reaction time by several orders of magnitude but also suppress side reactions substantially. Sometimes, microwave heating causes unique outcomes that cannot be achieved or duplicated by conventional heating.[2] Therefore, microwave can be used to accelerate the reaction rate and to induce unique properties in the syntheses of inorganic nanostructures. Notwithstanding the above mentioned advantages, however, the microwave-assisted synthesis of anatase TiO_2 nanostructures in the solution phase has rarely been reported, and reported anatase TiO_2 structures prepared *via* microwave-assisted routes are usually aggregates of irregular nanocrystals without having well-defined morphologies.[24,25]

In this work, we have developed a rapid and straightforward microwave-assisted two-step synthetic strategy for the preparation of anatase TiO_2 nanostructures having well-defined morphologies, which are controlled by the controlling the structures of titanium glycerolate precursors as TCPs. Microwave irradiation has enabled not only the rapid formation of titanium glycerolate precursors in 10 min but also the rapid hydrolysis of the precursors within 10 min. The simple hydrolysis of the precursors, whose structures have been controlled by adjusting the volume fraction of isopropanol in the solvent

mixture of glycerol and isopropanol, has yielded anatase TiO_2 crystals having morphological variation from rod-like crystals to diverse hierarchical nanostructures (Figure 1); whereas rod-like anatase TiO_2 crystals have been prepared in the absence of isopropanol, hierarchical anatase TiO_2 nanostructures have been synthesized at high solvent-volume fractions of isopropanol.

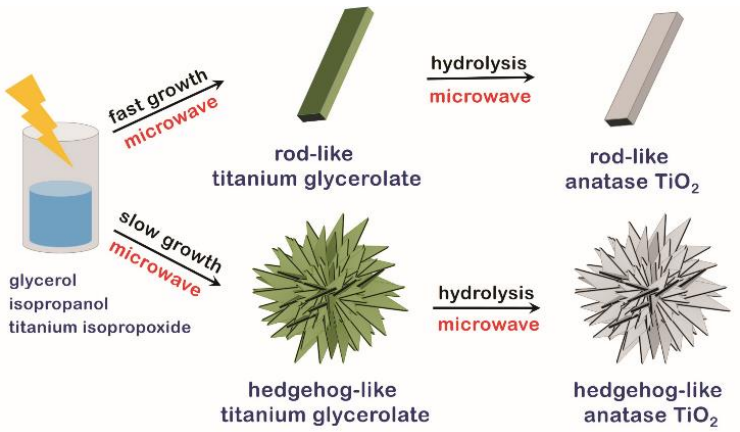

Figure 4A-1 Schematic illustration for two-step synthetic processes of anatase TiO_2 crystals under microwave irradiation.

4A. 3. Experimental Details

Materials. Titanium(IV) isopropoxide (l, >97%), glycerol (l, >99%), isopropanol (l, >99.9%), and ethanol (l, >99%) were used as purchased from

Sigma-Aldrich. Ultrapure deionized water (>17 MΩ cm) from a Millipore Milli-Q system was used throughout the experiments.

Titanium glycerolate precursors. Titanium glycerolate precursors were synthesized according to the reported procedure with modification.[17,18] 2.0 mmol of titanium isopropoxide was added to 40 mL of a solvent mixture of isopropanol and glycerol with a certain volume fraction of isopropanol (R). The mixture was maintained at 40 °C under vigorous stirring for 5 min and sonicated in an ultrasonic bath for 5 min to make the solution homogeneously clear. The clear solution was transferred into a 300 mL reactor and irradiated by a Samsung HV-367AWJ microwave system (2.45 GHz, 450 W) for 10 min. The white precipitate was harvested by centrifugation, washed with ethanol and water for three times, and dried at 40 °C for further usage. Titanium glycerolate precursors prepared at R values of 0.00, 0.08, 0.20, 0.40, 0.67, and 0.85 will be designated as P00, P08, P20, P40, P67, and P85, respectively.

Anatase TiO_2 crystals. 100 mg of a titanium glycerolate precursor was dispersed in 30 ml of water and subject to microwave irradiation for 10 min. The white precipitate was centrifuged, washed with ethanol and water for three times, and dried at 40 °C. Anatase TiO_2 crystals obtained through the hydrolysis of the titanium glycerolate precursors of P00, P08, P20, P40, P67, and P85 will be designated as A00, A08, A20, A40, A67, and A85, respectively.

Characterization. Transmission electron microscope (TEM) images were measured with a JEOL JEM-3000F microscope. The morphologies of the samples were measured with a JEOL JSM-6700F scanning electron microscope

(SEM). High-resolution X-ray diffraction (HRXRD) patterns were recorded using a Bruker D8 DISCOVER diffractometer (Cu K_α radiation, $\lambda = 0.154178$ nm). Thermogravimetric analysis (TGA) curves were measured with using a TA Instruments Q5000 thermal analyzer; a sample weighing approximately 3 mg was loaded into a platinum pan and then placed in the instrument under a nitrogen atmosphere. While Fourier transform infrared (FTIR) spectra were obtained using Nicolet 6700 FTIR spectrometer, Raman spectroscopic measurements were done with a Horiba Jobin Yvon T64000 Raman spectrometer that used the 514.5 nm of an Ar ion laser as the light source. XPS spectra were collected using a Thermo Scientific Sigma Probe ESCA spectrometer (Al Kα X-ray source) and the measured binding energies were calibrated with the C 1s peak at 284.5 eV of contaminated carbon.

4A. 4. Results and Discussion

As shown in the SEM images of Figure 2, without using any surfactants or ionic additives, the morphologies of titanium glycerolate precursors have been successfully controlled by adjusting the fraction of isopropanol in the solvent mixture of glycerol and isopropanol under microwave irradiation. The rod-like morphology of titanium glycerolate crystals having an average length of 230 nm and a typical width of 60 nm with narrow size distribution has been obtained at R = 0.00 (Figure 2a and Table 1). Titanium glycerolate crystals prepared at R = 0.08 also have rod-like shapes with an increased average aspect ratio of 6.6 although their lengths have increased almost twice. However, titanium

glycerolate precursors prepared at R ≥ 0.20 have morphologies of hedgehog-like hierarchical nanostructures, which consist of numerous 1D building blocks (Figure 4A-2). The building blocks have been found to reach the maximum values of 870 nm in their average length and 17.4 in their average aspect ratio at R = 0.67 (Table 1). Thus, our results indicate that the nanostructured 1D building blocks of the hierarchical titanium glycerolate precursors gradually become sharp-pointed as R increases from 0.00 to 0.67. However, Figure S1 in the SI and Table 1 indicate that the hierarchical structures of titanium glycerolate precursors become somewhat blunted as R increases from 0.67 to 0.85. Overall, our results have shown that the morphologies of titanium glycerolate precursors can be controlled from rod-like 1D structures to hedgehog-like hierarchical 3D structures by adjusting the volume fractions of isopropanol in solvent mixtures of isopropanol and glycerol.

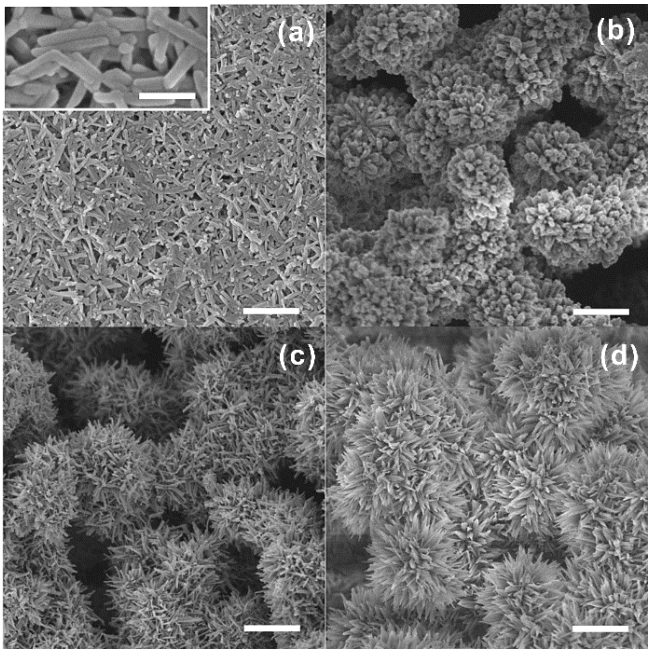

Figure 4A-2 SEM images of as-prepared titanium glycerolate precursors P00 (a), P20 (b), P40 (c), and P67 (d). Each scale bar indicates 1 μm, whereas the scale bar inside the inset indicates 200 nm.

As titanium glycolate crystals have been known to react with hot water to form anatase TiO_2 crystals without employing any calcination process,[15-16] we have hydrolyzed our titanium glycerolate precursors with water to produce anatase TiO_2 nanostructures. Figure 4A-3 shows indeed that anatase TiO_2 crystals have been prepared *via* simple hydrolysis of as-prepared titanium glycerolate precursors for 10 min under microwave irradiation. It is remarkable that the produced anatase TiO_2 nanostructures have almost retained the respective intrinsic morphologies of hydrolyzed titanium glycerolate precursors. We attribute this to the rapid hydrolysis of precursors under microwave irradiation; the short contact time with hot water could minimize the

morphological deformation of titanium glycerolate precursors during hydrolysis, producing anatase TiO_2 crystals with the original shapes of the precursors.

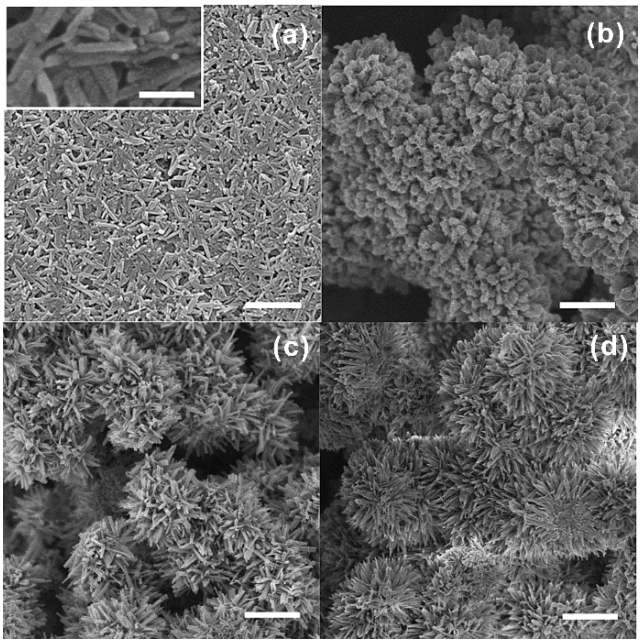

Figure 4A-3 SEM images of anatase TiO_2 A00 (a), A20 (b), A40 (c), and A67 (d) produced by the hydrolysis of titanium glycerolate precursors P00, P20, P40, and P67, respectively. Each scale bar indicates 1 μm, whereas the scale bar inside the inset indicates 200 nm.

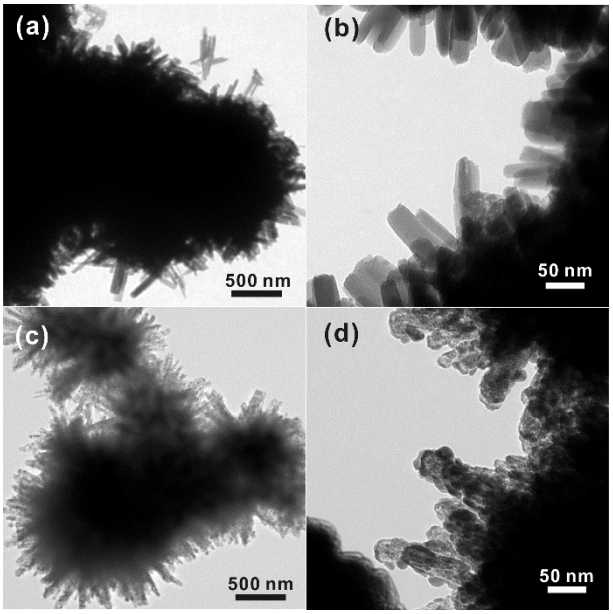

Figure 4A-4 TEM images of titanium glycerolate P40 (a,b) and anatase TiO_2 A40 (c,d).

The TEM images of Figure 4A-4 reveal detailed structural changes of titanium glycerolate P40 *via* hydrolysis under microwave irradiation to form anatase TiO_2 A40. As mentioned earlier with SEM images, the general shapes of P40 crystals are retained in A40 crystals. However, the TEM images of Figure 4c is brighter than that of Figure 4a due to the removal of glycerol moiety during the hydrolysis of P40 to form A40. Furthermore, the P40 crystals of Figure 4d have rougher surfaces than the A40 crystals of Figure 4A-4b. After the hydrolysis, P40 crystals having smooth surfaces have been turned into A40 crystals having irregular surfaces. It is considered that our as-prepared TiO_2 nanostructures would have highly potential applications in diverse fields such as photocatalysts and solar cells.

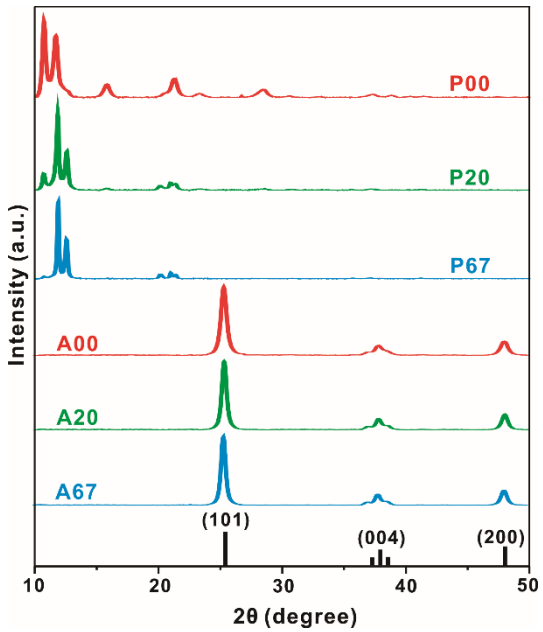

Figure 4A-5 HRXRD patterns of indicated titanium glycerolate precursors and anatase TiO_2 crystals. The standard diffraction pattern of anatase TiO_2 is also shown in the bottom.

The HRXRD patterns of as-synthesized titanium glycerolate precursors in Figure 4A-5 are in good agreement with those of reported titanium glycerolate crystals.[17,18] Since isopropanol and glycerol have high loss-tangent values of 0.79 and 0.65, respectively,[2,26] our solvent mixtures of isopropanol and glycerol can convert microwave energy efficiently into heat. As a result, titanium glycerolate crystals have been found to grow rapidly within just 10 min in our every solvent mixture. The sharp and intensive HRXRD peaks of titanium glycerolate crystals indicate that the precursors have highly crystallized structures, thus suggesting that our microwave-assisted synthetic method is economically efficient in comparison with reported time-consuming

methods.[14,15,17,18] It is also noticeable that the intensity of the HRXRD peak at $2\theta = 10.6°$ decreases but that at $2\theta = 12.5°$ increases with the increase of R. It is considered that the growth of titanium glycerolate might be inhibited at a certain direction ($2\theta = 10.6°$) but promoted at another direction ($2\theta = 12.5°$) by the presence of isopropanol. In general, crystallite sizes decrease as the growth rate increases.[27,28] Since the growth rate increases exponentially with the growth temperature, the variation of crystallite sizes for titanium glycerolate precursors suggests that the growth temperatures of titanium glycerolate depend extensively on the R value. Because a reaction under microwave irradiation occurs at the boiling temperature of the employed solvent (290 and 82 ℃ for glycerol and isopropanol, respectively), the growth temperature is considered to decease substantially with the increase of R. Whereas the HRXRD peaks of titanium glycerolate precursors vary with the change of R, the HRXRD peaks of anatase TiO_2 have been found to be almost invariant in their relative intensities. All the HRXRD patterns of our as-prepared anatase TiO_2 crystals have been found to match well with the reference pattern of the anatase TiO_2 structure (JCPDS card no. 84-1286). Considering that HRXRD peaks of titanium glycerolate crystals have not been observed at all in the HRXRD patterns of our as-prepared anatase TiO_2 nanostructures, we suggest that our microwave-assisted hydrolysis method has successfully transformed titanium glycerolate precursors into anatase TiO_2 crystals within 10 min. Figure S3 in the SI shows that the band width of the HRXRD peak due to the (101) planes of anatase TiO_2 crystals becomes gradually narrow as the R value increases.

Using the Scherrer equation[19] and assuming that peak broadening arises entirely from size effects, we have calculated the average crystallite sizes of anatase TiO_2 nanostructures by using the (101) peak at 2θ of 25.4° (Table 1). Because the anatase TiO_2 crystals have been produced by the hydrolysis of titanium glycerolate precursors, the variation trend of crystallite sizes for anatase TiO_2 crystals resembles that for titanium glycerolate precursors, although the average crystallite sizes of anatase TiO_2 nanostructures are substantially smaller than the respective ones of employed titanium glycerolate precursors.

The Raman analysis has also been considered to be an effective tool for determining the crystallinity of anatase TiO_2 materials.[29,30] As-prepared TiO_2 crystals have well-crystallized anatase TiO_2 structures; the observed six strong peaks have arisen entirely from the standard Raman modes of $A_{1g} + 2B_{1g} + 3E_g$ in the anatase TiO_2 phase.[29] And the narrowing of the lowest-E_g Raman peaks with the increment of R agrees with the narrowing of the HRXRD peaks in Figure S3; the average crystallite size of our as-prepared TiO_2 nanostructures increases with the increase of the R value.[30] Taken into consideration together, our rapid microwave-assisted hydrolysis method can be suggested to produce high-quality anatase TiO_2 nanostructures as well-defined as TiO_2 structures produced *via* a conventional calcination or hydrolysis method.

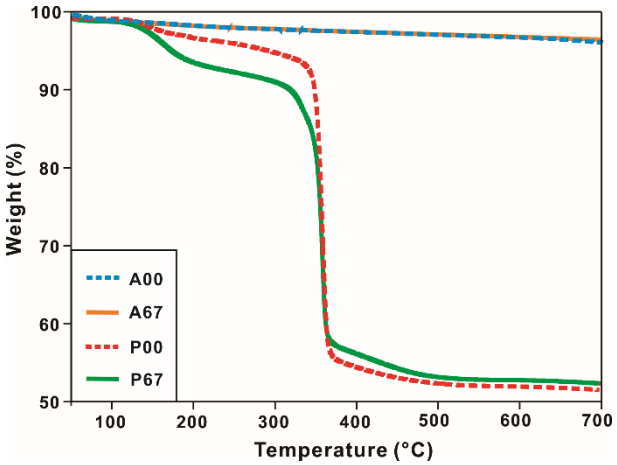

Figure 4A-6 TGA curves of indicated titanium glycerolate precursors and anatase TiO_2 crystals.

Thermo-gravimetric analysis (TGA) has been used to investigate the chemical compositions of as-prepared titanium glycerolate precursors and anatase TiO_2 crystals. Figure 4A-6 shows typical TGA curves recorded under a nitrogen atmosphere at a heating rate of 10 ℃ min^{-1}. As illustrated in Figure 4A-6, P00 has just one-stage weight degradation but P67 has two-stage weight degradation. The common degradation stage of P00 and P67 which occurs between 300–400 ℃ is in agreement with the bulk degradation of the glycerol moiety of titanium glycerolate reported in literature.[17] An additional weak degradation stage of P67 between 150–250 ℃ suggests that the isopropanol residue existing inside the crystals of P67 has also disappeared in that temperature range. From the first-derivative TGA curves (Figure S5 in the SI), the major peak arising from the removal of the glycerol moiety has been observed at 357 ℃ for both P00 and P67 while the minor peak resulting from the removal of the isopropanol residue has been observed at 163 ℃ for P67.

Unlike titanium glycerolate precursors, our as-prepared anatase TiO_2 nanostructures have not shown any degradation stage in both TGA and differential TGA curves in the temperature range of 50-700 ℃, indicating that there is no organic moiety or residue at all inside anatase TiO_2 nanostructures. Thus, we assert again that our microwave-assisted hydrolysis method can successfully transform titanium glycerolate precursors into anatase TiO_2 nanostructures within 10 min.

The FTIR spectra of Figure 4A-7 also support the TGA results that the chemical compositions of titanium glycerolate precursors have been dramatically changed during the hydrolysis process to produce anatase TiO_2 nanostructures. Whereas the FTIR patterns of titanium glycerolate precursors resemble the FTIR pattern of glycerol in appearance due to their inherently existing glycerol moiety, the FTIR patterns of anatase TiO_2 crystals do not show any vibrational normal modes which can be assigned to organic species.[14,17,31,32] The FTIR peaks of both the O-H stretching and the O-H bending modes, which are strong in titanium glycerolate precursors, are still observed very weakly in anatase TiO_2 crystals. The residual O-H functional group of TiO_2 surfaces is considered to be crucial for most applications of TiO_2 materials because hydrophilic surfaces have a good affinity with various guest molecules *via* hydrogen bonds. While the FTIR peaks from the C-C-O and the Ti-O-C stretching modes of titanium glycerolate have been disappeared completely, the FTIR peak from the Ti-O-Ti stretching mode has been considerably broadened and amplified due to the prevalence of Ti-O-Ti bonds throughout the anatase

TiO_2 nanostructures. Consequently, considering both the FTIR and the TGA results, we declare that the chemical composition of titanium glycerolate has been transformed perfectly into that of anatase TiO_2 during a rapid hydrolysis process of 10 min under microwave irradiation.

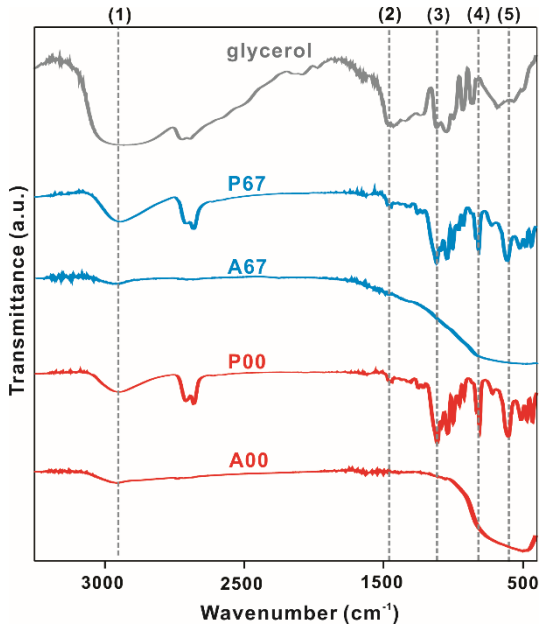

Figure 4A-7 FTIR spectra of glycerol, indicated titanium glycerolate precursors, and indicated anatase TiO_2 crystals: (1) O-H stretching at 3500 ~ 3000 cm^{-1}, (2) O-H bending at 1440 cm^{-1}, (3) C-C-O stretching at 1121 cm^{-1}, (4) Ti-O-C stretching at 813 cm^{-1}, and (5) Ti-O-Ti stretching at 612 cm^{-1}.

To understand the formation mechanisms of titanium glycerolate precursors and anatase TiO_2 crystals in detail, we have measured the XPS spectra of O 1s in Figure 8 as well as the XPS spectra of Ti 2p. The binding energies of the O 1s and the Ti 2p XPS spectra of titanium glycerolate precursors increase with the increase of R whereas those of anatase TiO_2

crystals remain invariant. To investigate the specific binding environments of O and Ti atoms, we have deconvoluted each of the O 1s and the Ti 2p XPS spectra into distinct Gaussian curves.[33,34] The deconvoluted O 1s XPS spectra of Figure 8 show that the binding environments of oxygen atoms in titanium glycerolate precursors are quite different from those in anatase TiO_2 nanostructures; although the dominant oxygen environment of titanium glycerolate precursors arises from Ti-O-C bonds due to their glycerol moiety, that of anatase TiO_2 crystals arises from Ti-O-Ti bonds due to the prevalence of TiO_2 crystals throughout the structure. the binding environments of Ti atoms in titanium glycerolate crystals are also very different from those in anatase TiO_2 crystals; the deconvoluted curves arising from Ti^{3+} ions have been observed only in titanium glycerolate precurTors. Thus, the XPS results also reveal that titanium glycerolate precursors have been successfully hydrolyzed in 10 min under microwave irradiation to form anatase TiO_2 nanostructures. On the other hand, Table S1 in the SI shows that the contribution of Ti-O-C bonds in the O 1s spectra of titanium glycerolate precursors decreases whereas that of Ti-O-(Ti,H) bonds increases with the increase of R. This observation suggests that although the contribution of organic O-C bonds decreases, that of inorganic O-H bonds increases when isopropanol was dominant in the solvent mixture of glycerol and isopropanol during the preparation of titanium glycerolate crystals. In addition, the contribution of Ti^{3+} peaks in the Ti 2p XPS spectra of titanium glycerolate precursors increases with the increase of R, suggesting that the formation rate of precursor crystals can be retarded by increasing the

concentration of isopropanol in the solvent mixture (see below). Overall, our XPS results, together with the other presented results, have shown that the morphologies of titanium glycerolate precursors and subsequently produced anatase TiO_2 nanostructures can be controlled effectively by adjusting the volume fraction of isopropanol only.

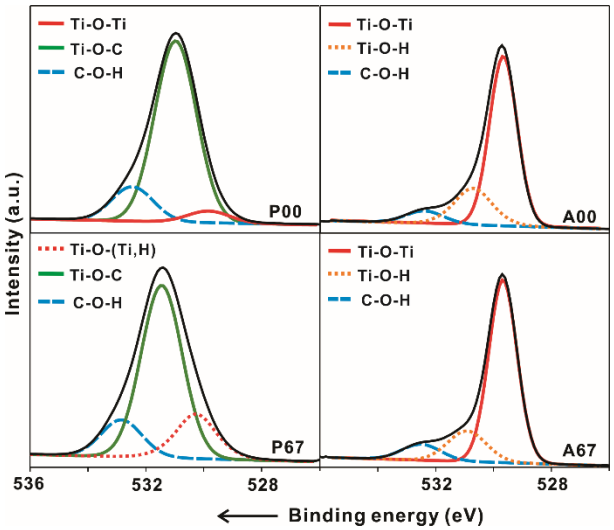

Figure 4A-8 O 1s XPS spectra of indicated titanium glycerolate precursors (left) and anatase TiO_2 crystals (right). Each XPS spectrum has been deconvoluted into three Gaussian curves arising from indicated oxygen environments.

Summarizing the above presented results, we can propose the possible formation mechanisms of titanium glycerolate precursors in terms of the LaMer theory (Figure 9);[6,27,35] monomers can play a crucial role in nucleation and growth processes. Only if the concentration of monomers is above the critical supersaturation (S_c), they can overcome the energy barrier for nucleation and

thus can form stable nuclei. Since the nuclei can grow by incorporating additional monomers present in the reaction medium, the concentration of monomers in the solution will drop quickly to a level below S_c. As long as the concentration of monomers is held below the threshold of S_c, no additional nucleation events except for the growth of nuclei will occur. Therefore, certain factors that change the nucleation and growth kinetics can determine the morphology, the size, and the dispersity of the product.

As mentioned with the HRXRD spectra of Figure 4A-5, the reaction kinetics depends significantly on the reaction temperature. At low R values, the glycerol-like solvent mixture can be heated up nearly to the boiling point of glycerol (290 ℃), so that the growth rate can be considerably boosted. Consequently, the concentration of the monomers rapidly reaches to the critical supersaturation within a very short time, resulting in a burst of nucleation. Since the employed polyol molecules of glycerol have been known to have a nature of producing various 1D nanostructures,[17,36] the nuclei generated at low R values can grow rapidly and homogeneously into rod-like 1D structures with assistance of glycerol molecules. At high R values, however, because the solvent mixture is isopropanol-like, the reaction temperature can be limited nearly to the boiling point of isopropanol (82 ℃), so that monomers are produced gradually and depleted slowly during all the reaction stages. As a result, the nucleation and the growth of titanium glycerolate proceed over an extended period of time, and thus the nuclei can grow slowly *via* a significantly different way. At low growth temperatures (at high R values), growing 1D

building blocks can be assembled into hedgehog-like hierarchical 3D structures to decrease the total surface energy. The temperature-dependent growth kinetics of titanium glycerolate can also be observed as the increase of Ti^{3+} peaks with the increase of R. Because Ti^{3+} ions are considered to be highly unstable surface defects,[37] the generation of Ti^{3+} ions can be facilitated mainly under kinetic conditions (at low growth temperatures) instead of thermodynamic conditions (at high growth temperatures). Thus, at high growth temperatures (at low R values), the generation of Ti^{3+} surface defects is retarded because the thermodynamic pathway has a tendency to produce the most stable product.

Because the employed solvents of glycerol and isopropanol have extremely different viscosity values (934 cP for glycerol and 1.96 cP for isopropanol), the viscosity of the solvent mixture could also be another decisive factor to determine the morphology of titanium glycerolate. In general, the diffusion coefficient (D) of monomers is correlated to the viscosity (η) of the solvent medium by the Stokes−Einstein equation: $D = k_B T/6\pi\eta R_h$, where k_B is the Boltzmann constant, T is the absolute temperature, and R_h is the hydrodynamic radius of a monomer.[38] When the solvent viscosity is low at a high R value, particles can grow bigger due to the high collisional frequency with monomers. In summary, the variation of the relative volume fractions of isopropanol and glycerol having significantly different boiling points and viscosity values can change the nucleation and growth kinetics to control the morphologies as well as the sizes of titanium glycerolate precursors. Finally, as-prepared titanium glycerolate precursors having novel morphologies can be used as sacrificial

templates to produce anatase TiO_2 crystals facilely *via* microwave-assisted hydrolysis.

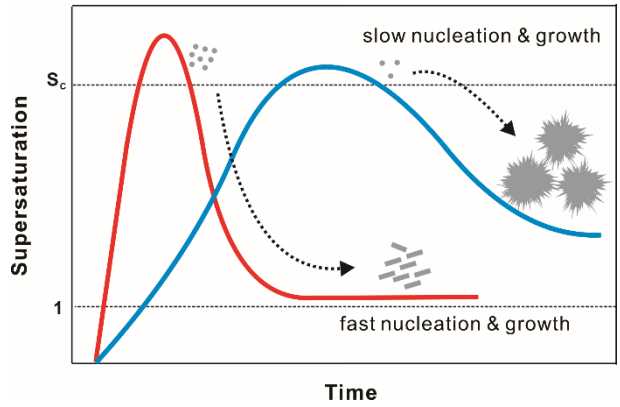

Figure 4A-9 Plausible growth mechanisms of titanium glycerolate precursors.

4A. 5. Conclusion

Without using any additional surfactants or ionic additives, we have controlled the morphologies of anatase TiO_2 crystals from rod-like structures to various hedgehog-like hierarchical structures *via* forming titanium glycerolate precursors as sacrificial templates. The morphologies of the precursors have been controlled readily under microwave irradiation by adjusting the relative solvent volumes of isopropanol and glycerol; whereas rod-like titanium glycerolate structures have been prepared in the absence of isopropanol, hierarchical titanium glycerolate structures have been synthesized at high

solvent-volume fractions of isopropanol. The simple hydrolysis of as-prepared titanium glycerolate precursors for 10 min under microwave irradiation has yielded intrinsic morphology-retained anatase TiO_2 nanostructures, although smooth surfaces of the precursors have been turned into rough surfaces of anatase TiO_2 crystals during the hydrolysis. It has been found that the variation of the relative volume fractions of isopropanol and glycerol having significantly different boiling points and viscosity values has changed the nucleation and growth kinetics to control the morphologies as well as the sizes of titanium glycerolate precursors. Our presenting method is suggested to contribute considerably to the development of a new synthetic strategy for the morphology-controlled fabrication of inorganic nanomaterials under microwave irradiation.

4A. 7. References

(1) Liu, Y.; Goebl, J.; Yin, Y. *Chem. Soc. Rev.*, **2013**, *42*, 2610−2653.

(2) Baghbanzadeh, M.; Carbone, L.; Cozzoli, P. D.; Kappe, C. O. *Angew. Chem. Int. Ed.* **2011**, *50*, 11312−11359.

(3) Kim, J.-Y.; Lee, D.; Kim, H. J.; Lim, I.; Lee, W. I.; Jang, D.-J. *J. Mater. Chem. A*, **2013**, *1*, 5982−5988.

(4) Son, M.; Jeong, S.; Jang, D.-J. *J. Phys. Chem. C*, **2014**, *118*, 5961−5967.

(5) Kim, Y.; Kim, H.-B.; Jang, D.-J. *J. Mater. Chem. A*, **2014**, *2*, 5791−5799.

(6) Jun, Y.-W.; Choi, J.-S.; Cheon, J. *Angew. Chem. Int. Ed.* **2006**, *45*, 3414−3439.

(7) Koziej, D.; Lauria, A.; Niederberger, M. *Adv. Mater.* **2014**, *26*, 235–257.

(8) Sang, S.; Zhao, Y.; Burda, C. *Chem. Rev.* **2014**, *114*, 9283−9318.

(9) Wang, H.; Rogach, A. L. *Chem. Mater.* **2014**, *26*, 123−133.

(10) Nikam, A. V.; Arulkashmir, A.; Krishnamoorthy, K.; Kulkarni, A. A.; Prasad, B. L. V. *Cryst. Growth Des.* **2014**, *14*, 4329−4334.

(11) Cargnello, M.; Gordon, T. R.; Murray, C. B. *Chem. Rev.* **2014**, *114*, 9319−9345.

(12) Wang, X.; Li, Z.; Shi, J.; Yu, Y. *Chem. Rev.* **2014**, *114*, 9346−9384.

(13) Fattakhova-Rohlfing, D.; Zaleska, A.; Bein, T. *Chem. Rev.* **2014**, *114*, 9487−9558.

(14) X. Jiang, T. Herricks and Y. Xia, *Adv. Mater.* **2003**, *15*, 1205−1209.

(15) Zhong, L.-S.; Hu, J.-S.; Wan, L.-J.; Song, W.-G. *Chem. Commun.* **2008**, 1184−1186.

(16) Wang, H.-E.; Zheng, L.-X.; Liu, C.-P.; Liu, Y.-K.; Luan, C.-Y.; Cheng, H.; Li, Y. Y.; Martinu, L.; Zapien, J. A.; Bello, I. *J. Phys. Chem. C* **2011**, *115*, 10419−10425.

(17) Das, J.; Freitas, F. S.; Evans, I. R.; Nogueira, A. F.; Khushalani, D. *J. Mater. Chem.* **2010**, *20*, 4425−4431.

(18) Zhao, J.; Zou, X.-X.; Su, J.; Wang, P.-P.; Zhou, L.-J.; Li, G.-D. *Dalton Trans.* **2013**, *42*, 4365−4368.

(19) Tang, Y.; Wee, P.; Lai, Y. Wang, X.; Gong, D.; Kanhere, P. D.; Lim, T.-T.; Dong, Z.; Chen, Z. *J. Phys. Chem. C* **2012**, *116*, 2772−2780.

(20) Wu, W.-Q.; Rao, H.-S.; Xu, Y.-F.; Wang, Y.-F.; Su, C.-Y.; Kuang, D.-B. *Sci. Rep.* **2013**, *3*, 1892.

(21) Zhao, Y.; Zhang, Y.; Liu, H.; Ji, H.; Ma, W.; Chen, C.; Zhu, H.; Zhao, J. *Chem. Mater.* **2014**, *26*, 1014−1018.

(22) Bilecka, I.; Niederberger, M. *Nanoscale* **2010**, *2*, 1358−1374.

(23) Nadagouda, M. N., Speth, T. F. Varma, R. S. *Acc. Chem. Res.* **2011**, *44*, 469−478.

(24) Wilson, G. J.; Will, G. D.; Frost, R. L.; Montgomery, S. A. *J. Mater. Chem.* **2002**, *12*, 1787−1791.

(25) Periyat, P.; Leyland, N.; McCormack, D. E.; Colreavy, J.; Corr, D.; Pillai, S. C. *J. Mater. Chem.* **2010**, *20*, 3650−3655.

(26) Cintas, P.; Tagliapietra, S.; Gaudino, E. C.; Palmisano, G.; Cravotto, G. *Green Chem*. **2014**, *16*, 1056−1065.

(27) Park, J.; Joo, J.; Kwon, S. G.; Jang, Y.; Hyeon, T. *Angew. Chem. Int. Ed.* **2007**, *46*, 4630−4660.

(28) Sowers, K. L.; Swartz, B.; Krauss, T. D. *Chem. Mater.* **2013**, *25*, 1351−1362.

(29) Zhang, W. F.; He, Y. L.; Zhang, M. S.; Yin, Z.; Chen, Q. *J. Phys. D: Appl. Phys.* **2000**, *33*, 912-916.

(30) Wang, D.; Zhao, J.; Chen, B.; Zhu, C. *J. Phys.: Condens. Matter* **2008**, *20*, 085212.

(31) Pillai, S. C.; Periyat, P.; George, R.; McCormack, D. E.; Seery, M. K.; Hayden, H.; Colreavy, J.; Corr, D.; Hinder, S. J. *J. Phys. Chem. C* **2007**, *111*, 1605−1611.

(32) Yang, X.; Fu, H.; Yu, A.; Jiang, X. *J. Colloid Interf. Sci.* **2012**, *387*, 74−83.

(33) Södergren, S.; Siegbahn, H.; Rensmo, H.; Lindström, H.; Hagfeldt, A.; Lindquist, S.-E. *J. Phys. Chem. B* **1997**, *101*, 3087−3090.

(34) Antony, R. P.; Mathews, T.; Dash, S.; Tyagi, A. K. *J. Phys. Chem. C* **2013**, *117*, 6851−6860.

(35) Tao, A. R.; Habas, S.; Yang, P. *Small* **2008**, *4*, 310−325.

(36) Jiang, X.; Wang, Y.; Herricks, T.; Xia, Y. *J. Mater. Chem.* **2004**, *14*, 695−703.

(37) Xiong, L. B.; Li, J. L.; Yang, B.; Yu, Y. *J. Nanomater.* **2012**, *2012*,1−13.

(38) Wang, Y.; Zheng, Y.; Huang, C. Z.; Xia, Y. *J. Am. Chem. Soc.* **2013**, *135*, 1941−1951.

Part 4B. Hierarchical mesoporous anatase TiO_2 nanostructures with efficient photocatalytic and photovoltaic performances

4B. 1. Abstract

Mesoporous anatase TiO_2 nanostructures with diverse morphologies ranging from rod-like 1D nanostructure to diverse hedgehog-like 3D hierarchical nanostructures have been found to have highly efficient photocatalytic and photovoltaic performances. Hierarchical 3D nanostructures have 5.5 times higher photocatalytic activity than rod-like 1D nanostructures, and the DSSC efficiency of hierarchical 3D nanostructures becomes as high as 5.37%, which is 50% higher than the DSSC efficiency of 1D nanostructures. The high photocatalytic performances of the hierarchical 3D anatase TiO_2 nanostructures have been attributed mainly to the large specific pore volume, whereas the high photovoltaic performances of hierarchical 3D nanostructures have been attributed not only to the great specific surface area and the large specific pore volume but also to the interparticular connectivity. Comparative experimental studies have shown that as-prepared hierarchical mesoporous anatase TiO_2 nanostructures have superior photocatalytic (three times higher) and photovoltaic performances (35% higher) compared with commercially available Degussa P25 TiO_2.

---

†This is reproduced from Hyung-Bae Kim Harkjin Kim, Wan In Lee, and Du-Jeon Jang, *J. Mater. Chem. A*, **2015**, *3*, 9714 - 9721.©2015 Royal Society Chemistry

4B. 2. Introduction

With the exponential growth of interest in the field of green energy and environmental sustainability, the conversion of solar energy into electrical or chemical energy has attracted great attention. A photocatalyst can absorb the incoming light, generate excitons, and promote chemical reactions under soft conditions.[1-2] Thus, it has been usefully applied for the photodegradation of organic pollutants,[3,4] the photoreduction of CO_2 to produce hydrocarbon fuel,[5] and the solar water-splitting.[6] Dye-sensitized solar cells (DSSCs) as promising alternatives to conventional silicon-based solar cells have also been studied greatly because of low production cost, facile fabrication processes, and stable photovoltaic properties.[7-10]

Metal oxide semiconductors have been considered to be representative materials for both photocatalysts and working electrodes for DSSCs.[7,8] Titanium dioxide (TiO_2) is the most predominant oxide semiconductor reported in the scientific literatures on photocatalytic and photovoltaic applications. In particular, anatase, which is one of the four polymorphs of TiO_2, has been widely investigated due to its high photoreactivity, chemical stability, favorable band-edge positions, strong optical absorption, and inexpensive cost.[11] There are several reported factors to be considered for the improvement of the photoactivity of anatase TiO_2 crystals; crystalline facets, electronic band structures, shapes, sizes, porosities, and surface areas.[11-13] Thus, extensive efforts have been made to improve the photoactivity of anatase TiO_2

nanostructures by introducing desired factors. In particular, the fabrication of anatase TiO_2 crystals with tailored crystalline facets has been extensively investigated due to their intrinsic facet-dependent photoactivity; both theoretical and experimental studies on the low-index facets of anatase TiO_2 crystals have reported that the {001} facets are much more reactive than the thermodynamically stable {101} facets.[14,15] To make highly efficient photoanodes for DSSCs, ideal TiO_2 particles coated on the working electrode of DSSCs should have a large specific surface area for more dye loading, packed nanostructures for faster electron transfer, and an efficient light-scattering effect for better light harvesting. In addition, an adequate porosity of TiO_2 particles can impose the feasible transport of electrolytes.[11,16] However, it is still challenge to meet those criteria for working electrodes simultaneously in a type of TiO_2 nanostructures. Thus, hierarchical mesoporous anatase TiO_2 3D nanostructures have drawn great attention due to their highly porous structures with high specific surface areas for the sake of the increased adsorption of guest molecules such as pollutants and dyes for DSSCs as well as their efficient light harvesting by excellent internal light-scattering effects.[17-19] In spite of their novel structural advantages, there are few reports about photocatalytic and photovoltaic properties of hierarchical mesoporous TiO_2 nanostructures because the controlled synthesis of hierarchical mesoporous TiO_2 nanostructures remains as a significant challenge. Furthermore, since Park et al. reported the shape-dependent thermodynamic parameters of hierarchical anatase TiO_2 nanostructures,[20] the photocatalytic and photovoltaic

performances of hierarchical TiO_2 nanostructures have hardly been compared with those of 1D TiO_2 nanostructures.

Herein, we report the morphology-dependent photocatalytic and photovoltaic performances of anatase TiO_2 nanostructures. An eco-friendly two-step microwave-assisted synthetic method has been employed to control facilely the diverse morphologies of anatase TiO_2 nanostructures ranging from rod-like 1D nanostructure to hedgehog-like 3D nanostructures. To illuminate structural effects on the photoactivity of hierarchical nanostructures, we have delicately tuned the aspect ratios of 1D building blocks in anatase TiO_2 nanostructures. The aspect-ratio variation of 1D building blocks has led to change the surface areas and pore-volumes of hedgehog-like 3D nanostructures notably. From detailed surface characterization, it has been found that whereas as-prepared rod-like 1D nanostructures consist of single crystalline anatase TiO_2 nanocrystals with dominantly exposed {101} facets, hedgehog-like 3D nanostructures consist of anatase TiO_2 nanocrystals with exposed {001} and {101} facets. The photoactivity experiments have shown that whereas the photocatalytic performances increase mainly with the increase of the specific pore volume, the photovoltaic performances increase with the combination of the high surface area, the great pore volume, and the strong interparticular connectivity. Hedgehog-like 3D nanostructures have 5.5 times higher photocatalytic activity than rod-like 1D nanostructures. When they are employed in the working electrode of DSSCs, the photovoltaic conversion efficiency of DSSC becomes as high as 5.37%, which is 50% higher than the

DSSC efficiency of rod-like 1D nanostructures. In addition, as-prepared anatase TiO_2 nanostructures have superior photocatalytic and photovoltaic activity compared with commercially available Degussa P25 TiO_2.

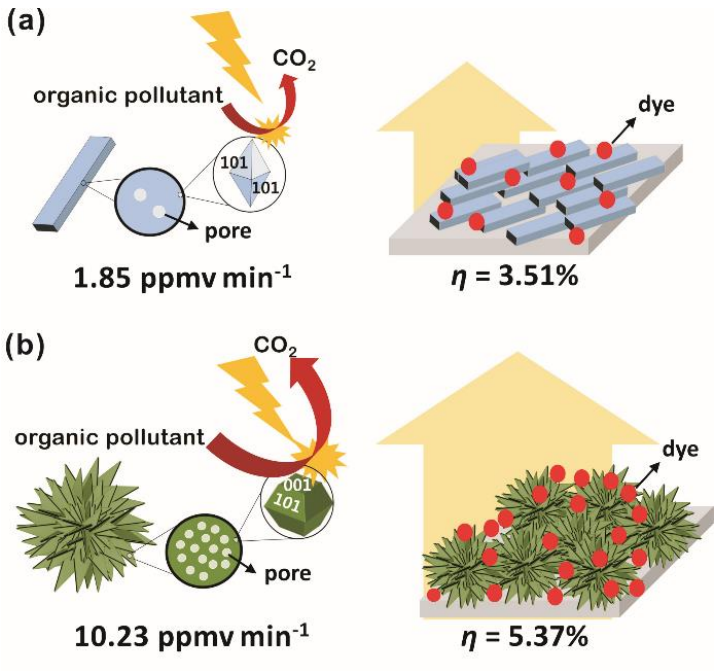

Figure 4B-1. Schematic illustration of morphology-depenedent photocatalytic (left) and photovoltaic performances (right) of as-synthesized rod-like (a) and hedgehog-like anatase TiO_2 crystals (b).

4B. 3. Experimental Details

Materials and preparation

Materials. Titanium(IV) isopropoxide (TIP, l, >97%), glycerol (l, >99%), isopropanol (l, >99.9%), ethanol (l, >99%) were used as purchased from Sigma-

Aldrich. Ultrapure deionized water (>17 MΩ cm) from a Millipore Milli-Q system was used throughout the experiments.

Preparation. Titanium glycerolate crystals were first synthesized as the precursors of anatase TiO_2 nanostructures according to the reported procedure with modification.[21,22] 2.0 mmol of titanium isopropoxide was added to 40 mL of a solvent mixture of isopropanol and glycerol with a certain volume fraction of isopropanol (R). The mixture was maintained at 40 °C under vigorous stirring for 5 min and sonicated in an ultrasonic bath for 5 min to make the solution homogeneously clear. The clear solution was transferred into a 300 mL reactor and irradiated by a Samsung HV-367AWJ microwave system (2.45 GHz, 450 W) for 10 min. The white precipitate was harvested by centrifugation, washed with ethanol and water for three times, and dried at 40 °C. In order to prepare anatase TiO_2 nanostructures, 100 mg of a titanium glycerolate precursor was dispersed in 30 ml of water and subject to microwave irradiation for 10 min. The white precipitate was centrifuged, washed with ethanol and water for three times, and dried at 40 °C. Anatase TiO_2 crystals obtained through the hydrolysis of titanium glycerolate precursors prepared at R values of 0.00, 0.08, 0.20, 0.40, 0.67, and 0.85 will be designated as A00, A08, A20, A40, A67, and A85, respectively.

Characterization and evaluation. While scanning electron microscope (SEM) images were measured with a JEOL JSM-6700F microscope, Fourier transform (FFT) patterns and high-resolution transmission electron microscope (HRTEM) images were measured with a JEOL JEM-3000F microscope. High-resolution

X-ray diffraction (HRXRD) patterns were recorded using a Bruker D8 DISCOVER diffractometer (Cu K_α radiation, $\lambda = 0.154178$ nm), valence-band X-ray photoelectron spectroscopy (XPS) spectra were collected using a Thermo Scientific Sigma Probe ESCA spectrometer (Al Kα X-ray source), and N_2 adsorption-desorption measurements were carried out using a Quantachrome Autosorb AUTOSORB-IQ-MP gas-sorption system.

Photocatalytic oxidation activity. Photocatalytic oxidation efficiencies were estimated by monitoring the amount of CO_2 evolved during the decomposition of isopropanol in the gas phase. An aqueous suspension containing 2.0 mg of a photocatalyst was spread on a 2.5 × 2.5 cm^2 glass as a film and dried at room temperature. The net volume of the gas-tight reactor was 200 mL, and the photocatalyst-coated film was located at the center of the reactor. The entire area of the photocatalytic film was irradiated by a 300 W Xe lamp with a water filter to cut IR off. After the reactor was evacuated, it was injected with 32 μL of 1:9 (v/v) isopropanol and water. The initial concentration of gaseous isopropanol in the reactor was maintained at 117 ppm in volume (ppmv). Thus, the ultimate concentration of CO_2 evolved after the complete oxidation of the injected isopropanol will be 351 ppmv, as shown in the following equation: $2(CH_3)_2CHOH(g) + 9O_2(g) \rightarrow 6CO_2(g) + 8H_2O(g)$. The total pressure of the reactor was then adjusted to 750 mmHg by adding O_2(g). Under this condition, the injected isopropanol and water remained in the vapor phase. After a certain irradiation interval, 0.5 mL of the gas in the reactor was automatically picked up and sent to an Agilent Technologies 6890N gas chromatography (GC) using

an auto-sampling valve system. For CO_2 detection, a methanizer was installed between a GC column outlet and a flame ionization detection (FID) detector.

Photocatalytic reduction activity. Photocatalytic CO_2-reduction efficiencies were evaluated by monitoring CH_3OH evolved in a home-made gas-tight reactor. An aqueous suspension containing 32.0 mg of a photocatalyst was spread on a 5 × 5 cm^2 soda-lime glass in a film form and dried at 50 ^oC for 2 h. The photocatalyst-coated film was placed in the center of the reactor, and its whole area was irradiated through a quartz window. Before measuring the photocatalytic activity, the film was irradiated by a bare 300 W Xe lamp for 30 min to remove organic impurities on the catalytic surface. After a 400 mL gas-tight reactor was evacuated, it was filled with water-saturated CO_2 (g). The IR-filtered light of a 300 W Xe lamp through a water filter was used as the UV-visible light source. The gas mixture in the reactor was magnetically convected during the irradiation. After irradiation for 30 min, 0.5 mL of the gas sample in the reactor was automatically picked up and sent to an Agilent Technologies 7890N GC using an auto-sampling valve system. In order to minimize the re-decomposition of the evolved products, the measurement cycle (chamber evacuation → wet CO_2 gas filling → light irradiation → product detection) was repeated in every 30 min and the amounts of evolved gases in each cycle were summed up. While the evolved $CH_3OH$was detected using an FID detector with an Agilent Technologies DB-1 column, the evolved amounts of CO_2, CO, and O_2 were detected using a thermal conductivity detection (TCD) detector with a Supelco Carboxen-1010 column.

Photovoltaic activity. For the preparation of a working electrode for DSSC, the viscous paste was prepared by the following procedure. 0.4 g of ethyl cellulose, 0.05 g of lauric acid, and 4.5 g of terpineol were added to the ethanol suspension of as-prepared TiO_2 powder and then ethanol was removed from the solution by a rotary evaporator to obtain a viscous paste. The prepared TiO_2 paste was then coated on a bare FTO layer *via* a doctor-blade method. The coated films were baked at 150 ℃ for 30 min and subsequently calcined at 500 ℃ for 15 min. For dye adsorption, the fabricated TiO_2 films were immersed in anhydrous ethanol containing N719 dye and kept for 24 h at room temperature. Pt-coated FTO, used as a counter electrode, was prepared by dropping a 0.7 mM H_2PtCl_6 solution on an FTO glass, followed by heating at 400 ℃ for 20 min in air. The electrolyte consisted of 0.6 M 1-butyl-3-methylimidazolium iodide, 0.03 M I_2, 0.1 M guanidinium thiocyanate, 0.02 M LiI, and 0.5 M 4-tert-butylpyridine in acetonitrile and valeronitrile 85:15 (v/v). The active area of the dye-coated TiO_2 film was 0.420 cm^2. Photocurrent−voltage (I−V) measurements were performed using a Keithley model 2400 source measurement unit. A 300 W Xe lamp was used as the light source, and the light intensity was adjusted approximately to AM 1.5G one sun-light illumination using an NREL-calibrated Si solar cell equipped with a KG-5 filter.

4B. 4. Results and Discussion

The SEM images of Figure 4B-2 show that the morphologies of anatase TiO_2 structures can be controlled successfully from rod-like 1D structures to various hedgehog-like hierarchical 3D structures consisting of 1D building blocks with different aspect ratios *via* a two-step microwave-assisted synthetic process. All the HRXRD patterns of our as-prepared anatase TiO_2 crystals have been found to match well with the reference pattern of the anatase TiO_2 structure. Considering that the peaks of titanium glycerolate crystals are not observed at all in the HRXRD patterns of our as-prepared anatase TiO_2 nanostructures, we suggest that microwave-assisted hydrolysis has completely transformed titanium glycerolate precursors into anatase TiO_2 crystals. It has been also shown in the SEM images of Figure 4B-2 that all the hierarchical anatase TiO_2 structures are the assembly of numerous nanosized 1D building blocks, whose average aspect ratios increase with the increase of the R value (Table 4B-1).

To identify the structural details of their nanosized building blocks, HRTEM images have been measured (Figure 4B-2). Interestingly, HRTEM images have shown that building blocks of anatase TiO_2 nanostructures consist of small interconnected TiO_2 nanocrystals that have resulted from the hydrolysis of titanium glycerolate precursors. Thus, as-prepared anatase TiO_2 nanostructures have great surface roughness to bring about large specific surface areas and high porosities. Fig. S4† confirms that as-prepared anatase TiO_2 nanostructures are constructed by closely interconnected nanocrystals and that the interparticle voids form multiple pores, generating high internal surface areas to adsorb

guest molecules. HRTEM images and FFT patterns indicate that the surface conditions of hedgehog-like 3D anatase TiO_2 nanostructures are significantly different from those of rod-like 1D anatase TiO_2 nanocrystals (Figure 4B-2); although the 1D nanocrystals have thermodynamically stable {101} facets dominantly, the 3D nanostructures have reactive {001} facets as well as {101} facets. Both the HRTEM image and the FFT pattern of A00 display a single d-spacing of 0.35 nm that agrees well with the standard spacing of 0.352 nm between the (101) lattice planes of the anatase TiO_2 crystal lattice of TiO_2 (JPCDS card no. 841286). This indicates that all the anatase TiO_2 crystals of A00 are dominated by {101} facets and that their individual nanocrystals are excellently aligned along the [100] direction.[17] However, each of A20 and A67 reveals interplanar spacings of 0.48 and 0.35 nm together, which are in good accordance with the respective standard spacings of 0.476 and 0.352 nm between the (002) and the (101) planes of the anatase TiO_2 structure. Moreover, the FFT patterns of A20 and A67 show that the angle between the (101) and the (10−1) planes and the angle between the (101) and the (002) planes are 44° and 68°, respectively, which are also in agreement with the respective theoretical angles of 44.5° and 68.3°.[11,23] It has been reported that the order of the average surface energies is {001} (0.90 J m^{-2}) > {010} (0.53 J m^{-2}) > {101} (0.44 J m^{-2}).[14,15] The existence of highly reactive {001} facets in the 3D anatase TiO_2 nanostructures is considered to arise from the temperature-dependent kinetic growth of titanium glycerolate precursors; because our anatase TiO_2 nanocrystals have been produced by the simple hydrolysis of the titanium

glycerolate precursors, the surface properties of anatase TiO_2 have been inherited from the titanium glycerolate precursors. Whereas 1D precursors have been grown at thermodynamic conditions (at high growth temperatures), the 3D precursors have been fabricated under kinetic conditions (at low growth temperatures). Thus, 1D anatase TiO_2 nanostructures have thermodynamically stable {101} facets mainly, and 3D anatase TiO_2 nanostructures have reactive {002} and {004} facets as well as {101} facets. It was not possible to calculate the accurate fractions of the respective exposed facets in individual anatase TiO_2 nanostructures due to their irregular shapes.

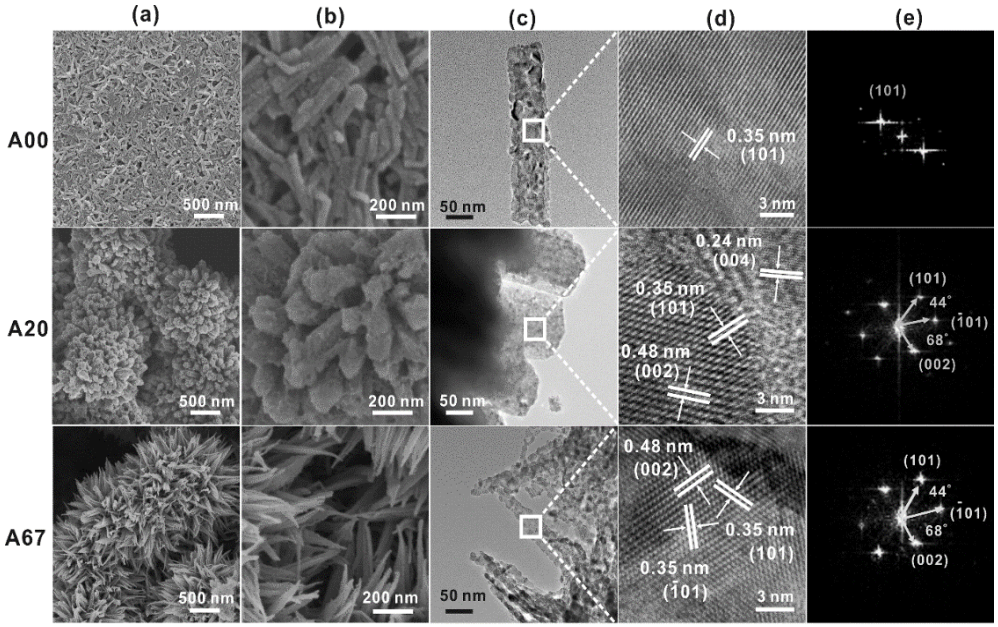

Figure 4B-2. SEM images (a,b), HRTEM images (c,d), and FFT patterns (e) of anatase TiO_2 nanostructures A00, A20, and A67.

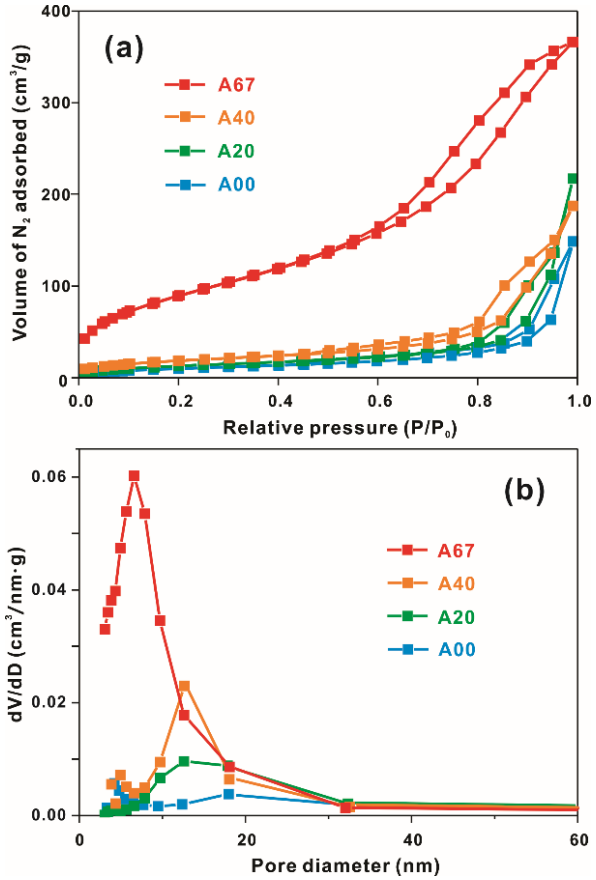

Figure 4B-3 N_2 adsorption-desorption isotherms (a) and pore-size distributions (b) of indicated anatase TiO_2 crystals.

In general, because the photocatalysis and the electron transfer of DSSC are surface-based processes, it is important to investigate surface conditions of fabricated crystals. Thus, we have measured the N_2 adsorption-desorption isotherms of as-prepared TiO_2 nanostructures (Figure 4B-3). It can be seen that all our samples show type-IV isotherms with type-H3 hysteresis loops according to the IUPAC classification, indicating that our samples have mesoporous structures.[25-27] All the 3D hierarchical anatase TiO_2 nanostructures

have higher values of specific surface areas than the 1D anatase TiO_2 nanostructures. The specific pore volumes and the pore sizes as well as the specific surface areas of 3D nanostructures depend strongly on the aspect ratios of their building blocks. As the average aspect ratio of the building blocks of 3D nanostructures increases, the hysteresis loop shifts toward a lower relative pressure and the area of the hysteresis loop increases, indicating that the specific surface area increases with the increase of the R value. Also, the peak of pore-size distribution shifts toward a smaller pore diameter and the area of the distribution increases with the increase of the aspect ratio, indicating that the pore size decreases while the pore volume increases with the increase of the R value. The fact that the pore volume of 3D nanostructures is larger than that of 1D nanostructures can be attributed to the nature of hierarchical structures.[28] Taking into consideration together, we assert that our microwave-assisted fabrication method can successfully control the morphologies as well as the surface conditions of anatase TiO_2 nanostructures.

Anatase TiO_2 crystals exposed with dissimilar crystal facets are known to exhibit different electronic band structures because each facet has its own unique surface atomic arrangement.[14,15,28] Because the electronic band structure is considered to be a very important factor to affect the photoreactivity of anatase TiO_2 crystals, we have deduced the electronic-band gap alignments of as-prepared anatase TiO_2 crystals by combining UV-visible diffuse-reflectance spectra and valence-band XPS spectra (Figure 4B-4). The UV-visible diffuse reflectance spectra of Fig. 4a show that the absorption edges of A20 and A67

are red-shifted by 6 nm with respect to that of A00. It is well known that anatase TiO_2 is an indirect semiconductor, whose bandgap can be estimated by extrapolating the linear portion of the modified Kubelka–Munk function versus the energy of light (Figure 4B-4b). The derived band gaps of A00, A20, and A67 are 3.10, 3.07, and 3.07 eV, respectively. On the other hand, the valence-band XPS spectra of Fig. 4c reveal that all our anatase TiO_2 crystals have the valence-band maxima at the same value of 1.97 eV. Thus, the conduction band minimum of A00 is raised by 0.03 with respect to those of A20 and A67; the order of the potential of the conduction-band potential minima is A00 > A20 = A67 (Figure 4B-4d). It is reported that whereas the energy of the {001} surface is higher than that of the {101} surface, the conduction-band minimum of the {001} surface is lower than that of the {101} surface.[29]

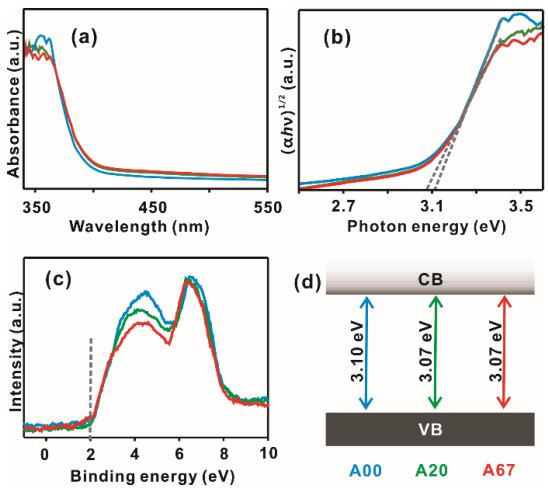

Figure 4B-4. UV-visible diffuse reflectance spectra (a), Kubelka-Munk plots of the reflectance spectra to find indirect band-gap energies (b), valence-band XPS spectra (c),

and determined valence-band (VB) and conduction-band (CB) edges (d) for A00 (red), A20 (green), and A67 (blue).

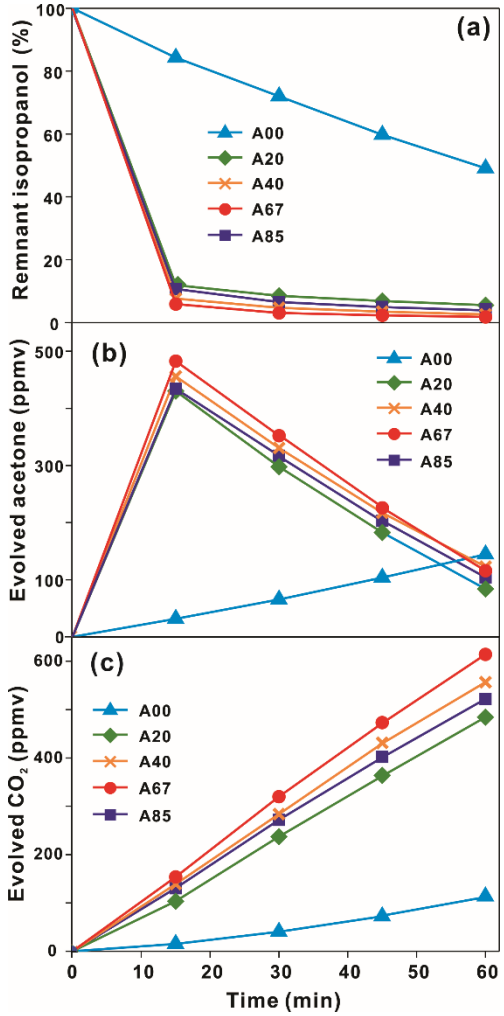

Figure 4B-5. Photocatalytic oxidation curves of isopropanol *via* indicated anatase TiO_2 crystals under UV-visible irradiation for remnant isopropanol (a), evolved acetone (b), and evolved CO_2 (c) as a function of irradiation time.

The photocatalytic oxidation activity of as-synthesized anatase TiO_2 nanostructures was evaluated by oxidizing gaseous isopropanol under UV-visible irradiation (Figure 4B-5). Gaseous isopropanol is initially oxidized to

generate acetone as an intermediate, and is ultimately converted into carbon dioxide and water.[30,31] Thus, the amounts of remnant isopropanol, evolved acetone, and evolved CO_2 have been monitored as a function of irradiation time to determine the photoactivity of each sample of anatase TiO_2 nanostructures. As shown in Fig. 5, the photocatalytic activities of hedgehog-like 3D nanostructures are much more efficient than that of rod-like 1D nanostructures. It can be also observed that the photocatalytic activity of 3D TiO_2 nanostructures increases gradually as the average aspect ratio of building blocks increases. As the average aspect ratio of building blocks increases, both the specific surface area and the specific pore volume, as well as the exposure of the reactive {001} facets, increase. However, the close examination of Table 4B-1 reveals that the photocatalytic oxidation activity of TiO_2 nanostructures depends particularly on the specific pore volume of TiO_2 nanostructures. This suggests that the heterogeneous photocatalytic oxidation reaction of gaseous isopropanol takes place inside the nanopores of anatase TiO_2 nanostructures. Mahmoud et al. have reported the nanoreactor confinement effect that catalytic reactions occurring on the external surface of a solid nanoparticle are contrasted with those occurring on the nanocavity of a nanostructure, which reduces the activation energy extensively.[3,32] Thus, we consider that the morphology of hierarchical anatase TiO_2 nanostructures having a large specific pore volume is responsible for their efficient photocatalytic oxidation performances.

The photocatalytic reduction of CO_2 with H_2O has been well known to produce CH_4 and CH_3OH as the main products.[33,34] Thus, the amount of evolved

CH_3OH, which was selectively produced in our photoreactor, was monitored to evaluate the structural advantage of our photocatalyst under UV-visible irradiation. Figure 4B-6 show that the evolved amount of CH_3OH *via* anatase TiO_2 A67 is 3.1 times higher than that *via* commercial photocatalyst Degussa P25 TiO_2. Because Degussa P25 is known to have a specific surface area of 51.4 m^2/g and a specific pore volume of 0.17 m^3/g,[24,35] it is suggested that the enhancement of the photocatalytic reduction activity of anatase TiO_2 A67 also arises from the increase of the specific pore volume of anatase TiO_2 A67. Thus, we assert that the photocatalytic reduction of CO_2, as well as the photocatalytic oxidation of isopropanol, *via* TiO_2 nanostructures occurs inside their nanocavities. The very efficient photocatalytic oxidation and reduction performances of our hierarchical mesoporous anatase TiO_2 nanostructures are considered to result from their extremely large specific pore volumes.

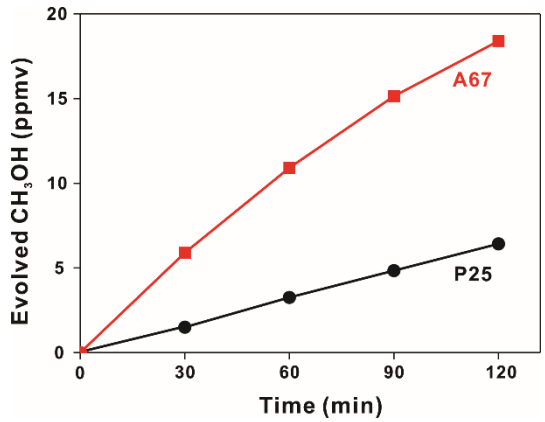

Figure 4B-6. Photocatalytic reduction curves of CO_2 by using anatase TiO_2 crystals A67 and commercial TiO_2 Degussa P25 under UV-visible irradiation.

To evaluate the photovoltaic performances of as-synthesized TiO_2 nanostructures, our samples have been applied as working electrodes having a film thickness of 10 μm for DSSCs. The current density-voltage (J-V) curves of Fig. 7 and the photovoltaic operation parameters of Table 4B-2 indicate that our as-prepared TiO_2 nanostructures perform well as the working electrode of DSSCs with and without a light-shading mask. The photovoltaic parameters of DSSCs in Tables 4B-2 reveal that the power conversion efficiency (η) of anatase TiO_2 nanostructures increases gradually as the R value increases; the largest power conversion efficiency has been observed with anatase TiO_2 A67, which has the largest specific surface area and the highest specific pore volume among our as-prepared anatase TiO_2 crystals. It is well known that mesoporous anatase TiO_2 structures can facilitate the transport of the redox couple of electrolytes.[16-19] Therefore, the highest DSSC efficiency of A67 can be explained by two factors. First, the increased light-harvesting efficiency can be enhanced by the intense internal light-scattering effect, which results from interactions between TiO_2 and dye molecules owing to the greatest specific surface area as well as the largest specific pore volume. Second, the rapid charge transport through the photoanode film made of mesoporous TiO_2 nanostructures owing to the better interparticular connectivity can also improve the DSSC efficiency of A67 substantially For these reasons, the DSSC efficiency of anatase TiO_2 nanostructures A67 is 35% higher than that of commercially available TiO_2 Degussa P25 (Table 4B-1).

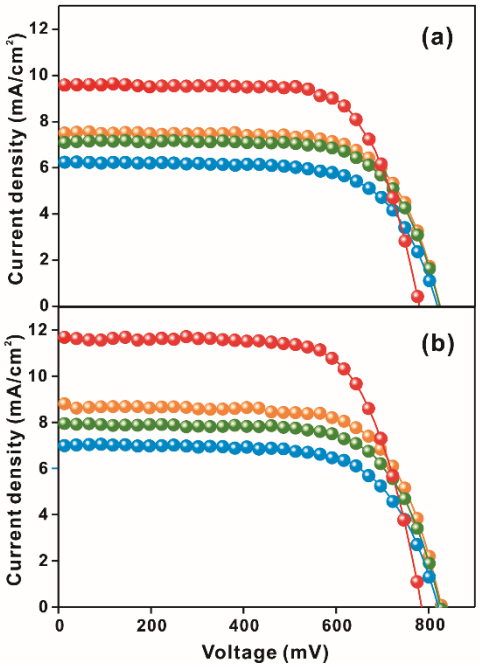

Figure 4B-7 $J-V$ curves of DSSCs based on as-synthesized anatase TiO_2 crystals A00 (red), A20 (green), A40 (orange), and A67 (blue) with (a) and without (b) a light-shading mask.

The photocatalytic and photovoltaic performances of our anatase TiO_2 nanostructures have been illustrated. Although both performances depend on the morphology and the surface conditions of TiO_2 crystals, their dependent behaviors are quite different from each other. As described already, whereas the photocatalytic performances increase mostly depending on the increase of the specific pore volume, the photovoltaic performances increase not only with the specific surface area and the specific pore volume, which enhance the light-harvesting ability, but also with the interparticular connectivity, which improves the charge transport. Overall, it has been shown that the morphology as well as the surface conditions of our hierarchical mesoporous anatase TiO_2 nanostructures is highly beneficial to efficient photocatalytic and photovoltaic performances.

4B. 5. Conclusion

Mesoporous anatase TiO_2 nanostructures with diverse morphologies ranging from rod-like 1D nanostructure to hedgehog-like 3D hierarchical nanostructures have been prepared to investigate their photocatalytic and photovoltaic performances. Hierarchical 3D nanostructures have 5.5 times higher photocatalytic activity than rod-like 1D nanostructures, and the DSSC efficiency of hierarchical 3D nanostructures becomes as high as 5.37%, which is 50% higher than the DSSC efficiency of 1D nanostructures. The high photocatalytic performances of the hierarchical 3D anatase TiO_2 nanostructures are attributed mainly to the large specific pore volume because mesoporous nanocavities can decrease the activation energy of photocatalytic reactions. On the other hand, the high photovoltaic performances of hierarchical 3D nanostructures have been attributed not only to the great specific surface area and the large specific pore volume, which enhance the light-harvesting ability by increasing dye adsorption and internal light-scattering effect, but also to the interparticular connectivity, which improves the charge transport within working electrodes for DSSCs. Comparative experimental studies have shown that as-prepared hierarchical mesoporous anatase TiO_2 nanostructures have superior photocatalytic (three times higher) and photovoltaic performances (35% higher) compared with commercially available Degussa P25 TiO_2. Thus, our results are suggested to contribute considerably to the development of new

strategies for the improvement of the photocatalytic and photovoltaic performances of anatase TiO_2 nanostructures.

4B. 7. References

(1) H. Zhou, Y. Qu, T. Zeid and X. Duan, *Energy Environ. Sci.*, 2012, **5**, 6732.

(2) F. Fresno, R. Portela, S. Suarez and J. M. Coronado, *J. Mater. Chem. A*, 2014, **2**, 2863.

(3) Y. Kim, H.-B. Kim and D.-J. Jang, *J. Mater. Chem. A*, 2014, **2**, 5791.

(4) J.-Y. Kim, D. Lee, H. J. Kim, I. Lim, W. I. Lee, D.-J. Jang, *J. Mater. Chem. A*, 2013, **1**, 5982.

(5) L. Liu, H. Zhao, J. M. Andino and Y. Li, *ACS Catal.*, 2012, **2**, 1817.

(6) T. K. Townsend, N. D. Browning and F. E. Osterloh, *ACS Nano*, 2012, **6**, 7420.

(7) M. Grätzel, *Acc. Chem. Res.*, 2009, **42**, 1788.

(8) A. Hagfeldt, G. Boschloo, L. Sun, L. Kloo and H. Pettersson, *Chem. Rev.*, 2010, **110**, 6595.

(9) Y. J. Kim, M. H. Lee, H. J. Kim, G. Lim, Y. S. Choi, N.-G. Park, K. Kim and

(10) Lee, *Adv. Mater.*, 2009, **21**, 3668.

(11) I. G. Yu, Y. J. Kim, H. J. Kim, C. Lee and W. I. Lee *J. Mater. Chem.*, 2011, **21**, 532.

(12) M. Cargnello, T. R. Gordon, C. B. Murray, *Chem. Rev.*, 2014, **114**, 9319.

(13) D. Fattakhova-Rohlfing, A. Zaleska, T. Bein, *Chem. Rev.*, 2014, **114**, 9487.

(14) X. Wang, Z. Li, J. Shi, Y. Yu, *Chem. Rev.*, 2014, **114**, 9346.

(15) X. Q. Gong, and A. Selloni, *J. Phys. Chem. B*, 2005, **109**, 19560.

(16) Y. Wang, H. Sun, S. Tan, H. Feng, Z. Cheng, J. Zhao, A. Zhao, B. Wang, Y. Luo, J. Yang and J. G. Hou, *Nat. Commun.*, 2013, **4**, 2214.

(17) X. Miao, K. Pan, Y. Liao, W. Zhou, Q. Pan, G. Tian and G. Wang, *J. Mater. Chem. A*, 2013, **1**, 9853.

(18) H.-E. Wang, L.-X. Zheng, C.-P. Liu, Y.-K. Liu, C.-Y. Luan, H. Cheng, Y. Y. Li, L. Martinu, J. A. Zapien, and I. Bello, *J. Phys. Chem. C*, 2011, **115**, 10419.

(19) W.-Q. Wu, H.-S. Rao, Y.-F. Xu, Y.-F. Wang, C.-Y. Su and D.-B. Kuang, *Sci. Rep.*, 2013, **3**, 1352.

(20) J. Lin, A. Nattestad, H. Yu, Y. Bai, L. Wang, S. X. Dou and J. H. Kim, *J. Mater. Chem. A*, 2014, **2**, 8902.

(21) T.-J. Park, A. A. Levchenko, H. Zhou, S. S. Wong and A. Navrotsky, *J. Mater. Chem.*, 2010, **20**, 8639.

(22) J. Das, F. S. Freitas, I. R. Evans, A. F. Nogueira, D. Khushalani, *J. Mater. Chem.*, 2010, **20**, 4425.

(23) J. Zhao, X.-X. Zou, J. Su, P.-P. Wang, L.-J. Zhou, G.-D. Li, *Dalton Trans.*, 2013, **42**, 4365.

(24) L. Ye, J. Mao,J. Liu, Z. Jiang, T. Peng and L. Zan, *J. Mater. Chem. A*, 2013, **1**, 10532.

(25) S. Bakardjievaa, J. Šubrta, V. Štengl, M. J. Dianez, M. J. Sayagues, *Appl. Catal. B: Eviron.* 2005, **58**, 193.

(26) Y. Tang, P. Wee, Y. Lai, X. Wang, D. Gong, P. D. Kanhere, T.-T. Lim, Z. Dong, Z. Chen, *J. Phys. Chem. C*, 2012, **116**, 2772.

(27) J. S. Chen, Y. L. Tan, C. M. Li, Y. L. Cheah, D. Luan, S. Madhavi, F. Y. C. Boey, L. A. Archer and X. W. Lou, *J. Am. Chem. Soc.*, 2010, **132**, 6124.

(28) M. Kruk, M. Jaroniec, *Chem. Mater.*, 2001, **13**, 3169.

(29) H. Wang, A. L. Rogach, *Chem. Mater.*, 2014, **26**, 123.

(30 J. Pan, G. Liu, G. Q. Lu and H.-M. Cheng, *Angew. Chem. Int. Ed*., 2011, **50**, 2133.

(31) C. Barakat, P. Gravejat, O. Guaitella, F. Thevenet, A. Rousseau, *Appl. Catal. B: Eviron.*, 2014, **147**, 302.

(32) S. B. Rawal, S. Bera, D. Lee, D. -J. Jang and W. I. Lee, *Catal. Sci. Technol.*,

2013, **3**, 1822.

(33) M. A. Mahoud, F. Saira and M. A. El-Sayed, *Nano Lett.*, 2010, **10**, 3764.

(34) J. Mao, K. Li and T. Peng, *Catal. Sci. Technol.*, 2013, **3**, 2481.

(35) E. Liu, L. Kang, F. Wu, T. Sun, X. Hu, Y. Yang, H. Liu, J. Fan, *Plasmonics*, 2014, **9**, 61.

(36) S. Agarwala, M. Kevin, A. S. W. Wong, C. K. N. Peh, V. Thavasi and G. W. Ho, *ACS Appl. Mater. Interfaces*, 2010, **2**, 1844

Chapter 5. Morphology-Tunable Synthesis of ZnO Microstructures under Microwave Irradiation: Formation Mechanisms and Photocatalytic Activity

[†]This is reproduced from Hyung-Bae Kim, Dong-Won Jeong and Du-Jeon Jang, *CrystEngComm*, **2016,** (DOI: 10.1039/C5CE02334C. © 2016 Royal Society Chemistry

5. 1. Abstract

The morphologies and the surface conditions of ZnO microstructures have been controlled facilely *via* a microwave-assisted one-pot synthetic route by varying the ammonia concentration of the reaction mixture. Ammonia affects the nucleation, growth, and hydrolysis kinetics of intermediate zinc glycerolate to induce shape variation from flower-like ZnO microstructures to various ZnO twin microstructures with the preferred exposure of ±(0001) polar planes. As-prepared ZnO microstructures are mesoporous with large specific surface areas and high specific pore volumes, which have resulted from the microwave-assisted fast hydrolysis of intermediate zinc glycerolate microstructures. Owing to the novel features of microwave, ZnO microstructures have numerous microcracks and wrinkles on their surfaces and show characteristic defect-driven orange emission, whose intensity increases with the specific surface area. The photocatalytic degradation rate constant of rhodamine B *via* our prepared ZnO microstructures have been founded to increase linearly with the specific surface area, the specific pore volume, and the polar-surface exposure. Our simple and rapid microwave-assisted synthetic method is considered to be beneficial to the development of morphology-controlled metal oxides that are applicable for eco-friendly waste-water treatment.

5. 2. Introduction

The development of the facile and morphology-tunable synthetic methods of nanostructures with functional properties has attracted great attention in nanotechnology.[1-5] Particularly, the fabrication of metal oxide nanostructures having various morphologies has been extensively explored owing to their chemical and thermal stability.[4-6] Zinc oxide (ZnO), which is a representative metal oxide semiconductor, has been reported to have a direct wide-band gap (3.37 eV), a large exciton-binding energy (60 meV), a large piezoelectric constant, and a high electron mobility.[7-9] These features have been extended in their wide applications such as UV lasers,[10] light-emitting diodes, photocatalysts,[11] UV or gas sensors,[12-13] and piezoelectric or photoelectric devices.[13-14] Since the properties of ZnO nanostructures depend strongly on morphologies, extensive efforts have been devoted to control their sizes, shapes, and facets delicately.[15-18]

Understanding and manipulating crystal growth mechanisms are keys to design the morphologies of nanomaterials. In general, the most useful strategy to control the morphologies of ZnO structures is the introduction of additives such as surfactants or ions in aqueous media, which affect kinetic and thermodynamic parameters significantly during nucleation and growth processes.[11] However, it is challenging to fabricate the morphology-controlled ZnO microstructures *via* the conventional methods due to the high reactivity of zinc precursors in aqueous media. Unlike conventional synthetic methods, novel two-step approaches for the preparation of ZnO nanostructures using zinc

polyolate complexes (ZPCs) as precursors have been also reported.[14-21] ZPC nanostructures are stable against moisture, so that we can control their morphologies rather easily. The subsequent calcination or hydrolysis process can transform ZPC nanostructures into ZnO ones. In most cases, the intrinsic morphologies of ZPCs have been preserved after conversion into ZnO. Consequently, with the assistance of ZPCs, ZnO nanostructures can have the novel morphologies that cannot be realized by the conventional aqueous synthetic conditions. Thus, ZPC nanostructures can be employed usefully as shape-determining sacrificial templates for the preparation of ZnO nanostructures having novel morphologies. However, there are three major challenging problems in ZPC-based synthetic methods. Most of the reported methods often require a too long reaction time of 10-24 h. Also, an additional post-calcination process at a high temperature of 400-600 ℃ is necessarily required to transfrom ZPCs into the desired crystalline ZnO phase. Finally, two-step ZPC-based synthetic methods are inconvinient in comparison with conventional one-step methods. Consequently, those challenging features have limited the economical applications of ZPC-based ZnO syntheses.

Microwave dielectric heating, which is significantly different from conventional heating sources, has been used to solve problems of time-consuming inorganic synthetic processes. Microwave can raise the reaction temperature uniformly and quickly throughout the whole liquid volume beacause it can penetrate the reactor wall easily, and it can also excite molecules or ions selectively due to the difference in the dielectric constants of reactants.[13]

The thermal and kinetic features of microwave superheating not only reduce the reaction time by several orders of magnitude but also suppress side reactions substantially. Microwave dielectric heating often causes unique outcomes that cannot be achieved or duplicated by conventional heating.[12-14] Thus, microwave can be used to accelerate the reaction rate and to induce unique properties in inorganic nanostructures. In general, polyol solvents such as ethylene glycol and glycerol have been efficiently used in microwave dielectric heating because they have great ability to convert microwave energy into heat at a given frequency of 2.45 GHz. Therefore, ZPC-based synthetic methods can be used usefully to prepare ZnO nanostructures under microwave irradiation. Despite those substantial advantages, however, the microwave-assisted preparation of ZnO structures using ZPCs has been rarely reported.

In this work, we have developed a microwave-assisted one-pot synthetic strategy for the preparation of the morphology-controlled ZnO microstructures *via* forming zinc glycerolate ($C_3H_6O_3Zn$) as a ZPC intermediate within 10 min. We have tuned ZnO microstructures simply by adjusting the concentration of ammonia, which can control not only the nucleation and growth kinetics but also the hydrolysis kinetics of zinc glycerolate intermediate. The differences in the growth kinetics have altered the growth orientation and have induced morphological variation from flower-like microstructures to diverse twin microstructures. Using prepared ZnO microstructures, we have also performed photocatalytic waste-water treatment, understanding the photocatalytic activity of ZnO microstructures is morphology-dependent. Our report will devote

considerably to the development of simple microwave-assisted synthetic strategies for morphology-controlled metal oxide microstructures, and also contribute to understanding the morphology-dependent properties related to the fields of energy storage, conversion, and sustainability.

5. 3. Experimental Details

Materials and preparation

Microwave-assisted preparation of ZnO microstructures. ZnO microstructures having various morphologies were fabricated according to reported procedures[18-20] with modification. 1.0 mmol of zinc acetate dihydrate(s) was put into 30 mL of glycerol and 15 mL of water, and the mixture was sonicated in an ultrasonic bath for 10 min. Then, 2.0 mL of 0.0, 0.40, 1.0, 2.0, 4.0, or 6.0 M ammonia(aq) was added into the above mixture under vigorous stirring. Note that the concentration of ammonia in the reaction mixture was 0.0, 17, 43, 85, 170, or 260 mM. The above solution was transferred into a 300 mL reactor and irradiated by a Samsung HV-367AWJ microwave system (2.45 GHz, 450 W) for 10 min. The white precipitate was harvested by centrifugation, washed with ethanol and water for three times, and dried at 60 ^{o}C for further usage.

Characterization and photocatalytic evaluation

General. While the morphologies of the samples were measured with a JEOL JSM-6700F scanning electron microscope (SEM), fast Fourier transform (FFT) patterns and high-resolution transmission electron microscope (HRTEM) images were measured with a JEOL JEM-3010 microscope. Dynamic light scattering for size evaluation was measured using a Malvern Instruments Zetasizer 3500 equipped with a He−Ne ion laser emitting at 632.8 nm. High resolution X-ray diffraction (HRXRD) patterns were recorded with a Bruker D8 DISCOVER diffractometer using Cu K_α radiation (λ = 0.154178 nm). N_2 adsorption-desorption measurements were carried out using a Quantachrome Autosorb AUTOSORB-IQ-MP gas-sorption system. Fourier transform infrared (FTIR) spectra were obtained using a Nicolet 6700 FTIR spectrometer. X-ray photoelectron spectroscopy (XPS) spectra were collected using a Thermo Scientific Sigma Probe ESCA spectrometer with an Al K_α X-ray source, and their measured binding energies were calibrated with the C 1s peak at 284.6 eV of contaminated carbon. UV-visible extinction spectra were monitored using a Scinco S-3100 spectrophotometer, and photoluminescence spectra were obtained using a home-built fluorometer consisting of an Acton Research XS432 Xe lamp of 75 W equipped with an Acton Research Spectrapro-150 monochromator of 0.15 m and an Acton Research PD438 photomultiplier tube attached to an Acton Research Spectropro-300 monochromator of 0.30 m.

Photocatalytic activity. The photocatalytic performances of as-prepared samples was evaluated at ambient conditions with rhodamine B as a representative dye. In a typical procedure, 10 mg of as-prepared ZnO

microstructures was added to 30 mL of 10 μM rhodamine B(aq) and stirred in the dark for 30 min to ensure the adsorption-desorption equilibrium of rhodamine B on the surfaces of the ZnO catalyst. The reaction mixture was placed 30 cm away from a 300 W Schoeffel LPS 255 HR xenon arc lamp, and its aliquot was taken at every scheduled interval time of 10 min during irradiation and centrifuged to separate the supernatant, and then the UV-visible absorption spectrum of the supernatant was recorded to monitor the remnant of rhodamine B.

5. 4. Results and Discussion

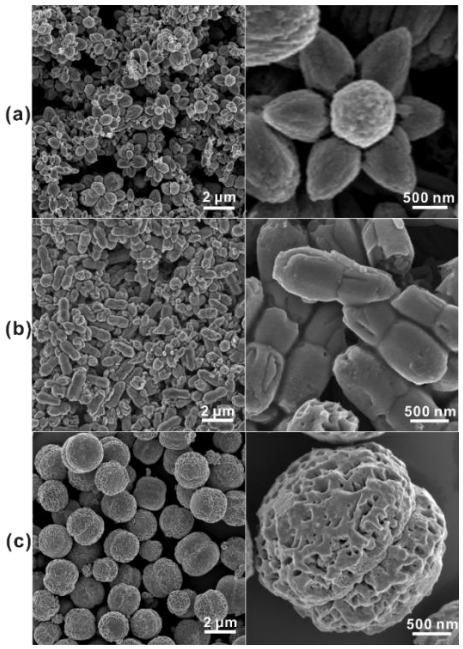

Figure 5-1 SEM images of ZnO microstructures having various morphologies prepared at different ammonia concentrations of (a) 0.0 mM, (b) 43 mM, and (c) 170 mM.

For the one-pot fabrication of ZnO microstructures *via* a ZPC-based synthetic route, we have employed co-solvents of glycerol and water as the reaction medium, where both the formation and the hydrolysis of zinc glycerolate occur sequentially. In addition, for the fabrication of morphology-controlled ZnO microstructures, we have also changed the concentration of ammonia in our reaction medium delicately. As shown in the SEM images of Figure 5-1, the morphologies of ZnO microstructures have been controlled successfully *via* a microwave-assisted synthetic route with variation of the ammonia concentration in the reaction medium; whereas flower-like ZnO microstructures have been obtained in the absence of ammonia (Figure 5-1a), various ZnO twin microstructures have been prepared in the presence of ammonia (Figure 5-1b,c). Flower-like ZnO microstructures have been assembled with irregular submicrostructures ranging from 0.5 μm to 1.2 μm. Peanut-like ZnO microstructures, which have been fabricated at an optimal ammonia concentration of 43 mM, have unique twin structures with an average length of 1.6 μm. Burger-like ZnO microstructures, which have been synthesized optimally at 170 mM of ammonia, appear to have twin structures with an average diameter of 2.1 μm, whose rough surfaces result from microcracks. It is noteworthy that ZnO microstructures prepared at a high ammonia concentration of 260 mM have collapsed burger-like twin structures.

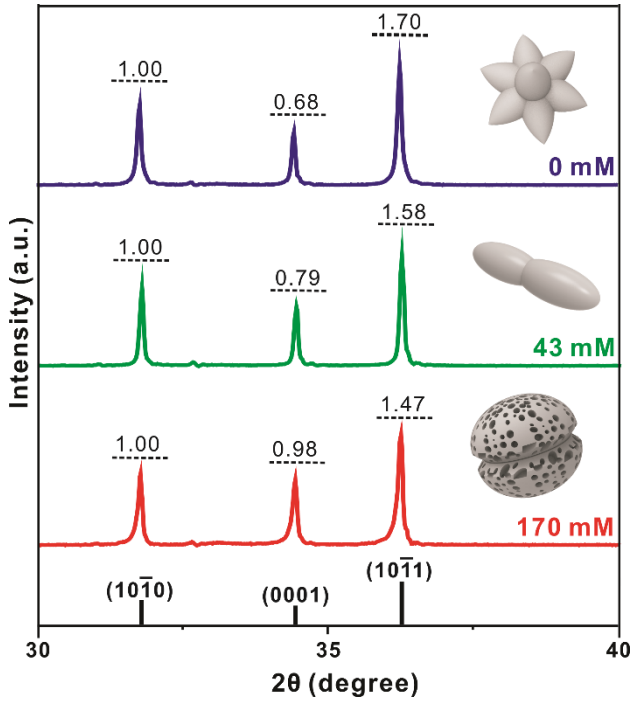

Figure 5-2 HRXRD patterns of ZnO microstructures having various morphologies prepared at indicated ammonia concentrations. The relative maximum intensity of each peak is shown on a dashed line, and the standard diffraction pattern of hexagonal wurtzite ZnO is also shown in the bottom.

Figure 5-2 shows that all the HRXRD patterns of as-prepared ZnO microstructures match well with the reference pattern of the hexagonal wurtzite ZnO phase (JCPDS Card no. 36-1451). Considering that HRXRD peaks from zinc glycerolate have not been detected at all in the HRXRD patterns of ZnO microstructures, we suggest that morphology-controlled ZnO microstructures have been successfully prepared within 10 min *via* our microwave-assisted one-pot synthetic method. In addition, the sharp and intensive HRXRD peaks indicate that ZnO microstructures have highly crystalline structures. Thus, it is suggested that our microwave-assisted synthetic method is economically

efficient in comparison with conventional time-consuming synthetic methods.[13-17] Three characteristic $(10\bar{1}0)$, (0001), and $(10\bar{1}1)$ peaks in Figure 5-2 show that there are noticeable intensity changes in the diffraction of $(10\bar{1}0)$, (0001), and $(10\bar{1}1)$ planes, indicating that the amount of ammonia has influenced vitally on the growth orientation of ZnO microstructures. Whereas the relative intensity of the (0001) plane is enhanced, the relative intensity of the $(10\bar{1}1)$ plane decreases with the increase of the ammonia concentration. These also suggest that the exposure of (0001) planes in ZnO microstructures is promoted while the exposure of $(10\bar{1}0)$ and $(10\bar{1}1)$ planes is inhibited by the presence of ammonia. Considering the fact that ±(0001) polar surfaces are energetically unfavourable due to their intrinsically high surface energies, we suggest that ammonia has kinetically controlled the morphology of ZnO microstructures to expose (0001) planes preferentially. Thus, the alteration of ZnO growth orientation *via* ammonia has resulted in the morphological variation of ZnO microstructures from flower-like microstructures to burger-like twin microstructures.

To understand structural details, we have taken HRTEM images at the edges of the ZnO microstructures, as presented in Figure 5-3. The discernible lattice-fringe images and the clear FFT diffraction spots of Figure 5-3b,c indicate that prepared ZnO microstructures are highly crystalline. The lattice analysis of HRTEM images and FFT patterns indicates that both flower-like and burger-like ZnO microstructures have interplanar spacings of 0.28 nm, which are in good accordance with the standard d-spacing of the $(10\bar{1}0)$ planes

of the hexagonal wurtzite ZnO structure. The preferred growth direction along [10$\bar{1}$0] leads to the formation of ZnO microstructures with exposed ±(0001) polar planes. However, it is still challenging to calculate the accurate fraction of the (0001) polar planes in the overall crystallites of ZnO microstructures using HRTEM images.

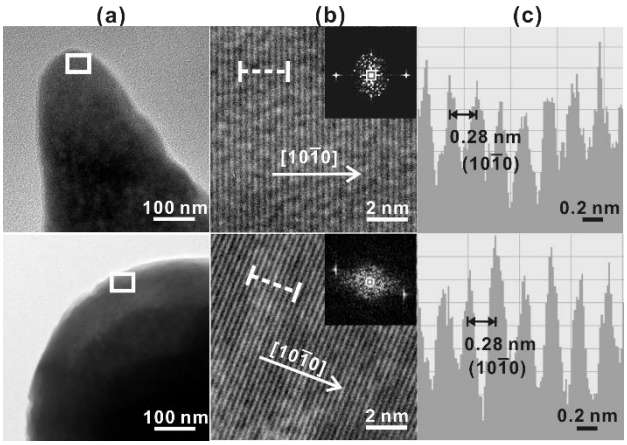

Figure 5-3 (a) TEM images, (b) HRTEM images observed from the indicated square regions of the TEM images, and (c) atomic density profiles scanned along dashed lines in the HRTEM images of (top) flower-like and (bottom) burger-like ZnO microstructures. The insets show FFT patterns.

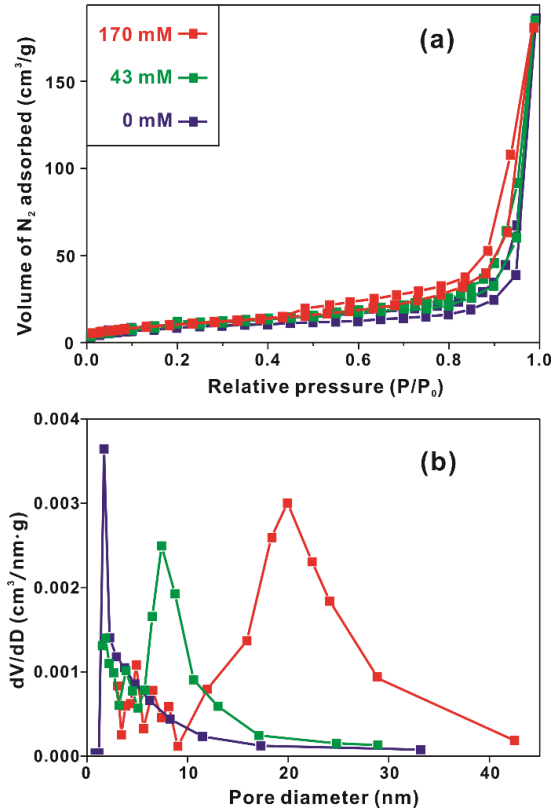

Figure 5-4. (a) N_2 adsorption-desorption isotherms and (b) pore-size distributions of ZnO microstructures prepared at indicated ammonia concentrations.

To evaluate the surface conditions of our prepared ZnO microstructures, we have measured their N_2 adsorption-desorption isotherms (Figure 5-4). All the obtained isotherms show type-IV behaviors with H3 hysteresis loops according to the IUPAC classification, designating apparently that our prepared ZnO microstructures are mesoporous.[25] The specific surface areas, pore sizes, and pore volumes of our prepared ZnO microstructures have been found to increase as the ammonia concentration in the reaction medium increases (Table 5-1). It is noticeable that all the measured specific surface areas of our prepared ZnO

microstructures (32.1 m^2/g - 45.0 m^2/g) are significantly higher than those of reported ZnO microstructures with similar sizes (3 m^2/g - 27 m^2/g).[35-38] These results are attributed to the fact that our hexagonal wurtzite ZnO microstructures are fabricated *via* the hydrolysis process instead of the conventional calcination process. In general, during the hydrolysis process, internal voids, which enhance surface areas considerably, are generated naturally because water can penetrate throughout the deep regions of intermediate zinc glycerolate microstructures. It is noteworthy that burger-like ZnO microstructures have exclusively high values of pore sizes and pore volumes due to the microcracks and wrinkles on their surfaces. Considering the fact that microwave-free conventional fabrication with similar initial conditions does not generate microcracks and wrinkles sufficiently, we suggest that the rich formation of microcracks and wrinkles can also be attributed to the novel features of microwave dielectric heating because microwave accelerates the hydrolysis of zinc glycerolate intermediate. Taking into consideration together, we assert that the morphologies as well as the surface conditions of ZnO microstructures can be controlled effectively by varying the ammonia concentration of the reaction mixture under microwave irradiation.

An effective way to study the defect structures of metal oxide semiconductors is the measurement of optical properties. The characterization of the surface conditions of ZnO microstructures is important because surface defects are closely associated with the photocatalytic performances of ZnO particles. Figure 5-5a reveals that UV-visible extinction spectra of as-prepared

ZnO microstructures, which show the typical intrinsic UV absorption features of ZnO, are almost invariant. The estimated bandgaps of 3.41 eV from the extinction spectra are slightly higher than with the bulk ZnO band gap of 3.37 eV.[14-15] These results indicate that the electronic structures of our ZnO microstructures are similar as the electronic structure of bulk ZnO due to the absence of the confinement effect in micrometer sizes. Photoluminescence spectra of Figure 5-5b show two distinct emission bands; whereas the narrow UV emission band around 390 nm arises from band-edge transition, the broad orange emission band around 520 nm originates from the radiative recombination of charge carriers in surface defects. Figure 5-5b shows that orange emission from surface defects, as well as UV emission, increases with the ammonia concentration in the reaction mixture, supporting that the specific surface areas of ZnO microstructures increases with the increment of the ammonia concentration (Table 5-1).

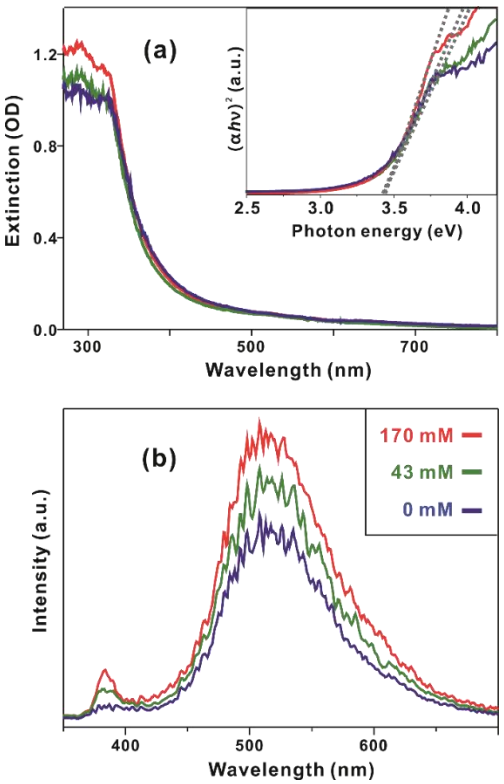

Figure 5-5. (a) UV-visible extinction spectra and (b) photoluminescence spectra with excitation at 266 nm of ZnO microstructures prepared at indicated ammonia concentrations. The inset shows the plots of $(\alpha h\nu)^2$ *vs* $h\nu$, where α is the absorption coefficient and $h\nu$ is the photon energy.

To obtain valuable information about the growth kinetics of ZnO microstructures, we have measured that the hydrodynamic sizes of particles grown in the reaction medium as a function of the microwave irradiation time (Figure 5-6). After microwave irradiation for 1.0 min, the clear initial reaction mixture inside the reactor has started to become a turbid and white suspension. Assuming that the initial hydrodynamic sizes resemble with the nucleus sizes closely, we have estimated the nucleus sizes indirectly from the initial reaction

mixture although it is technically impossible to observe their real sizes due to their transient existence. The hydrodynamic sizes of particles grown for 1.0 min under microwave irradiation decrease as the ammonia concentration increases. Considering the fact that the burst of nucleation makes nuclei of small sizes generally, we suggest that the nucleation rate increases with the increment of ammonia in the reaction mixture. As the microwave irradiation time increases, however, the hydrodynamic sizes at a high ammonia concentration increase fast to overtake the hydrodynamic sizes at a low ammonia concentration. The addition of ammonia provides a basic environment, where the nucleation, growth, and hydrolysis of intermediate zinc glycerolate particles can be boosted up by base-catalysis processes. In addition, ammonia can stock free Zn^{2+} ions temporarily by forming $[Zn(NH_3)_4]^{2+}$ complexes, whose Zn^{2+} ions can then be released to growing ZnO particles when the concentration of free Zn^{2+} ions becomes low in the reaction medium, as follows:

$$Zn^{2+} + 4NH_3 \rightleftarrows Zn(NH_3)_4^{+} \quad (1)$$

$$Zn(NH_3)_4^{+} + 2OH^- \rightleftarrows ZnO + 4NH_3 + H_2O \quad (2)$$

This efficient supply of zinc ions can increase the growth rate of ZnO microstructures. The estimated growth rate constants (k) from the single-exponential growth functions of Figure 5-6 agree well with our suggestion that the growth rates of ZnO microstructures are surely enhanced with the increase of ammonia in the reaction medium.

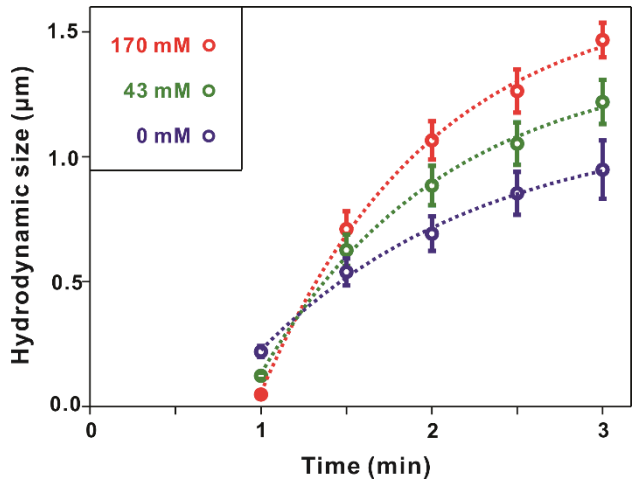

Figure 5-6 Hydrodynamic size evolution of ZnO microstructures prepared at indicated ammonia concentrations, measured by DLS in water. Each datum point represents the standard deviation of three measurements. The obtained data have been fitted to single-exponential growth functions ($y=a\cdot e^{-k\,t}+b$), resulting in rate constants (k) of 1.26×10^{-2} s^{-1} (0 mM), 1.54×10^{-2} s^{-1} (43 mM), and 1.67×10^{-2} s^{-1} (170 mM).

To shed light on the formation mechanism of our ZnO microstructures, we have investigated the time-dependent morphological and structural variation of ZnO microstructures grown at a particular ammonia concentration of 170 mM (Figure 5-7). The SEM images of Figure 5-7a show that the morphologies at the early growth stage of 1.5 min are irregular submicrosized structures, which are found to consist of zinc glycerolate (Figure 5-7b). Twin microstructures having the mixed phases of zinc glycerolate and hexagonal wurtzite ZnO have been found to appear at the irradiation time of 3.0 min. Particles grow continuously to have an average diameter of 2.0 μm at the irradiation time of 6.0 min. Finally, porous burger-like ZnO twin microstructures having the pure

hexagonal wurtzite ZnO phase have been obtained at the irradiation time of 10 min.

The FTIR spectra can support the time-dependent structural conversion of intermediate zinc glycerolate into ZnO. The characteristic vibrational modes of C-O (at 1063, 1124, and 1943 cm^{-1}) and O-H (at 1468 and 1665 cm^{-1}) confirm the formation of intermediate zinc glycerolate at the microwave irradiation time of 3 min. As the microwave irradiation time increases, the vibrational modes of organic moieties disappear while the vibrational mode of Zn-O appears rapidly. The presence of the Zn-O-Zn stretching mode at 510-634 cm^{-1} indicates that Zn-O bonds prevail for microstructures grown for 10 min. The peak in the broad region of 3200-3500 cm^{-1} could be assigned to the residual O-H functional group of ZnO surfaces. Owing to this hydrophilic surfaces, our prepared ZnO microstructures can have good affinity with various guest molecules *via* hydrogen bonds.[15]

To understand the time-dependent formation mechanism of ZnO microstructures in detail, we have also measured O 1s XPS spectra, which have been deconvoluted into four distinct Gaussian curves (Table 5-1). The deconvoluted O 1s XPS spectra show that the binding environments of oxygen atoms have been changed dramatically with the increase of the reaction time; whereas the oxygen environment of microstructures grown for 3 min arises dominantly from Zn-O-C and C-O-H bonds due to internal glycerol moieties, the oxygen surroundings of microstructures grown for 10 min result mainly from Zn-O-Zn bonds, oxygen vacancies, and Zn-O-H bonds due to due to the

prevalence of ZnO crystallites, point defects, terminal O-H functional groups, respectively, throughout the surfaces of ZnO microstructures. The low intensity percentage of the Zn-O-Zn peak, in consideration of the intensity percentages of Zn-O_x-Zn and Zn-O-H peaks, for ZnO microstructures grown for 10 min has been attributed to the instrumental detection depth limit (<10 nm) of XPS, which shows surface conditions significantly. Furthermore, the high intensity percentage of the Zn-O_x-Zn peak due to oxygen vacancies matches well with the intense orange emission of burger-like ZnO twin microstructures in Figure 5-5. Overall, our XPS analysis combined with the other presented results have shown that the structural evolution of ZnO microstructures under microwave irradiation has been controlled effectively by adjusting the ammonia concentration.

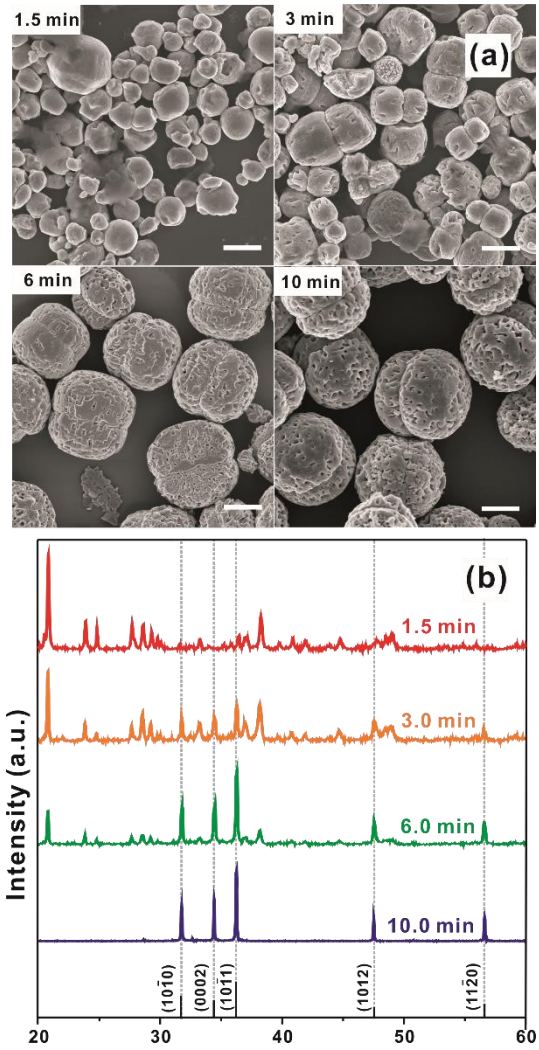

Figure 5-7 (a) SEM images of burger-like ZnO microstructures synthesized for indicated reaction times. Each scale bar indicates 1 μm. (b) HRXRD patterns of ZnO microstructures prepared at 170 mM of ammonia for indicated reaction times. The standard diffraction pattern of the hexagonal wurtzite ZnO is also shown in the bottom.

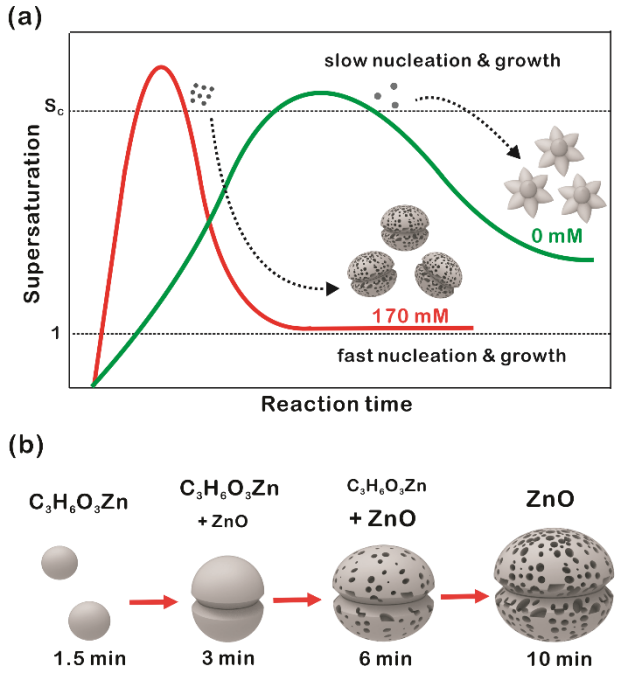

Figure 5-8 Plausible mechanisms for the ammonia-assisted growth of ZnO microstructures under microwave irradiation at two different ammonia concentrations (a) and a time-dependent growth mechanism at a particular ammonia concentration of 170 mM.

Summarizing all the presented results, we can propose the possible formation mechanisms of ZnO microstructures produced at different ammonia concentrations in terms of the LaMer theory (Figure 5-8a);[27,35] when the concentration of monomers is above the critical supersaturation (S_c), nuclei can form because monomers can overcome the energy barrier for nucleation. When the nuclei grow by incorporating additional monomers inside the reaction medium, the concentration of monomers in the solution drops quickly to a level below S_c. As long as the concentration of monomers is held below the threshold of S_c, additional nucleation events except for the growth of nuclei cannot occur.

Therefore, any factors that change the monomer concentration cause the variation of nucleation and growth kinetics considerably to induce the subsequent variation of morphologies and size distribution.[15]

As mentioned with the time-dependent DLS analysis of Figure 5-6, the growth kinetics of our ZnO microstructures depends significantly on the ammonia concentration. The supply of monomers are retarded at a low concentration of ammonia, so that monomers are produced heterogeneously and depleted slowly during all the reaction stages. As a result, the nucleation of monomers and the growth of nuclei proceed slowly over an extended period of time, generating flower-like structures due to their anisotropic growth. At a high ammonia concentration, however, the supply rate of monomers can be accelerated, so that the concentration of the monomers reaches rapidly to the critical supersaturation within a very short time, resulting in a burst of nucleation. Consequently, the nuclei can form and grow rapidly, generating burger-like ZnO twin microstructures due to their homogeneous growth. Furthermore, at a high ammonia concentration, the polar surfaces of ±(0001) have been preferentially exposed (Figure 5-2). In general, the positively Zn^{2+}-terminated (0001) and the negatively O^{2-}-terminated $(000\bar{1})$ polar surfaces have high surface energies. The appearance of novel (peanut-like and burger-like) twin structures at the presence of ammonia, therefore, can be explained by electrostatic inter-particle attractions at the polar surfaces to minimize the high surface energy of polar surfaces at the early growth stages (Figure 5-8b). As explained already, the rich pores of burger-like ZnO microstructures fabricated

at a high ammonia concentration of 170 mM originate from microcracks and wrinkles produced during the fast hydrolysis process of intermediate zinc glycerolate microstructures. In summary, the variation of the ammonia concentration in the reaction mixture can control nucleation and growth kinetics to tune the shapes and the surface conditions of ZnO microstructures.

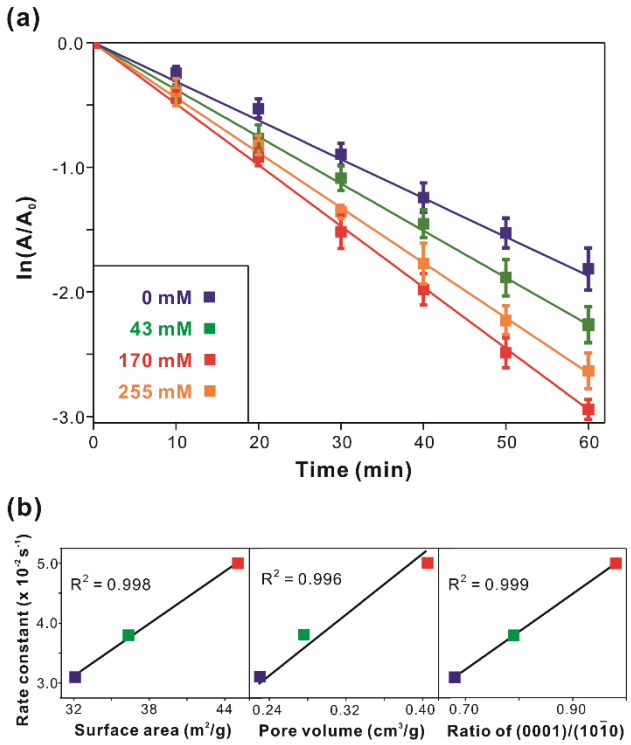

Figure 5-9 (a) First-order kinetics, $\ln(A/A_0)$ vs. irradiation time, for the photocatalytic degradation of 10 μM rhodamine B (aq) *via* different ZnO microstructures prepared at indicated ammonia concentrations under irradiation of a 300 W Xe lamp. The calculated rate constants were 0.031 s^{-1} (0 mM), 0.038 s^{-1} (43 mM), 0.050 s^{-1} (170 mM), 0.045 s^{-1}(255 mM). (b) The variation of rate constants as functions of surface area, pore volume, and (0001)/ (10$\bar{1}$0) ratio.

With increasing interests for the sustainability of environments, the eco-friendly treatment of waste water containing organic dyes has become popular increasingly.[33-37] In general, photogenerated holes in the valence band of ZnO have sufficient oxidation potential to initiate the decomposition of organic dyes; the photogenerated holes from ZnO microstructures can react with OH^- ions to form ·OH radicals for the further photocatalytic degradation of an organic dye.[32] Thus, to verify the potential environmental applications of our prepared ZnO microstructures, we have evaluated the photocatalytic properties of our prepared ZnO microstructures by monitoring the time-dependent absorbance changes of rhodamine B solutions in the presence of light irradiation (Fig. S7†). The photocatalytic degradation rate constants of ZnO microstructures have been obtained by plotting $\ln(A/A_0)$ vs. light irradiation time in Fig. 9a, revealing that burger-like ZnO twin microstructures prepared at an ammonia concentration of 170 mM have highest photocatalytic performances. As confirmed by defect emission in Fig. 5, the rich surface pores of burger-like ZnO microstructures have functioned as quantum wells where photoexcited electrons are confined to delay electron–hole recombination. Thus, during the photocatalytic process, long-lived charge carriers have been generated efficiently on the surfaces, enhancing the photocatalytic activity of burger-like ZnO microstructures. As shown in Fig. 9b, the photocatalytic degradation rate constant of rhodamine B increases linearly with the specific surface area, the specific pore volume, and the polar-surface exposure of ZnO microstructures. This indicates indeed that the photocatalytic activity of ZnO microstructures

can be improved well by controlling surface conditions. Thus, we suggest that our microwave-assisted synthesis can tune the photocatalytic performances, as well as the structures and morphologies, of ZnO microstructures.

5. 5. Conclusion

The morphologies of ZnO microstructures ranging from 1 μm to 2 μm have been controlled rapidly *via* a microwave-assisted one-pot synthetic route with variation of the ammonia concentration in the reaction medium; whereas flower-like ZnO microstructures have been obtained in the absence of ammonia, various ZnO twin microstructures have been prepared in the presence of ammonia. Ammonia has kinetically controlled the ZnO growth along the [10$\bar{1}$ 0] direction, exposing ±(0001) polar planes preferencially. Owing to interparticular electrostatic interactions at the exposed polar planes, novel twin microstructures of ZnO have been generated at the presence of ammonia. Prepared ZnO microstructures have been found to be mesoporous with large specific surface areas (32.1 m^2/g - 45.0 m^2/g) and high specific pore volumes (0.235 m^3/g - 410 m^3/g), which have resulted from the microwave-assisted fast hydrolysis of intermediate zinc glycerolate microstructures. ZnO microstructures show characteristic defect-driven orange emission, whose intensity increases with the specific surface area. Time-dependent morphological and structural variation has revealed the detailed formation mechanism of ZnO microstructures; the variation of the ammonia concentration in the reaction mixture can control nucleation and growth kinetics to vary the

shapes and the surface conditions of ZnO microstructures. The photocatalytic degradation rate constant of rhodamine B *via* ZnO microstructures increases linearly with the specific surface area, the specific pore volume, and the polar-surface exposure. Our simple, rapid microwave-assisted synthetic method is considered to be beneficial to the preparation of morphology-controlled metal oxides that are applicable for eco-friendly waste-water treatment.

5. 7. References

(1) Y. Liu, J. Goebl, Y. Yin, *Chem. Soc. Rev.*, 2013, **42**, 2610−2653.

(2) C. Zhu, D. Du, A. Eychmüller and Y. Lin, *Chem. Rev*. 2015, **115**, 8896−8943

(3) M. Baghbanzadeh, L. Carbone, P. D. Cozzoli, C. O. Kappe, *Angew. Chem. Int. Ed.* 2011, **50**, 11312−11359.

(4) Y.-W. Jun, J.-S. Choi, J. Cheon, *Angew. Chem. Int. Ed.* 2006, **45**, 3414−3439.

(5) Y. Kim, H.-B. Kim, D.-J. Jang, *J. Mater. Chem. A* 2014, **2**, 5791−5799.

(6) D. Koziej, A. Lauria, M. Niederberger, *Adv. Mater*., 2014, **26**, 235–257.

(7) H. Wang, A. L. Rogach, *Chem. Mater.*, 2014, **26**, 123–133.

(8) X. Sun, Q. Li, J. Jiang and Y. Mao, *Nanoscale*, 2014, **6**, 8769−8780.

(9) H.-B. Kim, H. Kim, W. I. Lee, D.-J. Jang, *J. Mater. Chem. A*, 2015, **3**,9714−9721.

(10) J.-Y. Kim, D. Lee, H. J. Kim, I. Lim, W. I. Lee, D.-J. Jang, *J. Mater. Chem. A*, 2013, **1**, 5982−5988.

(11) E.-S. Jang, X. Chen, J.-H. Won, J.-H. Chung, D.-J. Jang, Y.-W. Kim and J.-H. Choy, *Appl. Phys. Lett.*, 2010, **97**, 043109.

(12) D. I. Son, B. W. Kwon, D. H. Park, W.-S. Seo, Y. Yi, B. Angadi,C.-L. Lee and W. K. Choi, *Nat. Nanotech*., 2012, **7**, 465-471.

(13) S. Bai, W. Wu, Y. Qin, N. Cui, D. J. Bayerl and X. Wang, *Adv. Funct. Mater*., 2011, **21**, 4464–4469.

(14) R. Agrawal and H. D. Espinosa, *Nano Lett*. 2011, **11**, 786–790.

(15) S. Cho, S.-H. Jung and K.-H. Lee, *J. Phys. Chem. C*, 2008, **112**, 12769–12776.

(16) X.-G. Han, H.-Z. He, Q. Kuang, X. Zhou, X.-H. Zhang, T. Xu, Z.-X. Xie and L.-S. Zheng, *J. Phys. Chem. C*, 2009, **113**, 584-589.

(17) M. R. Alenezi, A. S. Alshammari, K. D. G. I. Jayawardena, M. J. Beliatis, S. J. Henley and S. R. P. Silva, *J. Phys. Chem. C*, 2013, **117**, 17850–17858.

(18) F. Li, F. Gong, Y. Xiao, A. Zhang, J. Zhao, S. Fang and D. Jia, *ACS Nano*, 2013, **7**, 10482–10491.

(19) J. Baier, N. J. Blumenstein, J. Preusker, L. P. H. Jeurgens, U. Welzel, T. A. Do, J. Pleiss and J. Bill, *CrystEngComm*, 2014, **16**, 5301–5307.

(20) J. Das and D. Khushalani, *J. Phys. Chem. C*, 2010, **114**, 2544–2550.

(21) Y. Hong, C. Tian, B. Jiang, A. Wu, Q. Zhang, G. Tian and H. Fu, *J. Mater. Chem. A*, 2013, **1**, 5700–5708.

(22) J. Zhao, X. Zou, L.-J. Zhou, L.-L. Feng, P.-P. Jin, Y.-P. Liu and G.-D. Li, *Dalton Trans.*, 2013, **42**, 14357–14360.

(23) A. Sinhamahapatra, D. Bhattacharjya and J.-S. Yu, *RSC Adv.*, 2015, **5**, 37721–37728.

(24) S. Zhang, P. Yang, A. Zhang, R. Shi and Y. Zhu, *CrystEngComm*, 2013, **15**, 9090–9096.

(25) H. Dong and C. Feldmann, *J. Alloys Compd.*, 2012, **513,** 125–129.

(26) M. N. Nadagouda, T. F. Speth and Varma, R. S., *Acc. Chem. Res.*, 2011, **44**, 469–478.

(27) I. Bilecka and M. Niederberger, *Nanoscale*, 2010, **2**, 1358–1374.

(28) Cintas, P.; Tagliapietra, S.; Gaudino, E. C.; Palmisano, G.; Cravotto, G. *Green Chem.* 2014, **16**, 1056-1065.

(29) H.-B. Kim, D.-J. Jang, *CrystEngComm*, 2015, **17**, 3325–3332.

(30) Y. Tang, P. Wee, Y. Lai, X. Wang, D. Gong, P. D. Kanhere, T.-T. Lim, Z. Dong, Z. Chen, *J. Phys. Chem. C*, 2012, **116**, 2772–2780.

(31) N. Qin, Q. Xiang, H. Zhao, J. Zhanga and J. Xu, *CrystEngComm*, 2014, **16**, 7062–7073.

(32) D. Pugliese, F. Bella, V. Cauda, A. Lamberti, A. Sacco, E. Tresso and S. Bianco, *ACS Appl. Mater. Interfaces*, 2013, **5**, 11288−11295.

(33) X. Yang, H. Fu, A. Yu, X. Jiang, *J. Colloid Interf. Sci.*, 2012, **387**, 74−83.

(34) Zhong, L.-S.; Hu, J.-S.; Wan, L.-J.; Song, W.-G. *Chem. Commun.*, 2008, 1184-1186.

(35) C. Park, J. Lee and W. S. Chang, *J. Phys. Chem. C*, 2015, **119**, 16984−16990.

(36) D. Chen, Z. Wang, T. Ren, H. Ding, W. Yao, R. Zong and Yongfa Zhu, *J. Phys. Chem. C*, 2014, **118**, 15300−15307

(37) J. Park, J. Joo, S. G. Kwon, Y. T. Hyeon, *Angew. Chem. Int. Ed.*, 2007, **46**, 4630−4660.

(38) K. L. Sowers, B. Swartz, T. D. Krauss, *Chem. Mater.* 2013, **25**, 1351−1362.

(39) S. Y. Park, S. Kim, J. Yoo, K.-H. Lim, E. Lee, K. Kim, J. Kim and Y. S. Kim, *RSC Adv.*, 2014, **4**, 11295–11299.

(40) A. R. Tao, S. Habas, P. Yang, *Small*, 2008, **4**, 310–325.

(41) E.-S. Jang, J.-H. Won, Y.-W. Kim, Z. Cheng and J.-H. Choy, *CrystEngComm*, 2011, **13**, 546–552.

Appendices

A. 1. List of Publications

(1) **Hyung-Bae Kim** and Du-Jeon Jang "Precursor-dependent shape variation of wurtzite CdSe crystals in a microwave-assisted polyol process" *CrystEngComm* **2012**, *14*, 6946-6951.

(2) Sun-Young Park, **Hyung-Bae Kim**, Byung Kook Yoo, and Du-Jeon Jang "Direct observation of conformation-dependent pathways in the excited-state proton transfer of 7-hydroxyquinoline in bulk alcohols" *J. Phys. Chem. B* **2012**, *116*, 14153–14158.

(3) Jong-Yeob Kim, **Hyung-Bae Kim,** and Du-Jeon Jang "Electrophoretic separation of gold nanoparticles according to bifunctional molecules-induced charge and size" *Electrophoresis*, **2013**, *34*, 911–916.

(4) Daeki Lee, **Hyung-Bae Kim,** and Du-Jeon Jang "Enhanced photocatalytic performances of cocrystalline TiO_2 nanoblossoms by the effect of nanoscale p-n junctions" *J. Nanopart. Res.*, **2014**, *16*, 2187(1)-2187(11).

(5) Daeki Lee, **Hyung-Bae Kim,** Sora Yu, Hark-Jin Kim, Wan In Lee, and Du-Jeon Jang "“Facile fabrication of anatase TiO_2 nanotube arrays having high photocatalytic and photovoltaic performances by anodization of titanium in mixed viscous solvents” *J. Mater. Sci.*, **2014**, *49*, 3414-3422.

(6) Younshin Kim, **Hyung-Bae Kim,** and Du-Jeon Jang "Facile microwave fabrication of CdS nanobubbles with highly efficient photocatalytic performances" *J. Mater. Chem. A*, **2014**, *2*, 5791-5799.

(7) **Hyung-Bae Kim** and Du-Jeon Jang "Morphological variation of anatase TiO_2 crystals *via* formation of titanium glycerolate precursors under microwave Irradiation" *CrystEngComm*, **2015**, *17*, 3325-3332.

(8) **Hyung-Bae Kim,** Harkjin Kim, Wan In Lee, and Du-Jeon Jang "Hierarchical mesoporous anatase TiO_2 nanostructures with efficient photocatalytic and photovoltaic performances" *J. Mater. Chem. A*, **2015**, *3*, 9714 - 9721.

(9) **Hyung-Bae Kim** and Du-Jeon Jang "Dislocation-Driven Growth of Porous CdSe Nanorods from CdSe·(ethylenediamine)$_{0.5}$ Nanorods " *Nanoscale*, **2016**, *8*, 403 - 410.

(10) **Hyung-Bae Kim,** Dong-Won Jeong, and Du-Jeon Jang "Morphology-Tunable Synthesis of ZnO Microstructures under Microwave Irradiation: Formation Mechanisms and Their Photocatalytic Activity " *CrystEngComm*, **2016**, (DOI: 10.1039/C5CE02334C) in press.

A. 2. List of International Presentations

(1) **Hyung-Bae Kim** and Du-Jeon Jang “Enhanced Photocatalytic Effect of Platinum-Decorated Inorganic-Organic Hybrid Nanorods” **Gordon Research Conference on Colloidal Macromolecular & Polyelectrolyte Solutions, Ventura, California, USA (2012).**

(2) **Hyung-Bae Kim** and Du-Jeon Jang “Structure, Optical Property, and Photocatalytic Effect of CdSe Nanorods and CdSe·(en)$_{0.5}$ Nanocomposites with and without Platinum” **The First International Conference on Photocatalysis and Solar Energy Conversion: Development of Materials**

and Nanomaterials, Daejeon, Korea (2012).

(3) Younshin Kim, **Hyung-Bae Kim,** Jin-Ah Kwak and Du-Jeon Jang "Microwave-Assisted Preparation of CdS Hollow Nanospheres with Enhanced Photocatalytic Activity" **The First International Conference on Photocatalysis and Solar Energy Conversion: Development of Materials and Nanomaterials, Daejeon, Korea (2012).**

(4) **Hyung-Bae Kim,** Daeki Lee and Du-Jeon Jang "Facile Fabrication of Anatase TiO_2 Nanotube Arrays by Anodization of Titanium in Mixed Viscous Solvents" **MRS Spring Meeting & Exhibit, San Francisco, California, USA, USA (2014).**

Abstract (Korean)

형태가 조절된 반도체 나노물질을 정밀하게 제조하는 방법을 개발하고 개발된 물질의 특성 평가 및 실용성에 대하여 물리화학 및 재료화학 관점에서 연구하였다. 이번 연구를 통하여 형태를 제어하는 4가지 방법 (공전구체 방법, 결합 유발 방법, 공용매 방법, 그리고 첨가물 방법) 을 개발하였는데 성공하였으며 이를 위하여 효과적인 합성 방법을 위하여 마이크로파나 오토클레이브를 선택적으로 이용하였다. 형태가 제어된 나노물질의 형성 메커니즘을 파악하기 위하여 주로 LaMer 이론을 도입하여 설명하였으며 형태가 제어된 물질의 물리적 화학적 특성평가를 체계적으로 파악하고 광촉매, 태양전지 분야에 다양하게 응용하여 이 분에 영향을 주는 나노물질이 갖는 형태학적 요소에 대하여 분석하였다. 제 1 장 도입부에서는 주로 나노 물질의 기본적인 특성에 대하여 양자제한 효과를 인용하여 설명하였고 특히 형태가 제어된 물질이 갖는 방향의존성 양자제한 효과를 설명하여 이번 연구의 필요성을 강조하였다. 형태가 제어된 물질의 특성을 결정하는 다양한 변수 (크기, 모양, 표면조건)에 대해서도 소개하고 이것을 조절하기 위한 다양한 형성 속도 인자들에 대해서 설명하였다.

제 2 장에서는 CdSe 합성하는데 쓰이는 두 전구체 (CdO 와 CdCl2)의 상대적인 비율을 조절하여 서로 다른 모양의 CdSe 나노 물질을 합성하는데 성공하였다. 이는 각각의 전구체가 반응 용액과의 상호작용 유무에 따른 결정화와 성장의 속도가 상이하므로 전구체의 비율을 조절하면 다양한 속도로 결정화 및 성장하는 나노물질을 만들 수 있게 되고, 결과적으로 여러 가지 모양의 나노물질이 만들어 짐을 발견하였다. 합성된 물질이 모양에 따른 분광학적 성질을 띄게 됨을

발견함으로써, 이번 합성 방법으로 나노구조의 모양과 분광 성질을 모두 조절할 수 있음을 파악하였다.

제 3 장에서는 피리 모양의 다공성 CdSe 화합물 반도체 나노막대를 다양한 결정결함(점, 선, 면 결함)의 도움을 통하여 합성하고 그것의 합성 메커니즘과 적외선 발광의 분광학적 특성을 체계적으로 규명하였다. 일반적으로 반도체 결함은 부정적인 영향을 끼친다고 알려져 있는데 이번 실험은 오히려 그 결함을 장점으로 이용하여 나노구조의 성질을 제어하는데 의의가 있다.

제 4 장에서는 마이크로파를 이용하여 기존의 합성 시간보다 1/10~1/100 정도 단축시켜 비표면적이 큰 계층적 구조의 이산화 티타늄을 합성하고 그것의 모양을 조절하는데 하는 인자를 찾아내어 합성 메커니즘을 보고 하였다. 개발된 합성법은 산화물 반도체를 만드는 다양한 분야에 경제적 시간적 기여를 할 수 있을 것으로 기대되며 이러한 합성법을 적용시켜 모양에 따른 이산화 티타늄 산화물 반도체의 휘발성 유기물 분해 및 이산화탄소 고정 반응에 대한 광촉매 효율 그리고 염료감응 태양전지의 효율을 측정하고 그 실용화 가능성에 대해서 확인하였다.

제 5 장에서는 마이크로파를 이용하여 쌍둥이 모양의 다공성 산화아연을 단일 단계 처리로 손쉽게 합성하는 조절 인자인 암모니아의 농도를 파악하고 그것의 형성 메커니즘과 분광학적 특성 그리고 광촉매적 효율을 체계적으로 분석하였다. 합성된 물질 중 쌍둥이 모양의 갖는 햄버거 형태의 산화아연은 높은 비표면적과 메조 구멍의 시너지로 높은 광촉매 효율을 갖는다는 것을 발견하였다.

주요어: 반도체 나노입자, 나노과학, 분광학, 광촉매, 태양전지

학번: 2010 - 20273